Technische Universität München
TUM School of Natural Sciences

Controlling Light–Matter Interaction via Collective Effects in Atom Arrays

David Castells Graells

Vollständiger Abdruck der von der TUM School of Natural Sciences der Technischen Universität München zur Erlangung eines

Doktors der Naturwissenschaften (Dr. rer. nat.)

genehmigten Dissertation.

Vorsitz:	Prof. Dr. Stefan Filipp
Prüfende der Dissertation:	1. Hon-Prof. Ignacio Cirac, Ph.D. 2. Prof. Dr. Peter Rabl

Die Dissertation wurde am 30.10.2024 bei der Technischen Universität München eingereicht und durch die TUM School of Natural Sciences am 12.11.2024 angenommen.

Abstract

The ability to control individual atoms and photons is crucial to building artificial quantum systems for novel technological applications. It is, however, not possible to achieve deterministic light–-matter interactions at the single-photon level in free space due to the small optical cross-section of atoms and the diffraction limit of light. A leading approach to overcome this limitation consists of confining light within optical resonators, thereby increasing the probability of interaction. This is the basis of the fields of cavity and waveguide quantum electrodynamics (QED), which have achieved high-fidelity light–-matter interaction and have enabled the exploration of complex systems with rich phenomenology. Despite such impressive demonstrations, the need to place individual atoms close to dielectric surfaces while maintaining a high degree of coherence presents a major technical obstacle to scaling up current cavity and waveguide QED platforms.

This thesis addresses this challenge by proposing alternative platforms consisting only of individually trapped atoms without conventional mirrors or waveguides. This is possible by harnessing collective optical resonances that arise when the atoms are separated by distances smaller than the wavelength of the resonant light. To control the resonances, we arrange the atoms in regular lattices, which enhances collective effects through interference and gives rise to prominent features such as extremely long-lived subradiant states and nearly perfect reflection. We show that it is possible to engineer arrays of atoms to achieve tunable and strong interactions between their collective states and additional atoms placed nearby. We observe the typical features of the conventional waveguide QED scenario in a system where the role of the waveguide is played by a one-dimensional atom array, and the role of the emitters is played by pairs of closely separated atoms that form an effective two-level system. We solve the dynamics of the system both when the emitter frequency lies inside and when it lies outside the band of modes of the array. Along with well-known phenomena of collective emission into the guided modes and waveguide-mediated long-range atom-–atom interactions, we uncover significant non-Markovian corrections, which arise from the finite size of the array and retardation effects. In addition to employing one-dimensional atom arrays as waveguides, we show that a pair of two-dimensional arrays can act as a cavity described by conventional cavity QED

parameters. Such an atom-array cavity exhibits the same cooperativity as a conventional counterpart with matching mirror specifications even though the cavity coupling strength and decay rate are modified by the narrow bandwidth of the atoms. We show that very high cooperativities can be achieved with an ideal setup. We also study the impact of atomic motion and disorder on our predictions, as it can be much detrimental to the collective response. Our estimations based on realistic parameters show that the main features survive and that useful fidelities can be achieved.

Our work presents a promising platform for high-fidelity QED applications based on all-atomic setups, eliminating the need for additional optical elements. This creates opportunities for exploring novel phenomena owing to the unique features of atom arrays, including their quantum nonlinearity and the ability to dynamically control them. Future work may build on the large toolbox available with atom arrays to develop exciting applications unattainable with conventional setups.

Zusammenfassung

Die Fähigkeit, einzelne Atome und Photonen zu kontrollieren, ist entscheidend für den Aufbau künstlicher Quantensysteme zur Entwicklung neuartiger technologischer Anwendungen. Es ist jedoch im freien Raum nicht möglich, deterministische Licht-Materie-Wechselwirkungen auf der Ebene einzelner Photonen zu erreichen, da Atome nur einen kleinen optischen Wirkungsquerschnitt besitzen und das Licht dem Beugungslimit unterliegt. Ein führender Ansatz zur Überwindung dieser Einschränkung besteht darin, Licht in optischen Resonatoren zu halten, wodurch die Wahrscheinlichkeit einer Wechselwirkung erhöht wird. Dies bildet die Grundlage der Felder der Hohlraum- und Wellenleiter-Quanten-Elektrodynamik (QED), die hochgradige Licht-Materie-Wechselwirkungen erreicht und die Erforschung komplexer Systeme mit reicher Phänomenologie ermöglicht haben. Trotz dieser beeindruckenden Fortschritte stellt die Notwendigkeit, einzelne Atome nahe an dielektrische Oberflächen zu platzieren und dabei einen hohen Kohärenzgrad aufrechtzuerhalten, ein erhebliches technisches Hindernis für die Skalierung derzeitiger Hohlraum- und Wellenleiter-QED-Plattformen dar.

Diese Dissertation adressiert diese Herausforderung, indem sie alternative Plattformen vorschlägt, die ausschließlich aus einzeln gefangenen Atomen bestehen und keine herkömmlichen Spiegel oder Wellenleiter erfordern. Dies ist möglich durch die Nutzung kollektiver optischer Resonanzen, die auftreten, wenn die Atome in Abständen kleiner als die Wellenlänge des resonanten Lichts angeordnet sind. Um die Resonanzen zu kontrollieren, ordnen wir die Atome in regelmäßigen Gittern an, wodurch kollektive Effekte durch Interferenz verstärkt werden und sich markante Eigenschaften wie extrem langlebige subradiante Zustände und nahezu perfekte Reflexion ergeben. Wir zeigen, dass es möglich ist, Atomgitter so zu gestalten, dass einstellbare und starke Wechselwirkungen zwischen ihren kollektiven Zuständen und zusätzlichen nahegelegenen Atomen erreicht werden. Wir beobachten die typischen Merkmale des konventionellen Wellenleiter-QED-Szenarios in einem System, in dem die Rolle des Wellenleiters von einem eindimensionalen Atomgitter übernommen wird und die Rolle der Emitter von Paaren dicht benachbarter Atome gespielt wird, die ein effektives Zwei-Niveau-System bilden. Wir lösen die Dynamik des Systems sowohl, wenn die Emissionsfrequenz innerhalb des Modenbandes des Gitters liegt, als auch,

wenn sie außerhalb liegt. Neben bekannten Phänomenen der kollektiven Emission in die geführten Moden und wellenleitervermittelten langreichweitigen Atom-Atom-Wechselwirkungen decken wir signifikante non-Markovian Korrekturen auf, die aus der endlichen Größe des Gitters und Verzögerungseffekten resultieren. Zusätzlich zur Verwendung eindimensionaler Atomgitter als Wellenleiter zeigen wir, dass ein Paar zweidimensionaler Atomgitter als Hohlraum fungieren kann, der durch herkömmliche Hohlraum-QED-Parameter beschrieben wird. Ein solcher Atomgitter-Hohlraum zeigt dieselbe Kooperativität wie ein konventionelles Pendant mit passenden Spiegelanforderungen, obwohl die Kopplungsstärke des Hohlraums und die Zerfallsrate durch die schmale Bandbreite der Atome modifiziert werden. Wir zeigen, dass mit einem idealen Aufbau sehr hohe Kooperativitäten erreicht werden können. Wir untersuchen auch den Einfluss atomarer Bewegung und Unordnung auf unsere Vorhersagen, da dies die kollektive Antwort stark beeinträchtigen kann. Unsere Schätzungen basierend auf realistischen Parametern zeigen, dass die Haupteigenschaften bestehen bleiben und dass nützliche Fidelitäten erreicht werden können.

Unsere Arbeit stellt eine vielversprechende Plattform für hochgradige QED-Anwendungen auf Basis rein atomarer Aufbauten dar, wodurch zusätzliche optische Elemente überflüssig werden. Dies schafft Möglichkeiten zur Erforschung neuer Phänomene, die sich aus den einzigartigen Eigenschaften von Atomgittern ergeben, einschließlich ihrer Quantennichtlinearität und der Möglichkeit, sie dynamisch zu regeln. Zukünftige Arbeiten könnten auf dem großen Werkzeugkasten, den Atomgitter bieten, aufbauen, um spannende Anwendungen zu entwickeln, die mit konventionellen Aufbauten unerreichbar sind.

List of Publications

Publications related to this Thesis

[1] **D. Castells-Graells**, D. Malz, C. C. Rusconi, and J. I. Cirac,
Atomic waveguide QED with atomic dimers
Physical Review A 104, 063707 (2021).
See chapter 3.

[2] **D. Castells-Graells**, J. I. Cirac, and D. S. Wild
Cavity Quantum Electrodynamics with Atom Arrays in Free Space
arXiv preprint arXiv:2409.15434 (2024).
See chapter 4.

Further publications not included in this thesis

[3] K. K. Nielsen, L. Wangler, **D. Castells-Graells**, D. Malz, C. C. Rusconi,
Polaron-Polaritons in Subwavelength Arrays of Trapped Atoms
In preparation

Contents

1 Introduction

At the beginning of the last century, theoretical work around a series of experiments such as the black body radiation and the photoelectric effect led to the birth of quantum mechanics and the fundamental idea of wave-particle duality. A series of scientific and technological breakthroughs followed from these new ideas, including a new understanding of the periodic table and chemical interactions, the transistor and the laser. This is often termed the *first quantum revolution*, in which quantum mechanics was used to understand what already existed to unlock new potential for applications.

While we could observe and predict the consequences of quantum mechanics, pure quantum systems remained elusive due to the difficulty of manipulating sufficiently small systems, down to a few quanta of light and matter, and keeping them isolated from the environment. However, the continuous development of experimental physics and engineering has addressed these issues, leading into a *second quantum revolution*, in which it is now possible to control individual atoms and photons. This offers a new paradigm in which artificial quantum systems with tailored properties can be built. The potential for applications is vast, most notably including quantum simulation, quantum computing, quantum cryptography, and quantum sensing, collectively known as *quantum technologies*.

Many quantum matter systems exist that offer the possibility to support specific quantum states and allow for unitary operations through controllable interactions. These systems, however, must be well isolated, since quantum superposition is highly susceptible to interactions with the environment. This collides with the requirement of being able to measure their quantum state with high efficiency. Light, on the other hand, can be easily measured, encodes quantum states in its polarization, and sustains coherence over long distances owing to its weak interaction with the environment, but photon-photon interactions are extremely weak in free space. Therefore, many technologies take advantage of storing quantum states on atomic degrees of freedom and use light to access the system at will for preparation, control, and measurement.

A key element in developing quantum technologies lies thus in coherently controlling light–matter interaction down to the single-photon level. For this, sources

of light that can absorb and emit single photons, usually known as quantum emitters, are required. In this thesis, we consider optical dipole transitions in neutral atoms, although our approaches apply to other types of dipole emitters. Using only atoms and photons is especially appealing, since they can be manipulated in a controlled environment. Moreover, their simplicity allows for a good understanding of their couplings and to achieve much better environmental isolation compared to more complex solid-state systems. The large toolbox available in neutral atom experiments [4], including the ability to cool atoms to very low temperatures, arrange them in large lattices with tailored geometries, and control and measure their quantum state with high precision makes them a very promising platform for quantum technologies [5, 6].

In particular, atom-based platforms have been considered for many applications in which interfacing matter and light plays a central role, including quantum information processing [7], studying quantum matter [8], quantum metrology [9], and realizing nonlinear optics [10]. To implement robust and scalable applications, it is essential to achieve deterministic atom–light interactions, but these are unfeasible in free space due to the small optical cross-section of an atom and the diffraction limit of light [11, 12]. Tight-focusing experiments to maximize free-space atom–light interaction have measured just about a 10% attenuation of near-resonant light [13].

Several approaches to overcome this limitation have been explored. A common strategy is to boost the light–matter interaction by increasing the number of emitters. While this raises the probability that a single photon interacts with the ensemble of emitters, it also effectively reduces the quantum nonlinearity. The nonlinearity may be reinstated by introducing strong interactions between the emitters by, for instance, exciting them to high-lying Rydberg states. However, requirements on the direct interaction between the emitters restrict the range of physical platforms for which this approach is applicable.

As an alternative strategy, the fields of cavity and waveguide quantum electrodynamics (QED) seek to enhance the light–matter interaction beyond the limits in free space by placing the emitter within an optical resonator, such as optical cavities made of highly reflective mirrors or nanophotonic structures like optical waveguides. The confinement of a single photon enhances its electric field, thereby resulting in a stronger interaction with the emitter, and increases the interaction time before the photon leaves the system. High-fidelity, deterministic light–matter interaction has been demonstrated in a variety of cavity QED setups [14] and a rich phenomenology can be explored using waveguides with non-trivial energy bands [15]. However, scaling up these systems presents a technological challenge owing

to the complexity of fabricating high-quality optical resonators and trapping individual emitters within, while maintaining the coherence of both components. For instance, the nearby presence of dielectric structures can affect trapping and readout, and imperfections on the surfaces disturb the electromagnetic field around the atoms.

In this thesis, we show that the collective optical response of ordered arrays of atoms can be used to replace optical elements such as waveguides and optical cavities. Additional atoms can interact with these collective states to realize waveguide and cavity QED schemes. These additional atoms, which we label as *target atoms* throughout this thesis, can even be of the same species as the array atoms using additional laser control. This is possible because atoms can interact with each other by absorbing and reemitting light. The interaction is strong when the distance between atoms is similar or smaller than the wavelength resonant with the atomic transition. This light-mediated effective interaction has both a coherent and a dissipative contribution, shifting the resonance energy of the collective atomic eigenstates and modifying their collective decay rate into free space, respectively. For instance, two interacting atoms will exhibit a superradiant collective eigenstate in which the atoms are in phase and their emission shows constructive interference and a subradiant eigenstate with atoms out of phase and interfering destructively.

The interference effects in collective resonances can be enhanced by arranging many atoms in a regular lattice. The many interactions between atoms make the range of collective states richer. For large lattices, the collective eigenstates become Bloch modes, forming a photonic band structure. In the subwavelength regime — when the inter-atomic spacing is smaller than the wavelength of the characteristic atomic dipole transition — some collective eigenstates can have associated quasi-momenta that are larger than the momentum of light. Far-field emission is forbidden for these states due to conservation of momentum, making them dark states. For one-dimensional subwavelength arrays, these dark states will propagate as guided modes similar to waveguides. A two-dimensional array will scatter light at specific angles like a Bragg diffractor. In a subwavelength array, higher-order diffraction modes are suppressed and only the zeroth-order mode survives, for which the array behaves as a perfect mirror.

Our work shows that, by properly engineering the system, atom arrays can be treated effectively as waveguides and cavities in the low-excitation regime for a wide range of parameters. We show that we can reproduce essential features of waveguide and cavity QED and achieve high-fidelity light–matter interactions. We also discuss the fundamental differences with their conventional counterparts and some relevant experimental considerations. In particular, we treat atomic motion

and disorder, which can be especially destructive to the interference-based effects these platforms rely on. Nevertheless, we show that useful fidelities can be achieved with current parameters.

Apart from obviating the need to trap atoms near surfaces, all-atomic setups create new opportunities beyond existing conventional schemes, enabling new protocols in quantum information processing as well as the exploration of new physical phenomena. Our work builds on the recent surge of interest in atom arrays, which has created a large toolbox to manipulate light, including methods to store light, modify its wavefront, mediate atom–-atom interactions, and realize photonic gates using Rydberg states. Future work can further incorporate these tools to develop new schemes that are unattainable with conventional setups. Another advantage of atom arrays is that they can be dynamically controlled in experiments using external fields to, for instance, turn on and off cavity transmission. Moreover, atom arrays exhibit quantum nonlinearities down to the few-photon level, in contrast to the weak nonlinearity of conventional materials. Taken together, this leads us to envision exciting applications such as the on-demand generation of complex quantum states of light or the realization of distributed quantum computing platforms composed entirely of trapped neutral atoms.

1.1 Outline of the Thesis

Let us now briefly summarize the structure of this thesis. In Chapter 2, we describe the model and methods used in the thesis. In Chapter 3 and Chapter 4, we focus on engineering one-dimensional atom arrays for waveguide QED applications and planar atom arrays to realize a cavity QED scheme, respectively. Atomic motion and disorder are studied for the case of cavities also in Chapter 4.

More specifically, in Chapter 2, we derive the light-mediated effective interactions between atoms that we use to predict the internal-state dynamics of atom arrays and the resulting scattered light field. We also solve the resulting effective Hamiltonian for ordered arrays and review some of the known results. We briefly introduce the basic concepts of waveguide and cavity QED, discuss some methods used in the thesis, and present the experimental setup that could implement our proposals.

In Chapter 3, we show that typical features of conventional waveguide QED can be observed in a system where the role of the waveguide is played by a one-dimensional subwavelength atomic array. We explain how a target atom can be coupled to the guided modes of the array while avoiding highly dissipative modes, and how to achieve a Markovian interaction between the atoms and the array. We then solve and discuss the dynamics of the system both when the target atom is resonant with

the band of guided modes of the array and when it lies in the band gap, comparing the results with the expectation from conventional systems. Together with well-known phenomena of collective emission into the guided modes and waveguide-mediated long-range atom–atom interactions, we observe significant non-Markovian corrections arising from the discrete array eigenstates and retardation effects.

In Chapter 4, we show that a cavity QED scheme can be realized by combining two planar arrays with a target atom placed between them. We show that the system can be described by conventional cavity QED parameters. Such an atom-array cavity exhibits the same cooperativity as a conventional counterpart with matching mirror specifications, even though the cavity coupling strength and decay rate are modified by the narrow bandwidth of the atoms. We estimate that an array cavity composed of atoms in an optical lattice can reach a cooperativity of about 10. This value can be increased by suppressing atomic motion with larger trap depths and may exceed 10^4 with an ideal placement of the atoms. We also propose a spatially dependent AC Stark shift as an alternative to curving the arrays, which reduces the experimental complexity of the scheme and may be of independent interest.

2 PRELIMINARIES

In this chapter, we present an overview of the model and methods employed throughout the thesis. We start by describing the interaction between atoms and light, and then derive the master equation and its associated effective spin Hamiltonian to describe the light-mediated interactions between atoms after eliminating the photonic environment. We then discuss the special case of ordered atom arrays with a subwavelength lattice spacing and characterize their spectrum and main features, including reflection of light by a planar array. We also discuss the modification of the atomic properties under the presence of optical elements and introduce waveguide and cavity QED. Since in this thesis we aim to use ordered atom ensembles as a bath for additional target atoms, we often are interested in the effective atom dynamics after eliminating a subset of the system. Here, we introduce these methods and discuss their validity. Finally, we describe some basic elements of an experimental implementation and the concept of using a Raman transition to control the linewidth of an atom.

2.1 ATOM–LIGHT INTERACTION

In this section, we introduce the formalism to describe the interaction of light with atoms. We start solving for the classical case of oscillating dipoles, as it is easier to derive, captures many radiative features and will give us the solutions for the propagation of the fields. Then, we present the quantized electromagnetic field and its interaction with the dipole transitions of an atom. For simplicity, we focus on two-level systems described by raising and lowering operators $\hat{\sigma}^{\pm}$, although the formalism can be readily generalized to more complex level schemes. With this, we can write the full Hamiltonian for our atom–light system. For computational purposes, however, it is often most convenient to trace out the photons. For this, w derive the quantum version of the input-output equation for the electric field, with which we obtain the field scattered by the atoms. This expression will be useful to eliminate the photonic bath and to reconstruct the electric field from the solution of the effective atom dynamics including only the atomic internal states. A constant assumption throughout this chapter is that the atoms are tightly trapped, such that we can treat

the positions of the atoms as fixed rather than as dynamical variables. We discuss the effects of motion in Chapter 4.

2.1.1 Scattering of light by a classical oscillating dipole

The free-space electromagnetic wave equation derived from Maxwell's equations reads

$$\nabla \times \nabla \times \mathbf{E}(\mathbf{r},\omega) - \frac{\omega^2}{c^2}\mathbf{E}(\mathbf{r},\omega) = \frac{1}{\epsilon_0}\frac{\omega^2}{c^2}\mathbf{P}(\mathbf{r},\omega)\,, \tag{2.1}$$

where $\mathbf{P}(\mathbf{r},\omega)$ is the polarization density of the sources. Treating the atoms as oscillating point dipoles, we can write the polarization density as $\mathbf{P}(\mathbf{r},\omega) = \sum_i \mathbf{d}_i(\omega)\delta(\mathbf{r}-\mathbf{r}_i)$, where $\mathbf{d}_i(\omega)$ is the induced dipole moment. The dipole moment is proportional to the local electric field, with the atom's polarizability, $\alpha(\omega)$, determining the strength of this response, $\mathbf{d}_i(\omega) = \alpha(\omega)\mathbf{E}(\mathbf{r}_i,\omega)$.

The electromagnetic wave equation can be solved using the Green's function

$$\nabla \times \nabla \times \mathbf{G}(\mathbf{r},\mathbf{r}_i,\omega) - \frac{\omega^2}{c^2}\mathbf{G}(\mathbf{r},\mathbf{r}_i,\omega) = \delta(\mathbf{r}-\mathbf{r}_i)\mathbf{I}\,, \tag{2.2}$$

which describes the field at position $\mathbf{r}$ generated by a source at position $\mathbf{r}_i$. In free space,

$$\mathbf{G}(\mathbf{r}_i,\mathbf{r}_j;\omega) = \frac{e^{ikr}}{4\pi r}\left[\left(1+\frac{ikr-1}{k^2r^2}\right)\mathbf{I} + \left(-1+\frac{3-3ikr}{k^2r^2}\right)\frac{\mathbf{r}_{ij}\otimes\mathbf{r}_{ij}}{r^2}\right]\,, \tag{2.3}$$

where we defined $\mathbf{r}_{ij} = (\mathbf{r}_i - \mathbf{r}_j)$, and $r = |\mathbf{r}_{ij}|$ and introduced the wavenumber $k = \omega/c$. The Green's function has the properties $\mathbf{G}^*(\mathbf{r}_i,\mathbf{r}_j;\omega) = \mathbf{G}(\mathbf{r}_i,\mathbf{r}_j;-\omega)$ and $\mathbf{G}(\mathbf{r}_i,\mathbf{r}_j;\omega) = \mathbf{G}(\mathbf{r}_j,\mathbf{r}_i;\omega)$.

The solution to Eq. (2.1) for the total electric field is, thus, the input field $\mathbf{E}_0(\mathbf{r},\omega)$ plus the field scattered by the atoms

$$\mathbf{E}(\mathbf{r},\omega) = \mathbf{E}_0(\mathbf{r},\omega) + \frac{1}{\epsilon_0}\frac{\omega^2}{c^2}\int \mathrm{d}\mathbf{r}'\,\mathbf{G}(\mathbf{r},\mathbf{r}';\omega)\cdot\mathbf{P}(\mathbf{r}',\omega)\,. \tag{2.4}$$

Since we are considering point dipoles,

$$\mathbf{E}(\mathbf{r},\omega) = \mathbf{E}_0(\mathbf{r},\omega) + \frac{1}{\epsilon_0}\frac{\omega^2}{c^2}\sum_i \mathbf{G}(\mathbf{r},\mathbf{r}_i;\omega)\cdot\mathbf{d}_i(\omega)\,. \tag{2.5}$$

As given by the Green's function, the light scattered by the atoms has a far field $(kr)^{-1}$, a mid-field $(kr)^{-2}$, and a near-field $(kr)^{-3}$ component. Note that the dipole moment involves the total field, for which the self-interaction of the dipole is captured in the second term of Eq. (2.5).

SPONTANEOUS EMISSION OF AN ATOM AND COLLECTIVE DECAY

To describe an atom classically, we use the Lorentz oscillator model [16], in which the atom is modeled as a classical harmonic oscillator, with an electron bound to the nucleus by a spring. For an atom much smaller than the optical wavelength, we approximate the electron by a point charge that sees the field at its position $\mathbf{r} = 0$. This is the dipole approximation. The equation of motion of the driven charge is

$$\frac{\mathrm{d}}{\mathrm{d}t^2}\mathbf{r} + \omega_0^2\mathbf{r} = \frac{q}{m}\mathbf{E}(\mathbf{r}, t)\,, \tag{2.6}$$

where q is the charge, m the reduced mass of the electron and ω_0 the resonance frequency. Here we neglected any source of damping. The dipole moment of the atom is $\mathbf{d} = q\mathbf{r}$. Solving the equation of motion, we obtain the atom's polarizability

$$\alpha(\omega) \simeq -\frac{q^2}{2m\omega_0}\frac{1}{\omega - \omega_0}\,. \tag{2.7}$$

Here we assumed that the transition frequency ω_0 is comparable to the probe frequency ω, such that $|\omega - \omega_0| \ll (\omega + \omega_0)/2$.

Evaluating Eq. (2.5) at the atom's position, the field radiated by a dipole including its self-interaction is

$$\mathbf{E}(\mathbf{r}, \omega) = \left[\mathbf{I} - \frac{1}{\epsilon_0}\frac{\omega^2}{c^2}\alpha(\omega)\mathbf{G}(\mathbf{r}, \mathbf{r}; \omega)\right]^{-1} \cdot \mathbf{E}_0(\mathbf{r}, \omega)\,, \tag{2.8}$$

where $\mathbf{I}$ is the 3×3 identity matrix. The isotropy of free space implies that $\mathbf{G}(\mathbf{r}, \mathbf{r}; \omega)$ is proportional to the identity. The dipole moment can thus be written as $\mathbf{d}(\omega) = \alpha(\omega)\mathbf{E}(\mathbf{r}, \omega) = \alpha_{\text{eff}}(\omega)\mathbf{E}_0(\mathbf{r}, \omega)$, where we have defined an effective polarizability to go with the input field. In the Markov approximation we use that $\omega^2\mathbf{G}(0, 0; \omega)$ varies slowly to set $\omega = \omega_0$ and write

$$\alpha_{\text{eff}}(\omega) \simeq -\frac{q^2}{2m\omega_0}\frac{1}{\omega - (\omega_0 + \Delta^{\text{cl}}) + \frac{i}{2}\gamma_0^{\text{cl}}}\,, \tag{2.9}$$

with

$$\Delta^{\text{cl}} = -\frac{q^2\omega_0}{2mc^2\epsilon_0}\text{Re}\{\mathbf{e}^* \cdot \mathbf{G}(0, 0; \omega_0) \cdot \mathbf{e}\}, \quad \text{and} \quad \gamma_0^{\text{cl}} = \frac{q^2\omega_0}{mc^2\epsilon_0}\text{Im}\{\mathbf{e}^* \cdot \mathbf{G}(0, 0; \omega_0) \cdot \mathbf{e}\}\,, \tag{2.10}$$

where $\mathbf{e}$ is the unit vector pointing along the dipole. The imaginary term in the denominator corresponds to damping term in the equations of motion of the oscillator. Therefore, the self-interaction of the atom through the electromagnetic field

results in a shift Δ^{cl} on the resonance frequency of the atom and radiative decay at a rate γ_0^{cl}. Note that the real part of the Green's function diverges at $\mathbf{r} = \mathbf{r}_i$. This is not surprising because we are assuming a point dipole and the electromagnetic field diverges at the dipole's position. Since we are lacking knowledge of the system, we cannot accurately calculate its self-energy. Therefore, we will use the experimentally observed value for the resonance frequency ω_0 and set Δ^{cl} to zero. The imaginary part, on the other hand, is finite, since

$$\text{Im}\{\mathbf{G}(0,0;\omega_0)\} = \frac{\omega_0}{6\pi c}\mathbf{I}\,, \tag{2.11}$$

where $\mathbf{I}$ is the identity tensor, and therefore

$$\gamma_0^{\text{cl}} = \frac{q^2\omega_0^2}{6\pi m c^3 \epsilon_0} \tag{2.12}$$

We now consider multiple dipoles. To simplify the discussion, we assume that they are all oriented in the same direction and project Eq. (2.5). The dipole moment of an atom now reads $d_i(\omega) = \alpha(\omega)E_0(\mathbf{r},\omega) + \frac{1}{\epsilon_0}\frac{\omega^2}{c^2}\sum_j \alpha(\omega)G(\mathbf{r}_i,\mathbf{r}_j;\omega)d_j(\omega)$, where $d_i(\omega) = \alpha(\omega)\mathbf{e}\cdot\mathbf{E}(\mathbf{r}_i,\omega)$, $E_0(\mathbf{r},\omega) = \mathbf{e}\cdot\mathbf{E}_0(\mathbf{r},\omega)$ and $G(\mathbf{r},\mathbf{r}_i;\omega) = \mathbf{e}\cdot\mathbf{G}(\mathbf{r},\mathbf{r}_i;\omega)\cdot\mathbf{e}$. For the case of multiple radiative atoms a solution in the style of Eq. (2.8) would now require inverting a matrix in which the diagonal elements are the dipoles self-interaction, and the off-diagonal elements contain electric-field-mediated interactions between the dipoles proportional to $G(\mathbf{r}_i,\mathbf{r}_j;\omega)d_j(\omega)$. If the dipoles are close to each other, the interactions are significant, and the system can be diagonalized into collective dipole emission states, with modified resonance energies and emission rates. Interestingly, the light scattered by an atom modifies the electromagnetic environment that the rest of the atoms perceive. These photon-mediated interactions are the basis of this thesis, as they lead to the different collective effects that we leverage to enhance and control the atom–light interaction. We postpone the discussion of this phenomena and its implications for section 2.2, after we have introduced the quantum formalism.

Assuming that the driving field is weak, the steady state distribution of the scattered field is the same computing it both with classical dipoles or quantum emitters, since the radiated field of quantum emitters obeys the same Maxwell equations. For stronger input fields, however, the quantum emitters will saturate and the system will behave non-linearly. The classical description will thus fall short to capture the physics of quantum emitters. In the following sections, we derive the quantum version of the input-output formula in Eq. (2.5).

2.1.2 Quantization of the electromagnetic field

One way to quantize the electromagnetic field in vacuum is by constructing the Hamiltonian for the field and associating with each pair of a generalized coordinate and its canonically conjugate momentum to operators with commutator $i\hbar$. Here, we outline this procedure and refer the reader to [17] for a more detailed analysis.

To get rid of redundant dynamical variables in the standard Hamiltonian, we choose the Coulomb Gauge, for which the longitudinal component of the vector potential is zero. In the absence of static charges, the Coulomb potential is zero, which means that the longitudinal components of the electric and magnetic fields are also zero. Therefore, we assume that all vector fields in this section are purely transverse. Thus the fields depend on the vector potential and its conjugate variable as $-\epsilon_0\mathbf{E}(\mathbf{r},t) = \mathbf{\Pi}(\mathbf{r},t) = \epsilon_0\dot{\mathbf{A}}(\mathbf{r},t)$ and $\mathbf{B}(\mathbf{r},t) = \nabla\times\mathbf{A}(\mathbf{r},t)$. The Hamiltonian for the electromagnetic field reads

$$\begin{aligned} H &= \frac{1}{2}\int \mathrm{d}^3r \left[\epsilon_0\mathbf{E}(\mathbf{r},t)^2 + \frac{1}{\mu_0}\mathbf{B}(\mathbf{r},t)^2\right] \\ &= \frac{1}{2}\int \mathrm{d}^3r \left[\frac{1}{\epsilon_0}\mathbf{\Pi}(\mathbf{r},t)^2 + \frac{1}{\mu_0}(\nabla\times\mathbf{A}(\mathbf{r},t))^2\right] . \end{aligned} \tag{2.13}$$

It can be shown that at every point in the reciprocal half space there are two independent dynamical complex variables $A_\varepsilon(\mathbf{k})$ (and their respective conjugate momenta) obtained by expanding the vector potential for each value of $\mathbf{k}$ into two orthogonal unit vectors ε, ε' perpendicular to $\mathbf{k}$. The quantization of the field is obtained by upgrading these variables to operators and equating their commutation relations to the classical ones, such that $\dot{\hat{\mathbf{A}}}(\mathbf{r}) = -i[\hat{\mathbf{A}}(\mathbf{r}), \hat{H}]$ and the time evolution satisfies Maxwell's equations.

The vector potential can be written in terms of a set of independent variables $\alpha_\varepsilon(\mathbf{k},t)$, known as normal variables, which for the free field are pure harmonic oscillators describing a normal vibrational mode of the field. Moreover, they are independent for the full reciprocal space, since $\alpha^*_\varepsilon(\mathbf{k},t) \neq \alpha_\varepsilon(-\mathbf{k},t)$, unlike the vector potential. After quantization, these become the annihilation and creation operators, $\hat{a}_k$ and $\hat{a}^\dagger_k$, for the harmonic oscillator associated with the mode $\mathbf{k}\varepsilon$, where the index $k \leftrightarrow (\mathbf{k},\varepsilon)$. They satisfy the commutation relations $[\hat{a}_\varepsilon(\mathbf{k}), \hat{a}^\dagger_\varepsilon(\mathbf{k}')] = \delta_{\varepsilon\varepsilon'}\delta(\mathbf{k}-\mathbf{k}')$, $[\hat{a}_\varepsilon(\mathbf{k}), \hat{a}_\varepsilon(\mathbf{k}')] = 0$ and $[\hat{a}^\dagger_\varepsilon(\mathbf{k}), \hat{a}^\dagger_\varepsilon(\mathbf{k}')] = 0$. The electric field may now be written in terms of the eigenmodes as

$$\hat{\mathbf{E}}(\mathbf{r},t) = i\sum_k \sqrt{\frac{\omega_k}{2\epsilon_0}}\left[\mathbf{u}_k(\mathbf{r})\,\hat{a}_k e^{-i\omega_k t} - \mathbf{u}^*_k(\mathbf{r})\,\hat{a}^\dagger_k e^{i\omega_k t}\right] , \tag{2.14}$$

where the mode functions $\mathbf{u}_k(\mathbf{r})$ are the orthonormal, $\int \mathrm{d}^3r\,\mathbf{u}^*_k(\mathbf{r})\cdot\mathbf{u}_{k'}(\mathbf{r}) = \delta_{kk'}$ so-

lutions to the free field wave equation, $(\nabla^2 + \omega_k^2/c^2)\mathbf{u}_k(\mathbf{r}) = 0$, determined by the boundary conditions of the field. This form of expressing the fields reduces the field Hamiltonian to the form

$$\hat{H}_{\mathrm{EM}} = \sum_k \omega_k \left(\hat{a}_k^\dagger \hat{a}_k + \frac{1}{2}\right) . \tag{2.15}$$

2.1.3 Electric dipole interaction

We are interested in regimes in which the interaction of an atom with the electromagnetic field is dominated by the electric dipole transition. This is often true in the optical regime, in the absence of strong magnetic fields and assuming only low-lying excitations. Unless stated otherwise, we take the simplest model of an atom consisting of a two-level system. The interaction of an atom with the electromagnetic field reads [17]

$$\hat{H}_{\mathrm{I}} = -\hat{\mathbf{d}}_i(t) \cdot \hat{\mathbf{E}}(\mathbf{r}_i, t) , \tag{2.16}$$

where $\hat{\mathbf{d}}_i$ is the atomic dipole operator, which we can write as $\hat{\mathbf{d}} = (\mathbf{d}^* \hat{\sigma}^+ + \mathbf{d}\hat{\sigma}^-)$, by projecting the dipole operator to write it in terms of the matrix elements $\mathbf{d} = \langle g|\hat{\mathbf{d}}|e\rangle$, and the raising and lowering operators $\hat{\sigma}^+ = \hat{\sigma}^{-\dagger} = |e\rangle\langle g|$. The diagonal matrix elements are both zero due to the odd parity of the dipole operator. Eq. (2.16) is valid in the electric-dipole (or long-wavelength) approximation, in which the electric field is evaluated at the atom's center-of-mass position $\mathbf{r}_i$ by assuming that the variation of the electric field over the scale of the atomic size is negligible.

2.1.4 Quantum input-output equation

In this section, we derive the general input-output relation [18] for the electric field involving the radiation of the dipole operators. Using a form of Weisskopf–Wigner theory, we derive the Heisenberg equation of motion of the photonic operators, and solve them in the Markov approximation.

The Heisenberg equations of motion for the field operators under the effect of the full Hamiltonian

$$\hat{H} = \hat{H}_{\mathrm{EM}} + \hat{H}_{\mathrm{at}} + \hat{H}_{\mathrm{I}} , \tag{2.17}$$

where

$$\hat{H}_{\mathrm{at}} = \sum_i \omega_i \hat{\sigma}_i^+ \hat{\sigma}_i^- \tag{2.18}$$

read

$$\dot{\hat{a}}_k(t) = -i\omega_k \hat{a}_k(t) + \sum_i \sqrt{\frac{\omega_k}{2\epsilon_0}} \mathbf{u}_k^*(\mathbf{r}_i) \cdot \hat{\mathbf{d}}(t) . \tag{2.19}$$

To find a solution, we perform a Laplace transform, in which we define a purely imaginary variable $s = -i\omega$, such that $f(\omega) = \mathcal{L}\{f(t)\}(-i\omega)$. The equation of motion of the annihilation operators becomes

$$i(\omega_k - \omega)\hat{a}_k(\omega) = \hat{a}_k(t=0) + \sum_i \sqrt{\frac{\omega_k}{2\epsilon_0}}\mathbf{u}_k^*(\mathbf{r}_i)\cdot\hat{\mathbf{d}}(\omega)\,. \tag{2.20}$$

By substituting the above expressions into Eq. (2.14), we obtain

$$\hat{\mathbf{E}}(\mathbf{r},\omega) = \hat{\mathbf{E}}_0(\mathbf{r},\omega) + \sum_{ki}\frac{1}{2\epsilon_0}\frac{\omega_k}{\omega_k-\omega}\left[\mathbf{u}_k(\mathbf{r})\otimes\mathbf{u}_k^*(\mathbf{r}_i) + \mathbf{u}_k^*(\mathbf{r})\otimes\mathbf{u}_k(\mathbf{r}_i)\right]\cdot\hat{\mathbf{d}}(\omega)\,, \tag{2.21}$$

where the explicit time dependence in Eq. (2.14) has been absorbed into $\hat{a}_k(t)$. Here, $\mathbf{E}_0(\mathbf{r},\omega)$ is the free-field solution without the atoms, which follows from the input field that sets the initial conditions, $\hat{a}_k(t=0)$, in Eq. (2.20). Due to the time-reversal symmetry that relates forward and backward propagating modes, the mode functions satisfy $\mathbf{u}_k^*(\mathbf{r}) = \mathbf{u}_{-k}(\mathbf{r})$. Applying this identity to the equation above and using that $\omega_k = \omega_{-k}$ yields

$$\hat{\mathbf{E}}(\mathbf{r},\omega) = \hat{\mathbf{E}}_0(\mathbf{r},\omega) + \sum_{ki}\frac{1}{\epsilon_0}\frac{\omega_k^2}{\omega_k^2-\omega^2}\mathbf{u}_k(\mathbf{r})\otimes\mathbf{u}_k^*(\mathbf{r}_i)\cdot\hat{\mathbf{d}}(\omega)\,, \tag{2.22}$$

Since the eigenmodes are orthogonal and complete, the Green's function in Eq. (2.3) can be decomposed into them. By using the completeness relation, it is possible to write this decomposition solely in terms of the transverse modes [19–21]

$$\mathbf{G}(\mathbf{r},\mathbf{r}';\omega) = \sum_k \frac{c^2}{\omega^2}\frac{\omega_k^2}{\omega_k^2-\omega^2}\mathbf{u}_k(\mathbf{r})\otimes\mathbf{u}_k^*(\mathbf{r}') - \frac{c^2}{\omega^2}\frac{\delta(\mathbf{r}-\mathbf{r}')}{\epsilon_0}\mathbf{I}\,, \tag{2.23}$$

where $\mathbf{I}$ is the identity matrix. We will omit the term that only contributes to the real part of the self Green's function ($\mathbf{r} = \mathbf{r}'$) which, as already discussed, we will absorb into the resonant energy of the atoms. Therefore, the expression of the electric field after solving for the photonic modes reads

$$\hat{\mathbf{E}}(\mathbf{r},\omega) = \hat{\mathbf{E}}_0(\mathbf{r},\omega) + \frac{1}{\epsilon_0}\frac{\omega^2}{c^2}\sum_i \mathbf{G}(\mathbf{r},\mathbf{r}_i;\omega)\cdot\hat{\mathbf{d}}(\omega)\,. \tag{2.24}$$

We recovered the classical solution Eq. (2.5) with the field and dipole upgraded to operators. As already anticipated when discussing the classical case, assuming a weak drive such that the atoms stay in the linear (non-saturated) regime, the scattering of light by the atoms will be the same than that of classical point scatterers.

REAL-TIME INPUT-OUTPUT EQUATION

We will now invert the Laplace transform to obtain the real time expression for the electric field scattered by the atoms, $\hat{\mathbf{E}}(\mathbf{r},t) = \frac{1}{2\pi}\int_{-\infty}^{\infty} \mathrm{d}\omega\, \hat{\mathbf{E}}(\mathbf{r},\omega)e^{-i\omega t}$. Because $\hat{\mathbf{E}}(\mathbf{r},t)$ is real, we know that $\hat{\mathbf{E}}^*(\mathbf{r},\omega) = \hat{\mathbf{E}}(\mathbf{r},-\omega)$. Thus, we only need to consider the positive frequency part of the electric field $\hat{\mathbf{E}}^+(\mathbf{r},\omega) = \hat{\mathbf{E}}(\mathbf{r},\omega)\theta(\omega)$. Therefore, from Eq. (2.24), we have

$$\hat{\mathbf{E}}^+(\mathbf{r},t) = \hat{\mathbf{E}}_0^+(\mathbf{r},t) + \frac{1}{2\pi}\sum_i \int_0^\infty \mathrm{d}\omega\, \frac{\omega^2}{\epsilon_0 c^2}\mathbf{G}(\mathbf{r},\mathbf{r}_i;\omega)\cdot\hat{\mathbf{d}}(\omega)\, e^{-i\omega t}\,. \tag{2.25}$$

Next, we write $\hat{\mathbf{d}}(\omega)$ as an integral over time and move to a frame rotating with the atoms frequency $\tilde{\sigma}_i^-(t) = \hat{\sigma}_i^- e^{i\omega_i t}$, such that $\tilde{\sigma}_i^-(t)$ evolves slowly. The above expression becomes

$$\begin{aligned}\hat{\mathbf{E}}^+(\mathbf{r},t) = \hat{\mathbf{E}}_0^+(\mathbf{r},t) + \sum_i \frac{1}{2\pi}\int_0^\infty \mathrm{d}\,\omega \frac{\omega^2}{\epsilon_0 c^2}\mathbf{G}(\mathbf{r},\mathbf{r}_i;\omega)e^{-i\omega_i t} \\ \times \int_{-\infty}^{\infty}\mathrm{d}\tau\left[\mathbf{d}_i\,\tilde{\sigma}_i^-(\tau)e^{i(\omega-\omega_i)(\tau-t)} + \mathbf{d}_i^*\,\tilde{\sigma}_i^+(\tau)e^{i(\omega+\omega_i)(\tau-t)}\right]\,.\end{aligned} \tag{2.26}$$

Since the frequency is always positive, the last term of the above equation oscillates fast for all ω, so we can neglect it in the rotating wave approximation. In addition, to solve the time integral we make a Markov approximation, also known as the Weisskopf–Wigner approximation, and assume that after computing the frequency integral, the time integral only contributes over a small correlation time τ_c [22]. For a τ_c much shorter than the time scale of the atomic dynamics, we can approximate $\tilde{\sigma}^-(\tau) \simeq \tilde{\sigma}^-(t)$. Under these approximations, the time integral becomes simply $\int_{-\infty}^{\infty}\mathrm{d}\tau e^{i(\omega-\omega_i)\tau} = 2\pi\delta(\omega-\omega_i)$, yielding

$$\hat{\mathbf{E}}^+(\mathbf{r},t) = \hat{\mathbf{E}}_0^+(\mathbf{r},t) + \frac{1}{\epsilon_0}\frac{\omega_0^2}{c^2}\sum_i \mathbf{G}(\mathbf{r},\mathbf{r}_i;\omega_0)\cdot\mathbf{d}_i\,\hat{\sigma}_i^-(t). \tag{2.27}$$

The Markov approximation is justified because the atoms only have a significant optical response in a narrow range determined by their linewidth, $\gamma_0 \ll \omega_i$, and the spread of atomic resonance frequencies, which we also assume to be of order of γ_0. Since the vacuum Green's function has a small dispersion over this relevant frequency range around ω_i, the integral over frequency gives only significant values for a small τ_c. In fact, if $\omega^2\mathbf{G}(\omega)$ was constant for all ω, the solution to the frequency integral would be a Dirac delta distribution $\delta(t-\tau)$, and $\tau_c \to 0$. Additionally, for the Markov approximation to hold with multiple atoms, radiation must take a much shorter time to travel between atoms than any other time-scale, such that we can

neglect retardation effects.

In Eq. (2.27), the total field is separated into the input field and the field scattered by the emitters. Here, the input field is a quantum operator. We assume that the input field consists of a classical drive with optical frequency ω_L and a slowly varying, spatially dependent envelope $\mathbf{E}_0^+(\mathbf{r},t)$, and the quantum vacuum fluctuations $\delta\hat{\mathbf{E}}_0^+(\mathbf{r},t)$,

$$\hat{\mathbf{E}}_0^+(\mathbf{r},t) = \mathbf{E}_0^+(\mathbf{r},t)e^{i\omega_L t} + \delta\hat{\mathbf{E}}_0^+(\mathbf{r},t)\,, \tag{2.28}$$

where $\mathbf{E}_0^+(\mathbf{r},t)$ without the hat indicates the classical expectation value.

In the next section, we use Eq. (2.27) to eliminate the photonic bath and obtain an effective description that only includes atomic internal state dynamics. For the cases in which we are also interested in the scattered field, we can use Eq. (2.27) to reconstruct it from the solution to the atomic dynamics.

2.2 Effective light-mediated dynamics of an atomic ensemble

The effective dynamics of an atomic ensemble coupled to a continuum of quantized electromagnetic modes was first derived in [23] and the resulting collective atom radiation in [24]. Here, we have been doing a similar treatment, in which we describe the effective dynamics of the atomic ensemble by treating atoms and fields as quantum states and compute the field propagation using Maxwell's equations. In the electric-dipole and rotating-wave approximation, and in the Born-Markov regime, the photonic environment can be eliminated yielding a master equation for the atomic operators. We have, in fact, done most of the heavy-lifting in the previous section, after obtaining an expression to construct the total electric field in terms of the dipole operators, Eq. (2.27). In this section, we derive the master equation that describes the light-mediated atom dynamics by constructing the Heisenberg equations of motion for the atomic operators and using Eq. (2.27) to eliminate the photonic bath. We then discuss the resulting collective dynamics through the simplest case of two nearby atoms, before we proceed to solve the spectrum of subwavelength atom arrays in Section 2.2.3.

2.2.1 Master equation

The Heisenberg equation of motion for a dipole operator $\hat{Q}$ which commutes with all photonic operators under the Hamiltonian Eq. (2.17) in the rotating wave approxi-

mation reads

$$\begin{aligned}\dot{\hat{Q}} =& -i\sum_i \omega_i[\hat{Q},\hat{\sigma}_i^+\hat{\sigma}_i^-] \\ &+ i\sum_i [\hat{Q},\hat{\sigma}_i^+]\mathbf{d}_i^*\cdot\hat{\mathbf{E}}^+(\mathbf{r}_i,t) + i\sum_i \hat{\mathbf{E}}^-(\mathbf{r}_i,t)\cdot\mathbf{d}_i[\hat{Q},\hat{\sigma}_i^-]\,,\end{aligned} \tag{2.29}$$

where we use normal ordering with photonic annihilation operators on the right and creation operator on the left, which is convenient when evaluating expectation values with initial radiation states. Plugging in the solution for the total electric field in the Markov approximation Eq. (2.27), we obtain

$$\begin{aligned}\dot{\hat{Q}} =& -i\sum_{ij}\left(\omega_i\delta_{ij}+\Delta_{ij}\right)[\hat{Q},\hat{\sigma}_i^+\hat{\sigma}_j^-] + \sum_{ij}\Gamma_{ij}\left(\hat{\sigma}_i^+\hat{Q}\hat{\sigma}_j^- - \frac{1}{2}\{\hat{Q},\hat{\sigma}_i^+\hat{\sigma}_j^-,\}\right) \\ &+ i\sum_i\left([\hat{Q},\hat{\sigma}_i^+]\mathbf{d}_i^*\cdot\hat{\mathbf{E}}_0^+(\mathbf{r}_i,t) + \text{h.c.}\right)\,,\end{aligned} \tag{2.30}$$

where we defined the Hermitian matrices

$$\Delta_{ij} = -\frac{\omega_0^2}{\epsilon_0 c^2}\,\mathbf{d}_i^*\cdot\text{Re}\{\mathbf{G}(\mathbf{r}_i,\mathbf{r}_j;\omega_0)\}\cdot\mathbf{d}_j \tag{2.31}$$

$$\Gamma_{ij} = 2\frac{\omega_0^2}{\epsilon_0 c^2}\,\mathbf{d}_i^*\cdot\text{Im}\{\mathbf{G}(\mathbf{r}_i,\mathbf{r}_j;\omega_0)\}\cdot\mathbf{d}_j\,. \tag{2.32}$$

As defined in Eq. (2.28), the input field $\hat{\mathbf{E}}_0$ contains a classical drive and a quantum noise term, related to the field's vacuum fluctuations. The above equations are known as the Heisenberg-Langevin equations [18] due to their analogy with classical stochastic systems. To find the associated master equation, we go back to the Schrödinger picture and compute the expectation value of an operator $\hat{Q}$ for a system represented by a density matrix $\hat{\rho}$. We assume that we can separate the density operator as the product between the dipoles and the photonic bath $\hat{\rho} = \hat{\rho}_\text{S}\otimes\hat{\rho}_\text{B}$, given that the photons are initially in a coherent state and that $\delta\mathbf{E}_0^+(\mathbf{r},t)$ just annihilates the state of the bath. Thus, if we trace out $\hat{\rho}_\text{B}$, the quantum noise terms of Eq. (2.30) will vanish, leaving an equation of motion for the atoms driven by a classical field.

To obtain the master equation, we use that the expectation value of an arbitrary operator is $\langle\hat{O}(t)\rangle = \text{Tr}[\hat{O}(t)\hat{\rho}_\text{S}(0)]$ and that, using the cyclic property of the trace,

$$\langle\hat{O}(t)\rangle = \text{Tr}[\hat{O}(0)\hat{\rho}_\text{S}(t)]\,. \tag{2.33}$$

With this last identity, we can write $\langle\dot{\hat{Q}}(t)\rangle = \text{Tr}[\dot{\hat{Q}}(0)\hat{\rho}_\text{S}(t)]$. Using the cyclic property

of the trace again and Eq. (2.30), we can rewrite this expression as

$$\begin{aligned}\langle\dot{\hat{Q}}(t)\rangle = \mathrm{Tr}\Bigg[\hat{Q}(0)\Bigg[&-i\sum_{ij}\left(\omega_i\delta_{ij}+\Delta_{ij}\right)[\hat{\sigma}_i^+\hat{\sigma}_j^-,\hat{\rho}_\mathrm{S}(t)]\\&+\sum_{ij}\Gamma_{ij}\left(\hat{\sigma}_j^-\hat{\rho}_\mathrm{S}(t)\hat{\sigma}_i^+-\frac{1}{2}\{\hat{\sigma}_i^+\hat{\sigma}_j^-,\hat{\rho}_\mathrm{S}(t)\}\right)\\&+i\sum_i\left([\hat{\sigma}_i^+,\hat{\rho}_\mathrm{S}(t)]\mathbf{d}_i^*\cdot\hat{\mathbf{E}}_0^+(\mathbf{r}_i,t)+\mathrm{h.c.}\right)\Bigg]\Bigg].\end{aligned} \tag{2.34}$$

Evaluating Eq. (2.33) with $\hat{Q}(t)$ and taking the time derivative on both sides yields $\langle\dot{\hat{Q}}(t)\rangle = \mathrm{Tr}[\hat{Q}(0)\dot{\hat{\rho}}_\mathrm{S}(t)]$. By comparing this last expression with Eq. (2.34), one can extract the master equation for the atomic system

$$\dot{\hat{\rho}}_\mathrm{S}(t) = -i[\mathcal{H},\hat{\rho}_\mathrm{S}(t)]+\mathcal{L}[\hat{\rho}_\mathrm{S}(t)]\,, \tag{2.35}$$

where the unitary dynamics are described by the Hermitian Hamiltonian

$$\mathcal{H} = \sum_{ij}\left[(\omega_i-\omega_\mathrm{L}\delta_{ij}+\Delta_{ij}\right]\hat{\sigma}_i^+\hat{\sigma}_j^- - \sum_i\left(\Omega_i\hat{\sigma}_i^+ + \mathrm{h.c.}\right), \tag{2.36}$$

and the dissipative Lindbladian is

$$\mathcal{L}[\hat{\rho}_\mathrm{S}] = \sum_{ij}\Gamma_{ij}\left(\hat{\sigma}_j^-\,\hat{\rho}_\mathrm{S}\,\hat{\sigma}_i^+ - \frac{1}{2}\{\hat{\sigma}_i^+\hat{\sigma}_j^-,\hat{\rho}_\mathrm{S}\}\right), \tag{2.37}$$

where we defined the local Rabi frequencies $\Omega_i(t) = \mathbf{d}_i^*\cdot\mathbf{E}_0^+(\mathbf{r}_i,t)$ and got rid of the explicit time dependence of the drive term in Eq. (2.28) by moving to a frame rotating with the drive. This transformation introduced a global energy shift $-\omega_\mathrm{L}$ to the Hamiltonian.

Physically, the off-diagonal element Δ_{ij} is the rate of an excitation being coherently exchanged between dipoles mediated by the emission and absorption of a photon. The term Γ_{ii} gives the spontaneous emission of the single dipoles, $\gamma_0 = |\mathbf{d}|^2\omega_0^3/3\pi c^3\epsilon_0$. Due to interference, the dipoles will decay collectively differently as they would do individually. This redistribution of the decay rates is determined by the off-diagonal element Γ_{ij} and gives rise to eigenstates with enhanced or reduced free-space emission rates. Finally, the diagonal element Δ_{ii} shifts the resonance frequency of the dipoles. As already discussed for the classical case, we implicitly include it in the energy of the emitters and set $\Delta_{ii} = 0$.

2.2.2 Effective Hamiltonian

The dynamics of the system can analogously be described by evolving an effective Hamiltonian that resembles that of a spin model with XY interactions

$$\hat{H}_{\text{eff}} = \sum_{i,j} \left[(\omega_i - \omega_L)\delta_{ij} + \Delta_{ij} - \frac{i}{2}\Gamma_{ij} \right] \hat{\sigma}_i^+ \hat{\sigma}_j^- - \sum_i \left(\Omega_i \hat{\sigma}_i^+ + \text{h.c.} \right), \tag{2.38}$$

together with stochastic quantum jump operators [25–27]. In the absence of a driving term and within the single excitation sector, as we consider for this thesis unless indicated otherwise, the dynamics of the system are completely characterized by this non-Hermitian Hamiltonian. Under these assumptions, a quantum jump prepares the system in the collective ground state which does not evolve under the action of Eq. (2.38). In presence of a weak drive, the non-Hermitian Hamiltonian will also capture the dynamics to the lowest order in Ω/γ_0. Therefore, for most of this thesis, we will neglect the quantum jumps and compute the dynamics of the system by evolving the non-Hermitian Hamiltonian. We can obtain the eigenstates of the system by diagonalizing Eq. (2.38). The real part of the eigenvalue will give its resonant energy, and its imaginary part its collective decay rate.

We typically use the free-space decay rate of a single atom as the energy unit, so it is more practical to express Δ_{ij} and Γ_{ij} as

$$\Delta_{ij} - \frac{i}{2}\Gamma_{ij} = -\frac{3\pi c}{\omega_0}\sqrt{\gamma_i \gamma_j}\, \mathbf{e}_i^* \cdot \mathbf{G}(\mathbf{r}_i, \mathbf{r}_j; \omega_0) \cdot \mathbf{e}_j \,, \tag{2.39}$$

where $\mathbf{e}_i = \mathbf{d}_i/|\mathbf{d}_i|$ are unit vectors corresponding to the polarization of the dipole transition.

2.2.3 Collective atomic eigenstates

As we derived in the previous section, an ensemble of N atoms will not interact with light in the same way as the combined effects of N independent atoms, since nearby dipoles experience strong photon-mediated interactions that modify their resonances. In the simplest case of two atoms, the eigenstates in the single-excitation sector are their symmetric and anti-symmetric superposition, $|eg\rangle \pm |ge\rangle$. The two states are separated by an energy $2\Delta_{12}$ and their decay rates are $\gamma_0 \pm \Gamma_{12}$. What this means in an experimental setting is that an optical absorption measurement would not be able to distinguish between the case of two identical atoms interacting with each other, or two independent atoms with different resonance energies and linewidths, as depicted in Fig. 2.1. While the far-field component of the scattered field (section 2.1.1) is mostly associated with absorption and emission of light, the

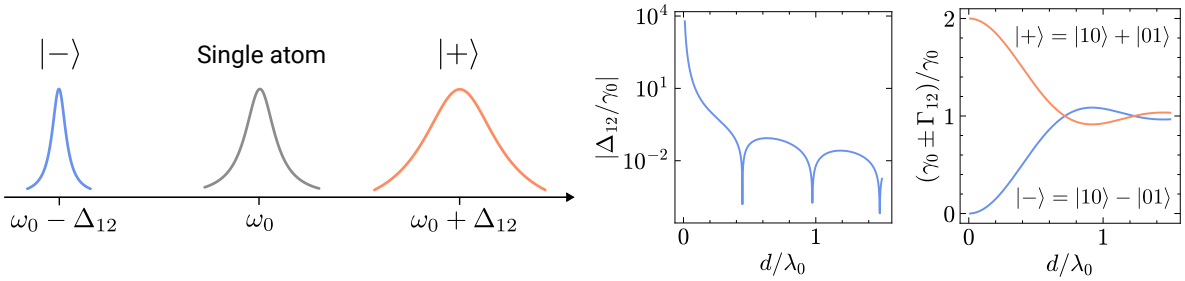

Figure 2.1: (left) Schematic depiction of an absorption experiment on one atom (center) or two nearby atoms (sides), where $|+\rangle$, $|-\rangle$ denote the eigenstate in which atoms are in-phase and out of phase, respectively. Two interacting atoms display energy splitting and modified decay rates. (right) Energy shift and collective decay rate of two atoms separated by a distance d.

near-field component hybridizes the atoms. Therefore, the collective response to light will be most significantly distinct for inter-atomic distances of the order of the wavelength of the resonant light, λ_0. In the limit of zero inter-atomic distance, the anti-symmetric state would become perfectly dark, exemplifying the perfect destructive interference of the emission of the two atoms, and the symmetric state would see its emission doubled owing to constructive interference. While this limit is obviously unattainable in practice, perfectly dark states, among other features, can be obtained with ordered arrays of atoms with a subwavelength lattice spacing, as we describe in the next section.

2.3 Subwavelength atom arrays

We now look into the case of periodic arrays of atoms and solve for their collective dipole eigenstates. In the subwavelength regime, the lattice spacing a is smaller than the wavelength of light associated to the optical dipole transition, $\lambda_0 = 2\pi/k_0 = 2\pi c/\omega_0$, as depicted in Fig. 2.2 for a one-dimensional array, for which the subwavelength condition is even stricter, as we discuss below. We solve the system for infinite lattices to illustrate the emergence of subradiant eigenstates before commenting on the extension to finite systems. Finally, we discuss key features of two-dimensional arrays.

2.3.1 Infinite lattices

We consider infinite arrays of identical atoms with free-space decay rate γ_0 and the same polarization, such that the system is translationally invariant under any lattice vector displacement. It follows that the eigenstates obey Bloch's theorem. For a single excitation, the eigenstates of Eq. (2.38) are spin waves with a well defined

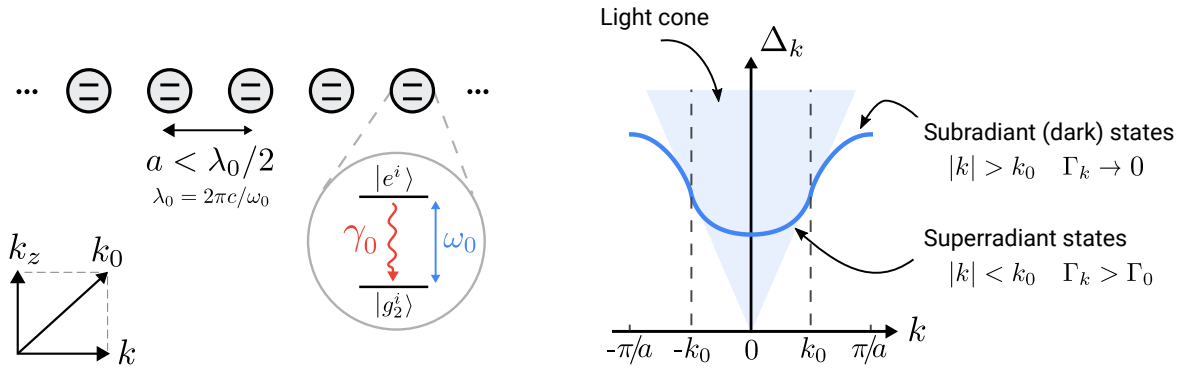

Figure 2.2: In Section 2.3 we solve for the collective energy and free-space decay rate for infinite periodic atom arrays. When $|\mathbf{k}| > k_0$, subradiant (dark) states appear with zero emission to free space.

quasimomentum $\mathbf{k}$. Thus, we can diagonalize Eq. (2.38) in terms of Bloch eigenmodes $\hat{\sigma}^-_{\mathbf{k}} = \frac{1}{\sqrt{N}}\sum_i \hat{\sigma}^-_i e^{-i\mathbf{k}\cdot\mathbf{r}_i}$. Allowing for the case of multiple parallel arrays, the Hamiltonian in reciprocal space reads

$$\begin{aligned}\hat{H} = \sum_{\mathbf{k},\alpha\beta}\left[(\omega_0-\omega_\mathrm{L})\delta_{\alpha\beta} + \Delta_{\alpha\beta}(\mathbf{k}) - \frac{i}{2}\Gamma_{\alpha\beta}(\mathbf{k})\right]\hat{\sigma}^+_{\mathbf{k}\alpha}\hat{\sigma}^-_{\mathbf{k}\beta} \\ - \sum_{\mathbf{k},\alpha}\left[\Omega(\mathbf{k};z^\alpha)\hat{\sigma}^+_{\mathbf{k}\alpha} + \mathrm{H.c.}\right],\end{aligned} \tag{2.40}$$

where α and β label the arrays. We defined $\Omega(\mathbf{k}) = \frac{1}{\sqrt{N}}\sum_i \mathbf{e}^*_\alpha \cdot \mathbf{E}^+_0(\mathbf{r}_i, z^\alpha)e^{-i\mathbf{k}\cdot\mathbf{r}_i}$, and

$$\Delta_{\alpha\beta}(\mathbf{k}) - \frac{i}{2}\Gamma_{\alpha\beta}(\mathbf{k}) = -\frac{3\pi\gamma_0}{k_0}\sum_i \mathbf{e}^*_\alpha \cdot \mathbf{G}_0(\mathbf{r}_i; z^{\alpha\beta})\cdot\mathbf{e}_\beta\, e^{-i\mathbf{k}\cdot\mathbf{r}_i}, \tag{2.41}$$

where z^α is the position in the orthogonal axis of the array α, and $z^{\alpha\beta}$ is the distance between α and β. We define the vectors $\mathbf{r}$ and $\mathbf{k}$ to be two-dimensional and parallel to a plane containing the array for a one-dimensional array, and on the plane of the array for a two-dimensional array.

To evaluate the sum in Eq. (2.41), we define first the Fourier transform of the Green's function

$$\mathbf{G}(\mathbf{k}; z^{\alpha\beta}) = \int \mathrm{d}\mathbf{r}\, \mathbf{G}(\mathbf{r}; z^{\alpha\beta})\, e^{-i\mathbf{k}\cdot\mathbf{r}}, \tag{2.42}$$

and its inverse Fourier transform

$$\mathbf{G}(\mathbf{r}; z^{\alpha\beta}) = \frac{1}{(2\pi)^2}\sum_{\mathbf{B}}\int \mathrm{d}\mathbf{k}\, \mathbf{G}(\mathbf{k}+\mathbf{B}; z^{\alpha\beta})\, e^{i(\mathbf{k}+\mathbf{B})\cdot\mathbf{r}} \tag{2.43}$$

where the sum runs over all reciprocal lattice vectors such that we can restrict $\mathbf{k}$ to the first Brillouin zone.

Using the differential form of the free-space Green's tensor

$$\mathbf{G}(\mathbf{r}_i, \mathbf{r}_j) = \frac{1}{4\pi}\left[\mathbb{1} + \frac{1}{k_0^2}\nabla_i \otimes \nabla_i\right] \frac{e^{ik_0|\mathbf{r}_i - \mathbf{r}_j|}}{|\mathbf{r}_i - \mathbf{r}_j|}\,, \tag{2.44}$$

the plane wave decomposition

$$\frac{e^{ik_0 r}}{r} = \frac{i}{2\pi}\int \mathrm{d}\mathbf{k}\, \frac{1}{k_z} e^{i\mathbf{k}\cdot\mathbf{r}} e^{ik_z|z|}\,, \tag{2.45}$$

where $k_z = \sqrt{k_0^2 - \mathbf{k}^2}$, and the Dirac delta representation in D dimensions, we can express the Green's function as a sum over reciprocal lattice vectors.

For a single one-dimensional array along the x direction (and setting $z = 0$) [28]

$$\mathbf{G}(\mathbf{k}) = \frac{i}{4\pi}\frac{1}{k_0^2 a}\sum_{\mathbf{B}}\int \mathrm{d}\, q_y\, \frac{1}{q_z}\left[k_0^2\mathbb{1} - \mathbf{q}\otimes\mathbf{q}\right]\,, \tag{2.46}$$

with $\mathbf{q} = [k + B_x, q_y, q_z \mathrm{sgn}(x)]$, and $q_z = \sqrt{k_0^2 - (k + B_x)^2 - q_y^2}$.

For one or multiple two-dimensional lattices in the $x - y$ plane, we obtain

$$\mathbf{G}(\mathbf{k}; z^{\alpha\beta}) = \frac{i}{2}\frac{1}{k_0^2 a^2}\sum_{\mathbf{B}} \frac{k_0^2\mathbb{1} - \mathbf{q}\otimes\mathbf{q}}{q_z}\, e^{iq_z|z^{\alpha\beta}|}\,, \tag{2.47}$$

with $\mathbf{q} = [k_x + B_x, k_y + B_y, q_z \mathrm{sgn}(z)]$ and $q_z = \sqrt{k_0^2 - |\mathbf{k} + \mathbf{B}|^2}$.

Putting all together, Eq. (2.41) becomes

$$\Delta_{\alpha\beta}(\mathbf{k}) - \frac{i}{2}\Gamma_{\alpha\beta}(\mathbf{k}) = -\frac{3\pi\gamma_0}{k_0 a^2}\sum_{\mathbf{B}} \hat{\mathbf{e}}_\alpha^* \cdot \mathbf{G}(\mathbf{k} + \mathbf{B}; z^{\alpha\beta}) \cdot \hat{\mathbf{e}}_\beta\,. \tag{2.48}$$

Eq. (2.48) is in general a complex quantity, but we defined $\Delta(\mathbf{k})$ and $\Gamma(\mathbf{k})$ such that they are Hermitian. For $\alpha = \beta$, they correspond to the energy dispersion and the decay rate of an array's eigenmodes with in-plane quasi-momentum $\mathbf{k}$, respectively, i.e., they represent the effective band structure of the arrays. For $\alpha \neq \beta$, they represent the coherent and dissipative interaction between $\mathbf{k}$ eigenmodes of different arrays. Note that interactions preserve the in-plane momentum.

We refer to [28] for the explicit expressions of $\Delta_{\alpha\alpha}(\mathbf{k})$ for 1D arrays. We compute Eq. (2.48) numerically for 2D arrays. The sum over reciprocal lattice vectors converges fast for $\Delta_{\alpha\neq\beta}(\mathbf{k})$ due to the exponential term in Eq. (2.47) being a real decaying function for $|\mathbf{k} + \mathbf{B}| > k_0$. On the other hand, $\Delta_{\alpha\alpha}(\mathbf{k})$ diverges as it includes the interaction of an atom with itself. We regularize the expression by subtracting the energy shift due to the atom self-interaction as we did with the real-space expression (see Appendix 2.A).

Because the anti-Hermitian part of the atoms' self-interaction is finite, $\Gamma_{\alpha\beta}$ converges for all cases. Note that for $|\mathbf{k}+\mathbf{B}| > k_0$, q_z is purely imaginary, for which Eq. (2.47) is purely real. Therefore, only a finite number of terms contribute to the collective decay rate of the array. Restricting ourselves to the reciprocal lattice vectors satisfying $|\mathbf{k}+\mathbf{B}| \leq k_0$, we obtain for the collective decay rate of a 1D array and atoms with a polarization parallel or perpendicular to the array

$$\frac{\Gamma^{\parallel}(\mathbf{k})}{\gamma_0} = \frac{3\pi}{2k_0^3 a} \sum_{\mathbf{B},|\mathbf{k}+\mathbf{B}|\leq k_0} \left[k_0^2 - (\mathbf{k}+\mathbf{B})^2\right] \tag{2.49}$$

$$\frac{\Gamma^{\perp}(\mathbf{k})}{\gamma_0} = \frac{3\pi}{4k_0^3 a} \sum_{\mathbf{B},|\mathbf{k}+\mathbf{B}|\leq k_0} \left[k_0^2 + (\mathbf{k}+\mathbf{B})^2\right] . \tag{2.50}$$

And for 2D arrays,

$$\frac{\Gamma^{\parallel}(\mathbf{k})}{\gamma_0} = \frac{3\pi}{k_0^3 a^2} \sum_{\mathbf{B},|\mathbf{k}+\mathbf{B}|\leq k_0} \frac{k_0^2 - |(\mathbf{k}+\mathbf{B})\cdot\mathbf{e}|^2}{\sqrt{k_0^2 - |\mathbf{k}+\mathbf{B}|^2}} \tag{2.51}$$

$$\frac{\Gamma^{\perp}(\mathbf{k})}{\gamma_0} = \frac{3\pi}{k_0^3 a^2} \sum_{\mathbf{B},|\mathbf{k}+\mathbf{B}|\leq k_0} \frac{|\mathbf{k}+\mathbf{B}|^2}{\sqrt{k_0^2 - |\mathbf{k}+\mathbf{B}|^2}} . \tag{2.52}$$

Dark eigenstates

From the above expressions follows that for $|\mathbf{k}| > k_0$ no term contributes to the sum and the decay rates are zero. Intuitively, conservation of momentum forbids array eigenstates with a momentum larger than that of a photon at frequency ω_0 from emitting. The out-of-plane momentum q_z becomes purely imaginary. The associated field, Eq. (2.27), is an evanescent field that decays exponentially away from the array. This condition can be satisfied in one-dimensional arrays for lattice spacings $a < \lambda_0/2$, and $a < \lambda_0/\sqrt{2}$ for two-dimensional arrays.

The dispersion relation and collective decay rates of one- and two-dimensional arrays are thoroughly discussed in [28]. In Fig. 2.3, we show the spectrum for example arrays used in Chapter 3 and Chapter 4. Here we can clearly identify the subradiant eigenstates.

2.3.2 Finite lattices

The solutions for the collective energies and decay rates for finite lattices, which we compute numerically, have well-defined momenta in reciprocal space for sufficiently big arrays and their magnitudes are very well approximated by the solutions from infinite lattice at those momenta. Therefore, we often use the analytical expressions. We will discuss the differences between the two systems and, when required,

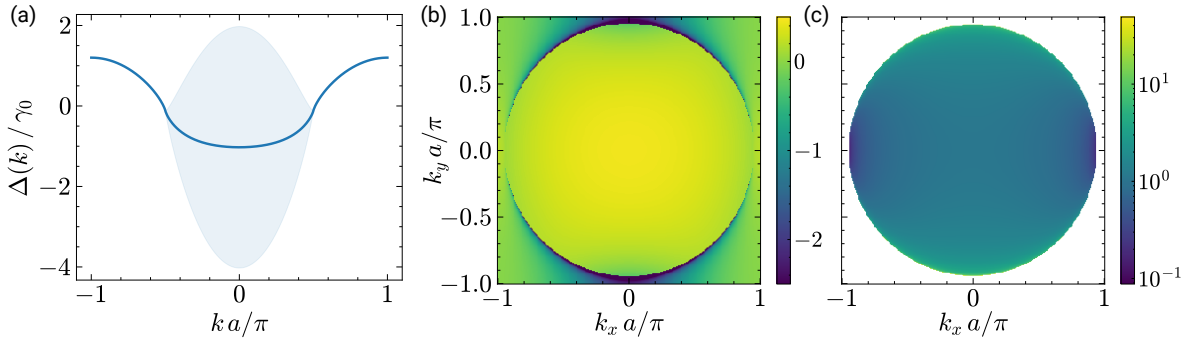

Figure 2.3: Dispersion relation and collective decay rate for infinite atom arrays. Both arrays show perfectly dark modes at larger $\mathbf{k}$. (a) The solid line shows $\Delta(k)$ for a one-dimensional array with lattice spacing $a = 0.25\lambda_0$ and polarization parallel to the array. The shaded area spans a range $\Delta(k) \pm \Gamma(k)$. We show $\Delta(\mathbf{k})/\gamma_0$ for a two-dimensional array with lattice spacing $a = 0.47\lambda_0$ and in-plane atom polarization along the x axis in (b), and $\Gamma(\mathbf{k})/\gamma_0$ in (c). The color axis in (b) has been truncated on the negative side to increase the resolution, as the band has a singularity on the light cone. The white region in (c) corresponds to the points in which the decay rate is exactly zero.

use more appropriate expressions in the following chapters, as they arise. The two main differences are firstly that the eigenstates in a finite lattice are discrete and well approximated (at least in the single-excitation subspace) by standing waves consisting of two counter-propagating spin waves [28]. Related to this, finite arrays have boundaries, which is relevant when studying the transport of an excitation. Secondly, subradiant states are not perfectly dark, with most of the scattered light originating from the ends of the arrays. Nevertheless, the states closer to the edge of the Brillouin zone stay highly subradiant. In [28] they observe a $\Gamma_{\mathbf{k}} \sim \gamma_0/N^3$ for the most subradiant states of a one-dimensional array, and even more advantageous scalings with N for two-dimensional arrays.

2.3.3 Planar arrays as resonant mirrors

We conclude our discussion of atom arrays by reviewing the reflection from a two-dimensional array of atoms [29, 30]. For this, we consider an infinite, regular lattice of identical atoms with transition frequency ω_0 and linearly polarized transition dipole moment. To study the scattering properties of the array, we solve the dynamics under Eq. (2.38) with a weak, monochromatic drive to obtain the steady state $\langle \sigma_{\mathbf{k}}^- \rangle = \Omega(\mathbf{k})/[\Delta(\mathbf{k}) - i\Gamma(\mathbf{k})/2]$. Using Eq. (2.27), we find that the amplitude reflection coefficient for an incident plane wave with in-plane momentum $\mathbf{k}$ is given by

$$r(\mathbf{k}, \omega_{\mathrm{L}}) = \frac{i\Gamma(\mathbf{k})/2}{\omega_0 - \omega_{\mathrm{L}} + \Delta(\mathbf{k}) - i\Gamma(\mathbf{k})/2}. \tag{2.53}$$

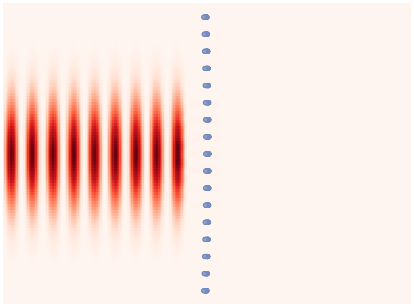

Figure 2.4: Steady-state electric field intensity for a two-dimensional subwavelength array driven at resonance with a weak classical field. The blue dots indicate the positions of the atoms. The incoming beam comes from the left.

Here, we assumed that the projection of the electric field onto the plane of the array is parallel to the transition dipole moment. The transmission coefficient is given by $t(\mathbf{k},\omega_{\mathrm{L}}) = 1 + r(\mathbf{k},\omega_{\mathrm{L}})$. We will frequently work with the intensity reflection and transmission coefficients $\mathcal{R} = |r|^2$ and $\mathcal{T} = |t|^2$, which by energy conservation satisfy $\mathcal{R} + \mathcal{T} = 1$ for an infinite array.

Eq. (2.53) holds if the lattice spacing is sufficiently small such that higher-order Bragg scattering is suppressed. Due to conservation of momentum, light will be scattered at specific angles, given by the incoming momentum and the incoming momentum plus a reciprocal lattice vector. Therefore, if all $|\mathbf{k} + \mathbf{B}| > k_0$, the emission of higher-order diffraction modes is suppressed and only the zeroth order mode survives, which corresponds to perfect reflection. For zero in-plane momentum (light impinging orthogonal to the array), the condition for perfect reflection is $a < \lambda_0$.

From Eq. (2.53), we see that there is an additional condition to have perfect reflection. For this, we need to tune the laser on resonance with a particular Bloch mode, $\omega_{\mathrm{L}} = \omega_0 + \Delta(\mathbf{k})$, such that $r(\mathbf{k},\omega_{\mathrm{L}}) = -1$ and $t(\mathbf{k},\omega_{\mathrm{L}}) = 0$. Atom arrays with subwavelength lattice spacings are thus excellent mirrors, albeit only over a narrow frequency range of width $\Gamma(\mathbf{k})$ centered around the collective resonance. From Eq. (2.51), at normal incidence ($\mathbf{k} = 0$) and in the absence of Bragg scattering, the linewidth is given by $\Gamma(0) = 3\pi\gamma_0/k_0^2a^2$.

The maximum of the reflection coefficient stays close to unity for finite arrays reflecting finite Gaussian beams. We discuss the matter in more detail in Chapter 4. In Fig. 2.4, we show the steady-state electric field intensity reflected by a finite array. We solve Eq. (2.38) in the steady state, i.e. $\langle\dot{\hat{\sigma}}^-(t)\rangle = 0$, and reconstruct the electric field using Eq. (2.27). Here we assume a weak field, such that the system stays in the unsaturated regime and $\langle\mathbf{E}^-(\mathbf{r})\mathbf{E}^+(\mathbf{r})\rangle \approx \langle\mathbf{E}^-(\mathbf{r})\rangle\langle\mathbf{E}^+(\mathbf{r})\rangle$. The field behind the mirror is indiscernible in this visualization.

2.4 Atoms coupled to a resonator

In this section we briefly motivate the need to enhance the atom-light interaction rate achievable in free-space and describe how the interaction can be enhanced using optical resonators. We then introduce the fields of waveguide and cavity QED and some of the basic concepts that will serve as a foundation for the following chapters.

2.4.1 Scattering cross-section and Purcell enhancement

The probability of interaction between an atomic dipole transition and a focused laser beam resonant with the transition frequency is given by the ratio of the resonant scattering cross-section of the atom over the area of the beam, $\sigma_{\text{sc}}/A_{\text{dif}}$, in the paraxial approximation. The scattering cross-section of an ideal point scatterer is proportional to the wave-length of the resonant light, $\sigma_{\text{sc}} = 3\lambda_0^2/2\pi$ [11], while the focusing of the beam is limited by the diffraction limit $A_{\text{dif}} \gtrsim \lambda_0^2$, which sets a limit on the efficiency of the interaction. The largest probability of atom-photon interaction achieved with far-field optics in free space is about a 10% [13].

The radiative properties of atoms depend on the local electromagnetic field, which can be modified by changing its boundary conditions. In the language of quantum electrodynamics, the emission rate of an atom depends on the density of modes of the electromagnetic field resonant with the atomic transition frequency, $\omega_0 = 2\pi c/\lambda_0$. For an atom in resonance with a resonator, Purcell showed that the spontaneous emission rate of an atom is enhanced by a factor $\sim Q\lambda_0^3/V$ [31], where Q is the quality factor of the resonator and V its mode volume.

The above relation follow readily from Fermi's Golden Rule. The transition rate $\Gamma_{i\to f}$ between an initial state $|i\rangle$ and a final state $|f\rangle$ reads

$$\Gamma_{i\to f}(\omega) = 2\pi|\langle f|\,\hat{H}_{\text{I}}\,|i\rangle|^2\rho(\omega)\,, \tag{2.54}$$

where $\rho(\omega)$ is the density of states of the electromagnetic field at frequency ω. $\hat{H}_{\text{I}}$ in this case is the electric dipole interaction introduced in Eq. (2.16). From this expression, the Purcell enhancement simply equals the ratio between the density of states due to the presence of some optical element and the density of states of the electromagnetic field in free space. The density of states of a large cavity can be approximated as $\rho_{\text{C}}(\omega) = Q/\omega V$ [32], while the density of states in free space is $\rho(\omega) = \omega^2/\pi^2c^3$. From this ratio, we recover Purcell's expression.

These expressions are valid in the Markovian regime, when interactions are weak and the atom's excitation decays monotonically into the environment. Nevertheless, as we describe below, figures of merit in the strong coupling regime depend on

the quality factor and the mode volume in a similar manner. Using the Jaynes-Cummings model, the rate of coherent transfer of population is determined by the coupling strength, whose magnitude to the power of two is proportional to the field intensity and thus inversely proportional to the mode volume. The rate of coherent dynamics must be compared to the rate of dissipative dynamics, which is inversely proportional to the quality factor. Therefore, the two desired features for an optical resonator are a high degree of spatial field confinement to increase the local per-photon intensity and a long photon lifetime. Next, we elaborate further on this in the context of the fields of waveguide and cavity QED.

2.4.2 Waveguide QED

In waveguide QED, light is confined to a nanophotonic guiding structure. Confining light to small dimensions increases the intensity of the field and, thus, the interaction probability with nearby atoms. In Fig. 2.5, we show a depiction of such a system, with atoms trapped near a nanofiber. The atoms interact with the propagating photons within the fiber owing to the evanescent field that forms outside, effectively emitting their excitation into that guided mode at a rate Γ_{1D}. The main figure of merit of this system is the Purcell factor, that compares the atom's emission into a guided mode with its emission into free space, $P = \Gamma_{1D}/\gamma_0$.

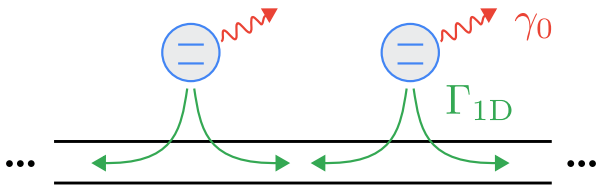

Figure 2.5: Schematic representation of atoms interacting with a waveguide. The main figure of merit of the system is the ratio between atom emission into the guided modes of the waveguide Γ_{1D} and free-space decay, known as Purcell factor $P = \Gamma_{1D}/\gamma_0$.

While typical optical fibers have a linear dispersion relation, the phenomenology becomes much richer when the dispersion relation of the waveguide is engineered into more complex shapes. One way to do this is by periodically modulating the dielectric profile of the waveguide along the propagation axis to make "photonic crystals" [33] that possess a band structure akin to solid crystals. Different physics arise when the emitter energy is inside the band of guided modes compared to when it lies in the band-gap. In Chapter 3, we consider these two regimes separately.

For atoms with a resonance energy within the band of the waveguide, emission into the guided modes with high Purcell factors can be obtained. Interestingly, the group velocity depends on the mode's quasimomentum through the dispersion relation $v_g = \mathrm{d}\omega/\mathrm{d}k$. Close to the band edge, the slope of the dispersion relation

approaches zero, for which slow light can be achieved. This increases the interaction probability with the atoms even further. Another possibility offered by these systems is the collective dissipation among multiple atoms. Because light is confined in one dimension, the probability that a photon emitted by one atom interacts with another atom along the waveguide is very high, allowing for collective behavior. In particular, with the right configuration to ensure constructive interference, the collective decay rate of the atoms can be enhanced.

Placing the resonance energy of the atoms within the band-gap allows to turn off the emission into the waveguide and gives rise to novel features. For instance, despite the suppressed emission, the interaction of the atoms with the field of the guided modes leads to the formation of atom–photon bound states. The spatial extend of the bound states grows as the detuning between the atom's resonant frequency and the edge of the band is reduced. This can be exploited to mediate coherent long-range interactions between distant atoms.

Therefore, beyond enhancing the efficiency of the interactions, waveguide QED offers a new paradigm for quantum atom-light interactions. For a comprehensive discussion of the topic, we refer the reader to [15].

2.4.3 Cavity QED

The interaction between a two-level atom and a single cavity mode within the rotating-wave approximation is described by the Jaynes-Cummings Hamiltonian

$$\hat{H}_{\text{cQED}} = \omega_{\text{a}}\hat{\sigma}^{+}\hat{\sigma}^{-} + \omega_{\text{c}}\hat{a}^{\dagger}\hat{a} - g\left(\hat{\sigma}^{+}\hat{a} + \hat{\sigma}^{-}\hat{a}^{\dagger}\right), \tag{2.55}$$

where we set $\hbar = 1$. Here, $\hat{\sigma}^{\pm}$ are the raising and lowering operators of the atom and $\hat{a}$ is the photon annihilation operator. The frequencies ω_{a} and ω_{c} refer to the resonant frequencies of the atom and the cavity, respectively. The coupling strength g is given by $g = \mathbf{d} \cdot \mathbf{E}_0$, where $\mathbf{d}$ is the transition dipole moment of the atom and $\mathbf{E}_0$ is the electric field due to a single photon at the location of the atom. The magnitude of the single-photon field can be expressed as $|\mathbf{E}_0| = \sqrt{\hbar\omega_{\text{c}}/2\epsilon_0 V}\, u(\mathbf{r}_{\text{a}})$. Here, $u(\mathbf{r}_{\text{a}})$ is the mode function of the electric field at the location of the atom, normalized to 1 at the field maximum, and $V = \int \mathrm{d}^3\mathbf{r}\, u^2(\mathbf{r})$ is the cavity mode volume.

In addition to the coherent Hamiltonian dynamics, cavity QED systems are also subject to incoherent processes such as spontaneous emission and decay of the cavity field. In free space, the spontaneous emission rate of a two-level system is given by $\gamma_{\text{a}} = |\mathbf{d}|^2\omega_{\text{a}}^3/3\pi\epsilon_0\hbar c^3$. The presence of the cavity modifies this decay rate to γ_{3D}, where the subscript highlights that the rate is associated with emission into unconfined, three-dimensional modes as opposed to cavity-mediated decay. If the cavity

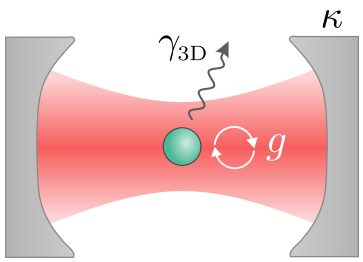

Figure 2.6: A cavity QED setup is characterized by the coupling strength g, the cavity decay rate κ, and the decay rate of the target atom into free space γ_{3D}. The main figure of merit of the system is the ratio between coherent and dissipative rates, known as the cooperativity $C = 4g^2/\kappa\gamma_{3D}$.

is composed of two mirrors with reflection coefficient $\mathcal{R}$ separated by a distance L, then the cavity field decays at a rate $\kappa = (1 - \mathcal{R})c/L$.

The performance of a cavity QED setup is governed by the strength of the coherent interaction, g, compared to the incoherent rates, κ and γ_{3D}. The relative strength of the coherent to incoherent rates is captured by the cooperativity

$$C = \frac{4g^2}{\kappa\gamma_{3D}}. \tag{2.56}$$

We highlight that the cooperativity is independent of the properties of the atom, i.e. the transition dipole moment and the transition frequency, when $\omega_a/\omega_c \approx 1$, which is the relevant regime for optical transitions.

The cooperativity compares the rates of coherent dynamics and dissipative dynamics in the strong coupling regime $g > \kappa, \gamma_{3D}$. In the bad cavity regime, $\kappa > g > \gamma_{3D}$, we recover Markovian dynamics in which the excitation of the atom decays into the cavity mode. In this regime, the cooperativity corresponds to the Purcell factor discussed above.

We refer the reader to review articles for a more comprehensive discussion [14, 34] on the field of cavity QED and its applications.

2.5 Adiabatic elimination of fast variables

Some physical phenomena depend on complex interactions between many players governed by many microscopic equations. Their macroscopic properties, however, might be described by a few variables. An example of this is the kinetic theory of gases, which can be described by a few macroscopic parameters, while the atomic interactions behind them are very fast and complex. In these types of problems, it is important to identify the different time-scales of the system. In many occasions, the fast dynamics can be eliminated. The result is a simplified set of equations in

which the slow variables incorporate the influence of the eliminated fast variables through a modified decay rate, energy shifts, or new effective couplings. We have, in fact, already performed such a procedure in Section 2.2, where we eliminated the photonic bath to find effective equations describing the atomic internal state dynamics. In that case, we had a noise variable that we assumed to be independent of the atomic internal dynamics so that we could write a master equation. Often, however, this will not be the case, as the variable to be eliminated and the variable of interest may be coupled.

In the next chapters, we aim to understand systems including many atoms with complex interactions in the language of waveguide and cavity QED, which can be described with a few parameters. Therefore, we will use techniques to eliminate the part of the atomic eigenstates that are not relevant for our description. There exist different possible methods to this end (see for instance [22, 35]). We will be using various approaches in this thesis, although they are in essence equivalent. We will introduce the methods as we need them and focus here on explaining the principle behind them and justifying their validity.

For an *adiabatic elimination*, one assumes that the fast dynamics equilibrate much faster than the slow dynamics, and remain thus in a quasi-equilibrium state. For the sake of example, let's associate fast and slow dynamics to the operators $\hat{a}$ and $\hat{b}$, respectively. Formally, the steady-state approximation is imposed by setting $\dot{\hat{a}}(t) \simeq 0$ and plug in the solution into the equation for $\dot{\hat{b}}(t)$. The timescale separation will often be justified when we eliminate fast-decaying eigenstates, compared to the long-lived subradiant eigenstates that we keep. In addition, the eliminated states are initialized with zero population for the dynamics that interest us, and the coupling with the slow variables is weak so that the fast subsystem can be treated independently. This approach is often known as "naive" adiabatic elimination, as inaccuracies may be introduced. A rigorous adiabatic elimination includes non-adiabatic corrections by defining a small parameter ϵ and expanding the solution for the fast variable in powers of the small parameter: $\hat{a} = \hat{a}^{(0)} + \epsilon\hat{a}^{(1)} + \epsilon^2\hat{a}^{(2)} + \dots$. We generally stop at the zeroth order. Nevertheless, we verify the validity of the elimination numerically.

In other related methods that we use, such as the resolvent operator method or solving in the Laplace domain, the weak couplings between slow and fast variables are treated perturbatively. Moreover, the fast degrees of freedom typically contribute poles that are far from the origin in the complex plane because they oscillate fast (we work in a rotating frame defined by the slow eigenstates) and often exhibit large decays. In the *pole approximation*, we simplify the analysis by neglecting the contributions of these poles and fix the implicit energy in the self-consistent equations to the resonance energy of the states contributing to the slow dynamics.

2.6 Experimental considerations

In this section, we introduce optical lattices as a platform to achieve subwavelength atom arrays and discuss the trapping potential, which will become relevant when accounting for motion and disorder in Chapter 4. We then introduce the concept of using a Raman transition to modify an atom's linewidth.

2.6.1 Optical lattices

In Section 2.1 we discussed atom-light interaction, which scaled with the polarizability of the specific dipole transition. Two types of mechanical forces arise from this interaction: the dipole force, associated to the potential energy of the dipole in the electric field, and the radiation pressure from the recoil induced by absorbing and rescattering incident light. These stem from the real and the imaginary part of the polarizability, respectively.

From the electric-dipole interaction, Eq. (2.16), we can write the potential energy [36]

$$V_{\text{dip}} = -\frac{1}{2\epsilon_0 c}\text{Re}\{\alpha(\omega)\}\, I(\mathbf{r})\,, \tag{2.57}$$

where $I(\mathbf{r})$ is the intensity of the electric field. If the driving field is red-detuned, $\omega < \omega_0$, $V_{\text{dip}} < 0$ and the potential attracts the atoms to high-intensity regions. Conversely, if the field is blue-detuned, $\omega > \omega_0$, $V_{\text{dip}} > 0$ and the potential pushes the atoms to low-intensity regions.

Recoil, on the other hand, is mostly detrimental for experiments as it heats the atoms. Therefore, an important energy scale to characterize experiments is the recoil energy, $E_{\text{r}} = h^2/(2m\lambda^2)$, where m is the mass of the atom.

Subwavelength atom arrays have been realized using optical lattices [37, 38]. In an optical lattice, three pairs of counterpropagating laser beams generate a three-dimensional, periodic trapping potential of the form

$$V_{\text{dip}}(\mathbf{r}) = V_0\left[\sin^2\left(\frac{\pi r_x}{a}\right) + \sin^2\left(\frac{\pi r_y}{a}\right) + \sin^2\left(\frac{\pi r_z}{a}\right)\right]\,, \tag{2.58}$$

where $a = \lambda/2$ is the lattice constant. Here we assumed, for simplicity, that the trapping potential is isotropic with trap depth V_0. Subwavelength lattice spacings can be achieved with the right selection of a trapping transition, which sets the lattice spacing a, and the probed dipole transition that sets λ_0. These transitions do not need to be the same.

For our discussion on the effects of motion and disorder, we are interested in the motional degree of freedom of the trapped atoms. Assuming deep traps, such that

tunneling is weak, the trapping potential around the minima can be approximated by an harmonic oscillator with trap frequency [36]

$$\nu_{\mathrm{T}} = \frac{2E_{\mathrm{r}}}{h}\sqrt{\frac{V_0}{E_{\mathrm{r}}}}\,. \tag{2.59}$$

In the deep-traps scenario, the Wannier wave functions of the trapped atoms are approximately Gaussian, characterized by the oscillator length

$$l = \frac{a}{\sqrt{2}\pi}\sqrt[4]{\frac{E_{\mathrm{r}}}{V_0}}\,, \tag{2.60}$$

The oscillator length indicates the minimum spread of the atom wavefunction assuming that the atoms remain in their vibrational ground state.

2.6.2 Controlling the atoms with a Raman transition

Working with different atomic species on an experiment consisting of atoms trapped in an optical lattice is possible, but it increases the complexity of the setup. Assuming all atoms to be of the same species, however, limits the versatility of the system. In particular, as we can see in Fig. 2.3, the atom array band-width and free-space decay rate of the radiant eigenstates are of the order of the single-atom free-space decay rate γ_0. This is expected as the atom–atom interactions are radiation-based unless the atom separations are deeply subradiant, in which case short-range interactions become much stronger. However, this regime is difficult to achieve in practice. The fact that the linewidth of the additional target emitters is comparable to the features of the arrays will be detrimental for applications, as we discuss in the next chapters. For this, target atoms with a narrower free-space decay rate are desirable.

One possible approach to modify the linewidth of an atom is to use a multilevel system [39–41]. In particular, by using a three-level Λ-system such as the one depicted in Fig. 3.3.1. There, the transition $|e\rangle - |g_2\rangle$ is the same dipole transition considered so far, and a second metastable state $|g_1\rangle$ is coupled to the excited state through a Raman laser with Rabi frequency Ω. By using a laser with a large detuning Δ with the driven transition, the excited state remains weakly populated and can be eliminated using the methods described in Section 2.5. The result is a new effective two-level system with reduced radiative coupling and, therefore, a reduced linewidth. We defer a more formal treatment to the specific use-cases in the following chapters. We highlight that the Purcell factor and cooperativity, introduced above as good figures of merit for waveguide and cavity QED, will remain unaltered.

Using a Raman scheme has the additional advantage that the interaction can be

turned on and off through a time-dependent Rabi frequency, adding control to the system. Moreover, the excitation oscillates between two metastable states, which are long-lived.

APPENDIX

2.A REGULARIZING THE SELF-INTERACTION

To regularize Eq. (2.48) for the case of $\alpha = \beta$, we follow the approach described in [42] and subtract the divergent self-interaction term,

$$\Delta_{\alpha\alpha}(\mathbf{k}) - \frac{i}{2}\Gamma_{\alpha\alpha}(\mathbf{k}) = -\frac{3\pi\gamma_0}{k_0}\,\hat{\mathbf{e}}^* \cdot \left[\frac{1}{a^2}\sum_{\mathbf{B}} \mathrm{Re}\{\mathbf{G}(\mathbf{k}+\mathbf{B})\} - \mathrm{Re}\{\mathbf{G}(\mathbf{r}=0)\}\right] \cdot \hat{\mathbf{e}}\,. \quad (2.61)$$

To compute $\mathrm{Re}\{\mathbf{G}(\mathbf{r}=0)\}$, we introduce a Gaussian regulator $e^{-\mathbf{k}^2/\Lambda^2}$ to the Green's function, where Λ is a momentum cutoff. The elimination of high momenta contributions modifies the expression on short length scales, such that $\Delta_{\alpha\alpha}(\mathbf{r}=0)$ becomes finite.

We compute $\mathbf{G}(\mathbf{r}=0)$ using Eq. (2.47) with the Gaussian regulator,

$$\mathbf{G}(\mathbf{r}=0) = \frac{1}{(2\pi)^2}\int \mathrm{d}^2\mathbf{k}\, e^{-\mathbf{k}^2/\Lambda^2}\mathbf{G}(\mathbf{k};0)\,. \quad (2.62)$$

We will use the same Gaussian filter with every instance of the Green's function. Thus, numerical truncation of the sums over reciprocal lattice vectors $\mathbf{B}$ remains consistent and smooth

Solving for the real part of the above equation in cylindrical coordinates, we obtain

$$\mathrm{Re}\{\mathbf{G}(\mathbf{r}=0)\} = \frac{3\sqrt{\pi}\gamma_0}{32\,k_0^3}\,\Lambda\, e^{-k_0^2/\Lambda^2}\begin{pmatrix} \Lambda^2-2k_0^2 & 0 & 0 \\ 0 & \Lambda^2-2k_0^2 & 0 \\ 0 & 0 & -2\Lambda^2-4k_0^2 \end{pmatrix} \quad (2.63)$$

We verify numerically a fast convergence by choosing a large enough value of Λ.

3 Waveguide QED using one-dimensional atom arrays

The content of this chapter is based on

[1] D. Castells-Graells, D. Malz, C. C. Rusconi, and J. I. Cirac,
Atomic waveguide QED with atomic dimers
Physical Review A 104, 063707 (2021).

3.1 Motivation

Quantum emitters coupled to a waveguide is a paradigm of quantum optics, whose essential properties are described by waveguide quantum electrodynamics (QED). The field of waveguide QED has recently attracted renewed interest [15] due to experimental progress in novel experimental platforms such as superconducting waveguide quantum electrodynamics (QED) [43–46], cold atoms near nanofibres [47, 48] or photonic crystal waveguides [49–51], and quantum dots [52–54]. The dynamics of emitters coupled to such non-conventional reservoirs is expected to exhibit several distinctive features such as collective super and subradiant emission into the reservoir [50, 55], long-range dipole–dipole interactions mediated by the reservoir [40, 41, 56, 57], and non-Markovian effects [58–60]. The observation of many of these phenomena is, however, challenging even with the unprecedented level of control achieved today in several experiments. These difficulties arise from both imperfections in the fabrication of these devices as well as from the unavoidable absorption of photons in the waveguide (see [15] and references therein).

As discussed in Chapter 2, subwavelength arrays exhibit strong collective behavior that give rise to subradiant excitations, among other features. These collective subradiant excitations can in fact be thought of as propagating modes of a waveg-

uide [28, 61, 62], for which one can draw an analogy between a one-dimensional atom array and a conventional waveguide. Besides, the dispersion relation of the atom array is non-linear, with a structure akin to photonic crystal waveguides [33], which have a rich phenomenology. Thus, inspired by waveguide QED, we consider the case in which atoms are coupled to a guided mode of a one-dimensional subwavelength atom array. The motivation is that an atomic waveguide in free space is a conceptually simple, clean optical medium that allows, in principle, to eliminate any intrinsic internal losses or imperfections which affect conventional waveguides or photonic crystals, and may feature very low disorder.

The observation of characteristic waveguide QED phenomena in an atomic waveguide setup poses, however, several fundamental challenges. On the one hand, efficient coupling between external "target" atoms and the atomic waveguide is hindered by free space decay due to the presence of broad superradiant modes of the array. On the other hand, the dynamics of the emitters shows signs of non-Markovian effects, which ultimately spoil some of the interesting phenomena of conventional waveguide QED. Some of these difficulties may be overcome by reducing the interatomic separation of the waveguide and by placing the target atoms extremely close to the array [63, 64], but it is challenging to achieve the required deep subwavelength regime experimentally.

3.2 Summary

Here, we discuss an alternative approach to the atomic waveguide setup to mitigate the aforementioned problems. Specifically, we propose to use atomic dimers – a pair of closely spaced atoms – as effective two-level emitters coupled to the atomic waveguide, and to control the dimers' linewidth with a Raman transition. We show that a dimer behaves as an effective two-level system formed by its ground state and its anti-symmetric state. The anti-symmetric state features a reduced coupling to free-space modes and, at the same time, an increased coupling to the array's guided modes. Additionally, we show that by controlling the decay rate of the dimer atoms via a Raman transition, it is possible to recover a Markovian regime for the dynamics of dimers coupled to an atomic waveguide. We derive simple models for our setup that predict collective emission from the target dimers into an array's subradiant mode and coherent long-range interactions between target dimers mediated by the array. We verify both observations numerically for an atom array with interatomic separation of quarter-wavelength, a regime where the simpler case of single atoms coupled to an atomic waveguide is hampered by free-space decay and non-Markovian effects [63]. We also study the effects and different non-Markovian behaviors arising

from the finiteness of the array and the reduced group velocity at the band edge. Our results show a clear advantage of using dimers over atoms. Besides, we highlight a promising route toward observing non-Markovian waveguide QED physics, which has received considerable attention [60, 65–67].

We organize the chapter as follows. In Section 3.3, we discuss the setup considered and the specifics of its effective description with the spin model explained in Section 2.2.2. In Section 3.4, we give a thorough description of the proposed methods to access the guided modes of the array. Namely, the coupling between a dimer and the array modes, and the Raman transition used to control the dimer's linewidth. The resulting physics of dimers coupled to an atomic array are described in Section 3.5 (Section 3.6) for the case of dimer's frequency lying inside (outside) the band of guided modes of the array. We discuss the feasibility of our proposal and possible physical implementations in Section 3.7. We finally discuss possible generalizations of the case presented here and draw our conclusions in Section 3.8.

3.3 Setup and System Description

In this chapter, we consider a one-dimensional atomic array of N identical atoms with resonance frequency ω_0 and lattice spacing d, and n target atoms with resonance frequency ω_a placed at a distance h from the array, as depicted in Fig. 3.3.1. We assume all atoms to be polarized along the z-axis, which coincides with the direction of the atomic array, and to have the same free-space decay rate γ_0. An important length scale of the system is the wavelength $\lambda_0 = 2\pi c/\omega_0$. We will neglect the difference between λ_0 and $\lambda_\mathrm{a} = 2\pi c/\omega_\mathrm{a}$ throughout, which is valid because $|\omega_0 - \omega_\mathrm{a}| \ll \omega_0$.

The effective Hamiltonian Eq. (2.38) for this setup reads

$$\hat{H} = \sum_{i,j} \left(\omega_i \, \delta_{ij} + \Delta_{ij} - \frac{i}{2}\Gamma_{ij} \right) \hat{\sigma}_i^+ \hat{\sigma}_j^- \, . \tag{3.1}$$

As discussed in Section 2.2.2, in the absence of driving and within the single-excitation sector, the above Hamiltonian completely characterizes the dynamics of the system.

We can separate Eq. (3.1) into three terms that include the array, the target atom, and atom–array interaction parts of the Hamiltonian,

$$\hat{H} = \hat{H}_\mathrm{array} + \hat{H}_\mathrm{a} + \hat{H}_\mathrm{int}. \tag{3.2}$$

In the limit of an infinite array, we diagonalize the array Hamiltonian analytically in terms of Bloch eigenmodes $\hat{b}_k^\dagger = \frac{1}{\sqrt{N}} \sum_i e^{ikz_i} \hat{\sigma}_i^+$,

$$\hat{H}_\mathrm{array} = \sum_k \left(J_k - \frac{i}{2}\Gamma_k \right) \hat{b}_k^\dagger \hat{b}_k. \tag{3.3}$$

In the single excitation regime, $\hat{b}_k$ can be taken to be bosonic annihilation operators. Closed expressions for the eigenstate energy J_k and decay rate Γ_k are derived in Ref. [28].

In the following, we are interested in the experimentally relevant case of an array with open boundary conditions. In this case, an analytical exact expression for the single excitation eigenmodes of $\hat{H}_\mathrm{array}$ is not available. However, when the atomic array is sufficiently long, $N \gg 1$, the eigenmodes of $\hat{H}_\mathrm{array}$ can still be understood as spin waves with a well-defined quasi-momentum k, where the value of k corresponds to the point in reciprocal space where the eigenmode wavefunction is peaked [28, 68, 69]. In this limit, an accurate Ansatz for the single excitation eigenmodes is

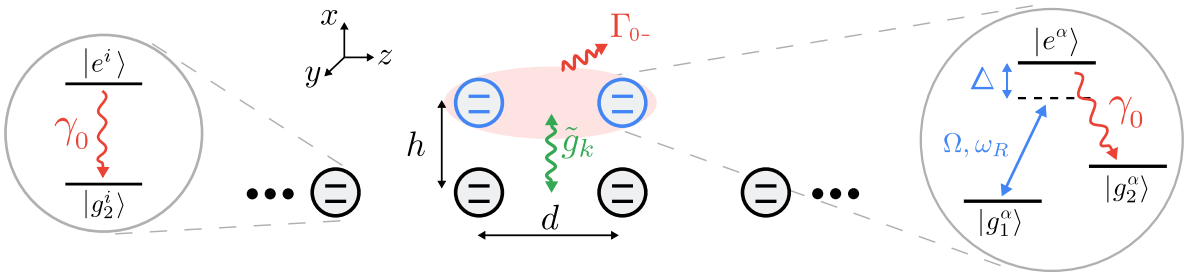

Figure 3.3.1: Schematic representation of the setup studied in this chapter. The target atoms (blue) interact with collective states of the atomic array (black). On the sides, we show the level scheme of the respective atoms. The effective two-level target atom discussed in Section 3.4 is realized with a three-level Λ system, in which the transition $|g_1\rangle \rightarrow |e\rangle$ is driven by a laser field with detuning Δ. The detuning and spontaneous emission rate are much larger than any other energy in the system and, thus, $|e^\alpha\rangle$ can be eliminated resulting in an effective two-level atom $|g_1^\alpha\rangle$–$|g_2^\alpha\rangle$.

$\hat{b}_k^\dagger = \sum_i \xi_{k_\nu}(z_i)\,\hat{\sigma}_i^+$, with [28]

$$\xi_{k_\nu}(z_i) = \begin{cases} \sqrt{\frac{2}{N+1}}\,\cos(k_\nu z_i) & \text{if } \nu \text{ is odd} \\ \sqrt{\frac{2}{N+1}}\,\sin(k_\nu z_i) & \text{if } \nu \text{ is even} \end{cases}, \tag{3.4}$$

where $k_\nu = \pi\nu/d(N+1)$ with $\nu = 1, 2, \ldots, N$. Accordingly, J_k and Γ_k in Eq. (3.3) do not have analytical expressions, but are well approximated by the expressions for an infinite array whenever $N \gg 1$.

Unless otherwise specified, we will always refer to the case of finite arrays with open boundary conditions, as this is the most relevant case for the experimental realization of atomic waveguide QED. Single-excitation eigenstates of $\hat{H}_{\text{array}}$ with a quasi-momentum $k > k_0$ lying outside the light cone of free space electromagnetic modes exist for $d < \lambda_0/2$. As discussed in Section 2.3, these collective states are subradiant and have been shown to decay at a rate $\sim \gamma_0/N^3$ due to scattering of the field through the ends of the array [28, 70]. These states can be intuitively understood as excitations propagating along the array.

The second term in Eq. (3.2), which includes the target atoms and interactions among them, reads

$$\hat{H}_{\text{a}} = \sum_i \omega_{\text{a}} \hat{c}_i^\dagger \hat{c}_i + \sum_{i,j} \left(g_{ij} - \frac{i}{2}\gamma_{ij} \right) \hat{c}_i^\dagger \hat{c}_j. \tag{3.5}$$

Here, we defined $\left(g_{ij} - i\gamma_{ij}/2\right)$ instead of $\left(\Delta_{ij} - i\Gamma_{ij}/2\right)$ to differentiate interactions between target atoms from interactions among the array atoms. We also replaced the Pauli matrix of the target atoms with bosonic operators, $\hat{\sigma}_i^- \rightarrow \hat{c}_i$, as we restrict our analysis to single-excitation dynamics [68]. We recall that, when $i = j$,

$(g_{ii} - i\gamma_{ii}/2) = -i\gamma_0/2$, where we include the energy shift in the resonance energy of the atoms.

The last term in Eq. (3.2) contains the interactions between array atoms and target atoms. Using the definitions above, the interaction Hamiltonian between the target atoms and the eigenmodes of the array reads

$$\hat{H}_{\text{int}} = \sum_{k,i} \tilde{g}_k^i \left(\hat{c}_i^\dagger \hat{b}_k + \text{h.c.} \right), \tag{3.6}$$

where we defined the complex coupling of a single target atom at position $\mathbf{r}_i$ to an array mode with quasi-momentum k, $\tilde{g}_k^i$, with

$$\tilde{g}_k^i = \left(g_k^i - \frac{i}{2}\gamma_k^i \right) = \xi_k(z_i) \left(|g_k^i| - \frac{i}{2}|\gamma_k^i| \right) \tag{3.7}$$

with $\xi_k(z_i)$ as defined in Eq. (3.4), and

$$|g_k^i| - \frac{i}{2}|\gamma_k^i| = -\frac{3\gamma_0\, i}{8d} \sum_{m\in\mathbb{Z}} \left[1 - \kappa_m(k)^2\right] H_0^{(1)}\left(k_0 h \sqrt{1-\kappa_m(k)^2}\right). \tag{3.8}$$

We derive the above expression in the Appendix 3.A. Here, $\kappa_m(k) = (k/k_0 + m\lambda_0/d)$, and $H_0^{(1)}$ is the Hankel function of the first kind and zeroth order. Note that for $k > k_0$, Eq. (3.8) is purely real, which means that the coupling of a target atom to the subradiant Bloch modes is coherent and dissipation-free. The coupling Eq. (3.8) between a single target atom and a mode k in the array is plotted in Fig. 3.4.2. For the case of an infinite array, the coupling can be obtained from Eq. (3.8) by substituting $\xi_k(z_i) \to e^{-ikz_i}/\sqrt{N}$.

3.4 Accessing the guided modes of the array

Since achieving small d is increasingly challenging experimentally, we consider here the case of $d = \lambda_0/4$. For this parameter choice, the free-space decay of the most superradiant state, $\Gamma_{k=0}$, is comparable to the width of the band J_k in Eq. (3.3). The dynamics of an emitter with energy lying within the band of the array is thus dominated by the dissipative resonant interaction with the array's superradiant modes. We show an example of this in Fig. 3.4.1(left), where a target atom initialized on its excited state looses the excitation exponentially at a faster rate than its natural free-space decay rate (dashed line). Most of the excitation is lost to free space and only a small fraction is transferred to the subradiant modes of the array, which hold the excitation for a long time.

In this section, we discuss our proposed approach to access the guided modes of

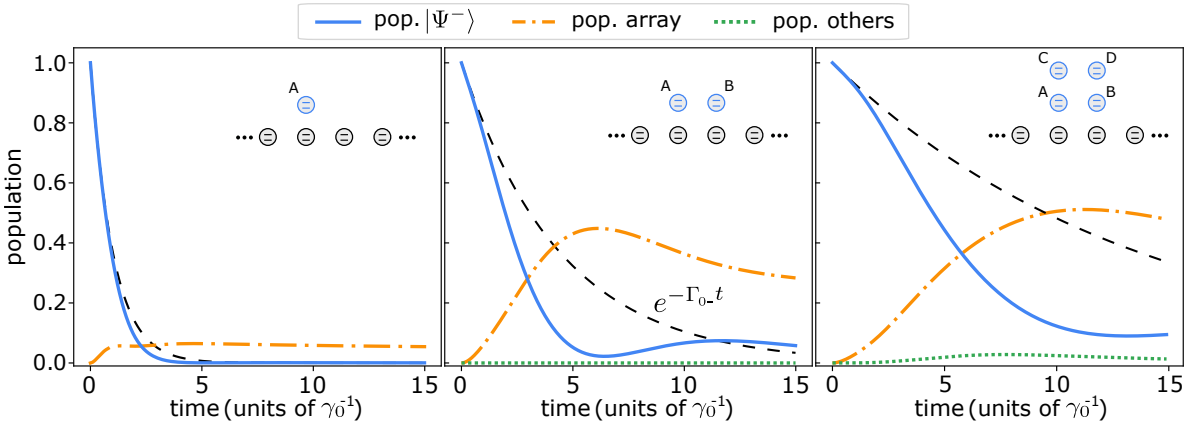

Figure 3.4.1: Dynamics of a target atom prepared in the state $|\Psi^-\rangle$ resonant with the array subradiant modes for the case of a single atom (left), a dimer (middle), and a 2×2 plaquette (right). The dashed line corresponds to the free-space decay of $|\Psi^-\rangle$ at a rate Γ_{0-}. The colored lines correspond to different states according to the legend, where *array* refers to the sum over all array modes, and *others* refers to all the eigenstates of the target atom other than $|\Psi^-\rangle$. We define $|\Psi^-\rangle = |e\rangle$ for the single atom, $|\Psi^-\rangle = (|eg\rangle - |ge\rangle)/\sqrt{2}$ for the dimer, and $|\Psi^-\rangle = \frac{1}{2}(|eggg\rangle - |gegg\rangle - |ggeg\rangle + |ggge\rangle)$ for the plaquette, where the general state of the plaquette is given by $|\nu_A\nu_B\nu_C\nu_D\rangle$, with $\nu = g, e$. We tune the atomic transition of the single target atoms for each case such that the collective state $|\Psi^-\rangle$ has always the same energy. Here, we use $N = 50$, $d = \lambda_0/4$, and the energy of the state $|\Psi^-\rangle$ is set resonant with the array mode with $k = 0.95\pi/d$.

the array, while obviating the resonant highly dissipative modes and staying in the Markovian regime. The approach consists of using pairs of atoms for the role of the target atom, and narrowing the target atom's linewidth with a Raman transition, respectively. In Section 3.4.1, we derive the coupling of the collective excitation of two neighboring atoms, which we name "atomic dimer", with the eigenstates of the array. We then show that the anti-symmetric dimer eigenstate does not interact with the undesirable superradiant array modes, while it interacts efficiently with the subradiant modes.

In Section 3.4.2, we show that we can adiabatically eliminate the symmetric dimer eigenstate and the superradiant modes of the array, such that we can effectively treat the system as independent effective target atoms (consisting of the anti-symmetric dimer eigenstates) interacting with the guided (subradiant) modes of the array.

In Section 3.4.3, we describe the Raman scheme used to reduce the linewidth of the target atoms, such that they show a Markovian evolution when interacting with the array. We also obtain the new Hamiltonian that includes the Raman scheme that we use for all the numerical results shown in the following sections, and the effective dimer–waveguide Hamiltonian that we use for our analytical predictions.

3.4.1 Atomic dimers

We consider a dimer formed by two neighboring target atoms at positions $\mathbf{r}_i = (h, 0, z_i)^T$ and $\mathbf{r}_{i+1} = (h, 0, z_{i+1})^T$. We label the two atoms forming a dimer "a" and "b" with positions $\mathbf{r}_i^a = \mathbf{r}_i$ and $\mathbf{r}_i^b = \mathbf{r}_{i+1}$, respectively. We represent the collective single excitation of an atomic dimer with the bosonic operator

$$\hat{a}_{i\lambda} = \frac{1}{\sqrt{2}} \left(\hat{c}_i^a + \lambda \, \hat{c}_i^b \right) , \tag{3.9}$$

where $\hat{c}_i^a = \hat{c}_i$ and $\hat{c}_i^b = \hat{c}_{i+1}$. For $\lambda = -1$ ($\lambda = 1$), Eq. (3.9) creates an anti-symmetric (symmetric) excitation which predominantly couples to the sub(super)-radiant array modes exploiting their short(long)-wavelength nature. The coupling to the array modes of the states of a dimer centered at $\rho_i = \hat{z} \cdot (\mathbf{r}_i^a + \mathbf{r}_i^b)/2$, with atoms aligned to the array atoms as depicted in Fig. 3.3.1, writes (see Appendix 3.A)

$$\begin{aligned} |g_k^{i\lambda}| - \frac{i}{2}|\gamma_k^{i\lambda}| = -\frac{3\gamma_0 \, i}{4\sqrt{2}\, d} \left\{ \begin{array}{ll} \sin\left(\frac{kd}{2}\right) & \text{if } \lambda = -1 \\ \cos\left(\frac{kd}{2}\right) & \text{if } \lambda = 1 \end{array} \right\} \\ \times \sum_{m \in \mathbb{Z}} \left[1 - \kappa_m(k)^2 \right] H_0^{(1)} \left(k_0 h \sqrt{1 - \kappa_m(k)^2} \right) , \end{aligned} \tag{3.10}$$

and $\left(g_k^{i\lambda} - \frac{i}{2}\gamma_k^{i\lambda}\right) = \xi_k^\lambda(\rho_i) \left(|g_k^{i\lambda}| - \frac{i}{2}|\gamma_k^{i\lambda}|\right)$. This expression is similar to Eq. (3.8) with an additional factor of $\sqrt{2}$ and a quarter-sine-wave envelope. In the case of the dimer, the coupling to half of the modes becomes zero at the center of the array due to the particular symmetry of the collective dimer states, as indicated in Eq. (3.42) and Eq. (3.43). Unless otherwise specified, we set $h = d$ from here forth.

As we can see in Fig. 3.4.2, the anti-symmetric configuration ($\lambda = -1$) eliminates the undesired dissipative coupling at small k due to a destructive interference of the interaction of each atom with the array eigenstates. Additionally, it increases the coupling to the subradiant modes thanks to constructive interference. In Fig. 3.4.1(middle), we show the dynamics for a dimer anti-symmetric state near an atomic waveguide, where we can appreciate the more efficient interaction with the long-lived subradiant modes of the array, as compared to using a single target atom.

The dimer states in Eq. (3.9) are the eigenstates of Eq. (3.1) with two atoms. Their eigenvalues are $E_\lambda - \frac{i}{2}\Gamma_{0\lambda} = (\omega_0^{\text{imp}} + \lambda g_{ab}) - \frac{i}{2}(\gamma_0 + \lambda\gamma_{ab})$, with

$$\begin{aligned} g_{ab} &= -\frac{3\gamma_0}{2k_0^3 r_{ab}^3} \left[\cos(k_0 r_{ab}) + k_0 r_{ab} \sin(k_0 r_{ab}) \right] \\ \gamma_{ab} &= -\frac{3\gamma_0}{k_0^3 r_{ab}^3} \left[k_0 r_{ab} \cos(k_0 r_{ab}) - \sin(k_0 r_{ab}) \right] , \end{aligned} \tag{3.11}$$

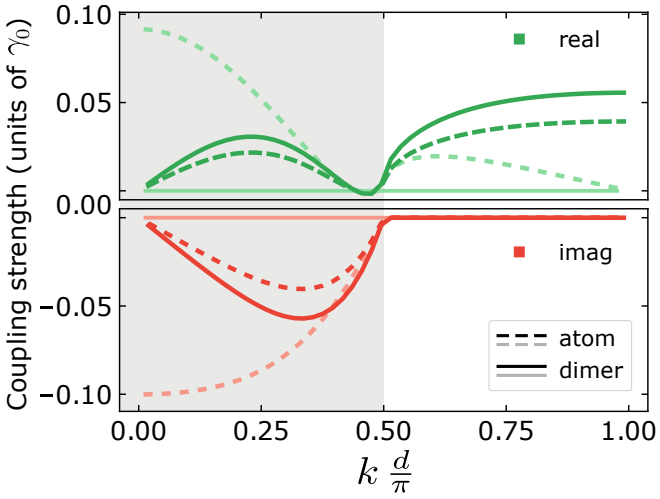

Figure 3.4.2: Real (top) and imaginary (bottom) part of the coupling of a single target atom (dashed) or a dimer in the anti-symmetric $\lambda = -1$ state (solid) with an array mode with quasi-momentum k. The shaded region indicates the superradiant part of the array modes. The dimer is aligned with the center and the single atom with the closest site to the center of an array with $N = 100$ and $d = h = \lambda_0/4$. The dimer anti-symmetric state interacts destructively (constructively) with the low(high)-k modes. Hence, in comparison with a single atom, the coupling of the dimer to the guided modes is stronger, while the coupling to the superradiant modes is highly suppressed. The dark and light lines correspond to the two different parities of the standing waves in a finite array [see Eq. (3.4) for one atom or Eq. (3.42) for a dimer]. The light line is exactly zero in this case due to placing the dimer exactly in the centre of the array ($z = 0$).

for a separation r_{ab} between the two atoms. For $r_{ab} < \lambda_0/2$, as is the case for sub-wavelength arrays in one dimension, the anti-symmetric dimer state has a reduced linewidth as compared to the single atom. In particular, for $d = \lambda_0/4$, the decay rate $\Gamma_{0-} \simeq \gamma_0/4$. This reduction of the linewidth is an additional benefit to using dimers instead of single atoms. This naturally leads us to consider modifications to the dimer solution with even smaller decay rates, such as using larger ensembles or decreasing the separation between the dimer atoms. Next, we show that the benefit of these alternative setups is relatively small. Favoring the simplicity of an atomic dimer with the same lattice spacing than the array, we will consider dimers for the rest of the chapter.

Alternative setup: a 2x2 quadruplet

In Fig. 3.4.1(right), we show the time dynamics of a 2×2 plaquette initialized in an anti-symmetric configuration in both x and z directions. As expected, using a larger ensemble allows to attain a smaller free-space decay as compared to the dimer. However, the reduction of free-space decay is hindered by the smaller coupling with the array modes, for which a longer time is required to achieve the same amount

of transfer of population to the array. In fact, if we scaled the time-axis of the two plots by the decay rate of the respective anti-symmetric state, we would observe little qualitative difference between the evolution of the two systems. This observation extends to other configurations with more than two atoms.

Alternative setup: smaller dimer atom separation

For $r_{ab} < d$, we can repeat the derivation in Appendix 3.A to obtain

$$|g_k^{i-}| - \frac{i}{2}|\gamma_k^{i-}| = -\frac{3\gamma_0\, i}{4d\sqrt{2N}} \sum_{m\in\mathbb{Z}} \sin\left[\frac{kr_{ab}}{2} + \left(\frac{r_{ab}}{d} - 1\right)\pi n\right] \times \left[1 - \kappa_m(k)^2\right] H_0^{(1)}\left(k_0 h\sqrt{1-\kappa_m(k)^2}\right), \tag{3.12}$$

and $\left(g_k^{i-} - \frac{i}{2}\gamma_k^{i-}\right) = \xi_k^-(\rho_i)\left(|g_k^{i-}| - \frac{i}{2}|\gamma_k^{i-}|\right)$ for the coupling rate of the anti-symmetric eigenstate of the dimer. For the symmetric eigenstate, we need to replace the sine with a cosine. From Eq. (3.11), we know that γ_{ab} can be reduced by reducing r_{ab}. The coupling Eq. (3.12), however, also becomes smaller for $r_{ab} < d$. A plot of the ratio $|g_k^{i-}|^2/\Gamma_{0-}$ — a magnitude we want to maximize, as we discuss in Section 3.5 and 3.6 — as a function of r_{ab} shows a slow monotonic increase towards smaller r_{ab}. The value of $|g_k^{i-}|^2/\Gamma_{0-}$ for the extreme case of $r_{ab} \to 0$ is only about a factor of two larger than for $r_{ab} = d$.

3.4.2 Effective Hamiltonian for the dimer-array interaction

When the resonance energy of the anti-symmetric state of the dimer is resonant with the subradiant part of the band, or it lies outside of the band, it is possible to adiabatically eliminate both the array's superradiant sector and the symmetric state of the dimer. Thus, the dynamics of a system initialized on either the anti-symmetric dimer state or a subradiant array eigenstate can be modeled as an effective two-level system — formed by the dimer's ground and anti-symmetric states — coupled coherently to a set of subradiant modes. For the rest of this chapter, we often refer to the resulting effective two-level target atom simply as "dimer".

To derive the effective Hamiltonian for the interaction between the anti-symmetric state of a dimer and the subradiant modes of the array, we define the state $|\psi(t)\rangle = \sum_\lambda a_\lambda(t)\,\hat{a}_\lambda^\dagger\,|0\rangle + \sum_k b_k(t)\,\hat{b}_k^\dagger\,|0\rangle$, and obtain the equations of motion of the corre-

sponding dimer and array coefficients evolving under the Hamiltonian Eq. (3.2),

$$\dot{a}_\lambda(t) = -i\left(E_\lambda - \frac{i}{2}\Gamma_{0\lambda}\right) a_\lambda(t) - i\sum_k \tilde{g}_k^\lambda\, b_k(t) \tag{3.13}$$

$$\dot{b}_k(t) = -i\left(J_k - \frac{i}{2}\Gamma_k\right) b_k(t) - i\sum_\lambda \tilde{g}_k^\lambda\, a_\lambda(t)\,. \tag{3.14}$$

We stay within the single excitation subspace and consider a single dimer for simplicity. The extension to multiple dimers is straightforward, especially when the free-space coupling between them is negligible, as is usually the case for distances between dimers larger than λ_0.

In Fig. 3.4.2, we see that interference suppresses the coupling between the anti-symmetric state of the dimer and the most dissipative modes of the array. The same applies between the symmetric dimer state and the subradiant modes. Setting the dimer anti-symmetric state energy, E_-, resonant with the subradiant array modes, $J_{k>k_0}$, the symmetric state energy, E_+, is resonant with the superradiant modes, $J_{k<k_0}$. In such case, $\sqrt{N}\tilde{g}^+_{k>k_0} \ll |J_{k>k_0} - E_+|$ and $\sqrt{N}\tilde{g}^-_{k<k_0} \ll |J_{k<k_0} - E_-|$. We set the zero of energy at E_- and define $\Delta_+ = (E_+ - E_-)$ and $\Delta_k = (J_k - E_-)$. Under these conditions, and assuming that the system is initialized in the dimer anti-symmetric state, $a_-(0) = 1$, we can adiabatically eliminate the symmetric dimer state and the superradiant modes of the array. To perform the elimination, we set $\dot{a}_+(t) = \dot{b}_{k<k_0}(t) = 0$, and isolate $a_+(t)$ and $b_{k<k_0}(t)$ from their respective equations of motion in Eq. (3.13) and Eq. (3.14), as discussed in Section 2.5. We then substitute the resulting expressions into the equations for $\dot{a}_-(t)$ and $\dot{b}_{k>k_0}(t)$ to obtain a new set of effective equations of motion that include only the anti-symmetric dimer state and the subradiant modes of the array. After doing this treatment, the new effective resonance energies, decay rates and coupling rates are

$$E_-^{\text{eff}} \simeq\; E_- - A^-\left(1 + \frac{B^*}{\Delta_+ - A^+ - \frac{i}{2}\Gamma_{0+}}\right) \tag{3.15}$$

$$J^{\text{eff}}_{k>k_0} \simeq\; J_{k>k_0} - \frac{\tilde{g}^{+*}_{k>k_0}}{\Delta_+ - A^+ - \frac{i}{2}\Gamma_{0+}} \sum_{k'>k_0} \tilde{g}^+_{k'} \tag{3.16}$$

$$\tilde{g}^{-\,\text{eff}}_{k>k_0} \simeq\; \tilde{g}^-_{k>k_0} + \frac{B}{\Delta_+ - A^+ - \frac{i}{2}\Gamma_{0+}}\, \tilde{g}^+_{k>k_0}\,, \tag{3.17}$$

with

$$A^\lambda = \sum_{k<k_0} \frac{\tilde{g}_k^\lambda\, \tilde{g}_k^{\lambda*}}{\Delta_k - \frac{i}{2}\Gamma_k}\,, \text{ and } B = \sum_{k<k_0} \frac{\tilde{g}_k^-\, \tilde{g}_k^{+*}}{\Delta_k - \frac{i}{2}\Gamma_k}\,, \tag{3.18}$$

where $\tilde{g}_k^{\lambda*} = \left(g_k^{\lambda*} - \frac{i}{2}\gamma_k^{\lambda*}\right) = \xi_k^{\lambda*}\left(|g_k^\lambda| - \frac{i}{2}|\gamma_k^\lambda|\right)$.

These corrections are negligible when the dimer resonance energy sits at the edge

of the array's band, as verified numerically by comparing the evolution under the full Hamiltonian and the effective Hamiltonian derived here. This is true because the coupling rate of the dimer anti-symmetric state with the most superradiant array modes, which lie around $k = 0$, is close to zero, and the overlap with the narrower radiant modes of larger k is small at those energies. Since the edge of the band is our region of interest, we can hence model the system with a two-level target atom consisting of the ground and anti-symmetric state of the dimer interacting coherently with the guided ($k > k_0$) modes of the array. For lower target atom energies closer to J_{k_0}, the dimer becomes resonant with those additional, less broad, superradiant modes with which the coupling is non-zero. In this case, Eq. (3.15) introduces finite corrections to the effective dynamics. This additional coupling to superradiant channels is further suppressed after we introduce a Raman transition on the dimer atoms, since the dimer states' linewidth is reduced and so is the overlap with those modes.

3.4.3 Raman Transition

Despite the reduced effective decay rate Γ_{0-} of the dimers, their linewidth is still comparable to the bandwidth (BW) of the array for $d = \lambda_0/4$, leading to strong non-Markovian effects, as can be seen in Fig.3.4.1(middle), where the dynamics show oscillations instead of a monotonic exponential decay of the excitation of the dimer into the array. To enter the Markovian regime, we can further reduce the dimer's linewidth using a Raman scheme as depicted in Fig. 3.3.1.

In the Raman scheme, the dimer atoms are initialized in additional metastable levels $|g_1^{a,b}\rangle$, and driven into the excited state of the dipole transition included in Eq. (3.1), $|e^i\rangle = \hat{\sigma}_i^+ |g_2^i\rangle$, by a laser with Rabi frequency Ω. The driving frequency, ω_R, is detuned with respect to the energy difference between the two states by Δ. The decay rate from $|e^\alpha\rangle$ to $|g_1^\alpha\rangle$ is assumed to be much slower than γ_0 and is thus neglected. The dimer atoms are excited without affecting the array atoms by placing the array on a node of the laser field. To describe the dynamics of the system including the Raman transition for the dimer atoms, we use the Hamiltonian in Eq. (3.2) and include the energy of the levels $|g_1^{a,b}\rangle$, and the interaction terms due to the driving laser, $\frac{\Omega}{2}\left(|g_1^\alpha\rangle\langle e^\alpha| e^{i\omega_R t} + \text{h.c.}\right)$. To remove the time dependence of the new interaction term, we move to a frame rotating with ω_R, yielding

$$\hat{H}_{\text{R}} = \hat{H} + \sum_\alpha (\omega_{\text{a}} - \Delta) |g_1^\alpha\rangle\langle g_1^\alpha| + \frac{\Omega}{2}\sum_\alpha \left(|g_1^\alpha\rangle\langle e^\alpha| + \text{h.c.}\right). \tag{3.19}$$

We use the evolution under the Hamiltonian in Eq. (3.19), with $\hat{H}$ as given by

Eq. (3.1), for all numerical results presented in this chapter, which we use to benchmark the predictions obtained with analytical derivations and additional approximations.

For $\Delta, \gamma_0 \gg \Omega, g_{ab}, \gamma_{ab}, g_k^i, \gamma_k^i$, the states $|e^{a,b}\rangle$ remain weakly populated at all times, which we eliminate to second order in perturbation theory in Appendix 3.B. The resulting dynamics can be approximated by an effective Hamiltonian that includes effective two-level target atoms $|g_1^\alpha\rangle$–$|g_2^\alpha\rangle$. For this, we define new operators for the dimer states, $\hat{a}'_{i\lambda} = (\hat{c}_i^{a\prime} + \lambda\, \hat{c}_i^{b\prime})/\sqrt{2}$, with $\hat{c}_i^{\alpha\prime}\, |g_1^{i\alpha}\rangle = |g_2^{i\alpha}\rangle$. We can further simplify the resulting Hamiltonian by eliminating the dimer symmetric state and the superradiant modes of the array, as in the previous section. Using $\Delta \gg \gamma_0$, the effective coupling between array and dimer is coherent.

Hence, as shown in Fig. 3.4.3, for $\Delta \gg \gamma_0 \gg \Omega, g_{ab}, \gamma_{ab}, g_k^i, \gamma_k^i$ and distant dimers, we observe the dynamics of Eq. (3.19) to be well approximated by the effective Hamiltonian

$$\begin{aligned}\hat{H}_{\text{eff}} = &\sum_i \left(\omega_{\text{a}}{}' - \frac{i}{2}\Gamma'_{0-}\right) \hat{a}_{i-}^{\prime\,\dagger} \hat{a}'_{i-} + \sum_{k>k_0} \left(J_k - \frac{i}{2}\Gamma_k\right) \hat{b}_k^\dagger \hat{b}_k \\ &+ \sum_{i,k>k_0} g'_k \left(\xi_k^-(\rho_i)\, \hat{a}_{i-}^{\prime\,\dagger} \hat{b}_k + \text{h.c.}\right) ,\end{aligned} \tag{3.20}$$

with $\omega_{\text{a}}{}' = \omega_{\text{a}} - \Delta - \Omega^2/4\Delta$, $\Gamma'_{0-} = \Gamma_{0-}\Omega^2/4\Delta^2$ and $g'_k = |g_k^-|\Omega/2\Delta$. Note that ${g'_k}^2/\Gamma'_{0-}$ is independent of Ω and Δ as long as $\Delta \gg \gamma_0 \gg \Omega, g_{ab}, \gamma_{ab}, g_k^i, \gamma_k^i$ is fulfilled. Obtaining smaller Γ'_{0-}, however, makes the Markovian regime accessible, since $\Gamma'_{0-}/\text{BW} \sim (\Omega/\Delta)^2$. On the other hand, g'_k can be modified with other system parameters, such as tuning the resonance energy of the emitter with respect to the band, as we discuss in Section 3.5. For simplicity, except when the finiteness of the array is explicitly relevant, we use the infinite array form of $\xi_k(\rho_i)$. We also define $\gamma'_0 = \gamma_0\Omega^2/4\Delta$, which we will use as new time scale for the dynamics.

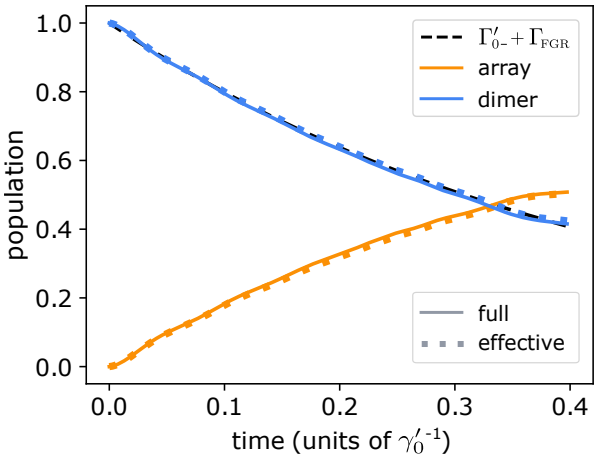

Figure 3.4.3: Population dynamics for a dimer anti-symmetric state resonant with $k = 0.945\pi/d$ for $N = 500$, $d = \lambda_0/4$, $\Delta = 8\gamma_0$, and $\Omega = 0.2\gamma_0$. The dimer line represents the anti-symmetric state of the dimer, and the array integrates the population of all array modes. The population of all other states is negligible. The loss of total population is due to the dimer's free-space decay. The solid lines are computed with the full-system Hamiltonian, Eq. (3.19), and the dotted lines with the effective Hamiltonian in Eq. (3.20). The black dashed line shows the prediction using Fermi Golden's Rule (FGR), which we discuss next in Section 3.5, and captures the dimer dynamics with great approximation.

3.5 In-band dynamics

In this section we study the dynamics of initializing one or multiple dimers with a resonance energy that lays within the band of guided modes of the array. In Section 3.5.1, we show that, at short times, we recover the Markovian dynamics expected in waveguide QED, for which the population of the emitters decays exponentially into the guided modes of the arrays, and which rate can be predicted using Fermi Golden's Rule. We also show that distant dimers interact through the guided modes of the array. In particular, we show collective decay due to constructive interference between multiple dimers.

In Section 3.5.2, we show that, at long times comparable to the length of the array divided by the group velocity of the guided modes, we observe non-Markovian effects in the dynamics. We understand these effects as the retarded back-action on the emitter via the electric field, which is reflected back at the ends of the array. The non-Markovian features can also be explained mathematically considering that the energy band of a finite array is discrete and not continuous, as assumed with conventional waveguides. By resolving the discreteness of the states with narrow enough dimer linewidths, we can access different non-Markovian behaviors, including enhanced and suppressed emission.

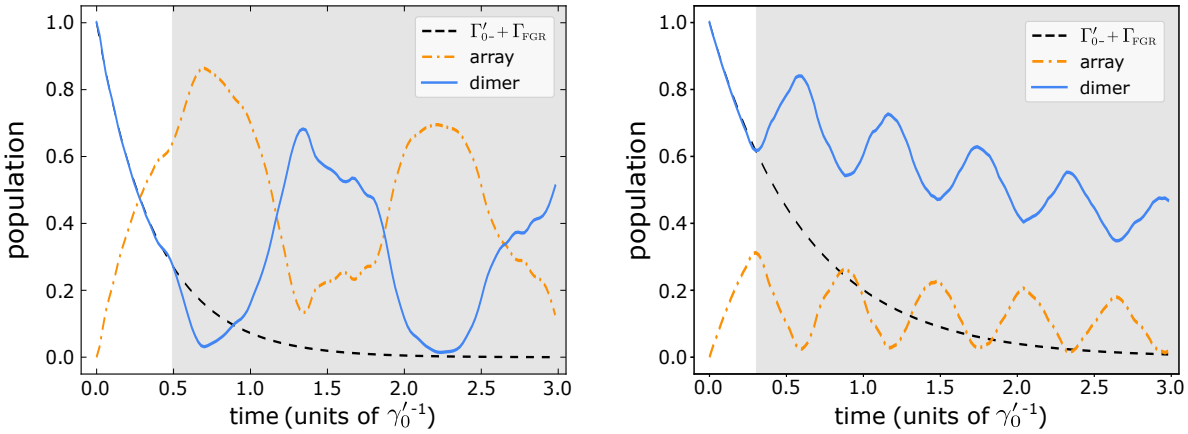

Figure 3.5.1: Population dynamics for a dimer anti-symmetric state resonant with (left) $k = 0.956\pi/d$ and (right) $k = 0.922\pi/d$. The dimer is aligned with the center of the array. The dimer line represents the anti-symmetric state of the dimer, and the array line integrates the population of all array modes. The loss of total population is due to the dimer's free-space decay. The unshaded region corresponds to the Markovian regime, in which the population is predicted by Fermi's golden rule (FGR). The shaded region corresponds to the non-Markovian regime. Parameters for all the plots are $N = 500$, $d = \lambda_0/4$, $\Delta = 8\Gamma_0$, and $\Omega = 0.2\Gamma_0$.

3.5.1 Markovian regime

When the resonance energy of a dimer lies within the sub-radiant region of the array's band, there is a coherent transfer of population between the dimer and the guided modes of the array. In the Markovian regime (see the white region in Fig. 3.5.1), the transfer of population can be modeled as a plane wave emitted into the resonant array mode k,

$$\hat{H}_{\text{in}} = -\frac{i}{2}\Gamma_{1D}\sum_{i,j} e^{ik(\rho_i-\rho_j)}\hat{a}'^{\dagger}_{i-}\hat{a}'_{j-} - \frac{i}{2}\Gamma'_{0-}\sum_i \hat{a}'^{\dagger}_{i-}\hat{a}'_{i-}, \tag{3.21}$$

where Γ_{1D} is the effective decay rate of the dimer excitation into the array. A large Purcell factor $P = \Gamma_{1D}/\Gamma'_{0-}$ corresponds to the desired regime of predominant decay of the emitters into the array modes. The decay rate Γ_{1D} obtained from numerical simulations agrees with the prediction using Fermi's golden rule (FGR),

$$\Gamma_{\text{FGR}} = 2Nd\,\frac{g'^{\,2}_k}{\partial_k J_k}\,. \tag{3.22}$$

In Fig. 3.5.2(left), we plot P as a function of k as extracted from the numerical evolution, and compare it to the prediction using FGR. We compare the case of a dimer and of a single atom, showing that the former allows for a substantial improvement in P with respect to the latter. The coupling g'_k increases with k, while $\partial_k J_k$ decreases and becomes zero at the band edge. Hence, larger k are favorable and would lead to a divergence in the Γ_{1D} according to Eq. (3.22). The Markovian assumption, how-

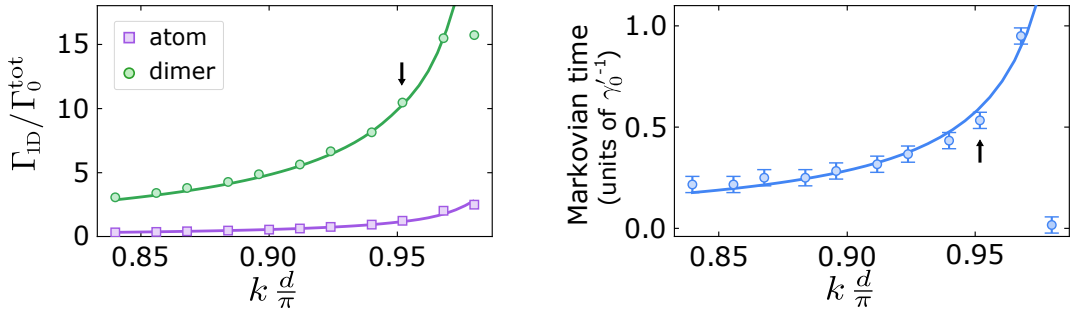

Figure 3.5.2: (left) Purcell enhancement extracted from the population dynamics. We obtain Γ_{1D} by fitting an exponential decay to the dimer's population, restricted to the Markovian regime. For Γ_0^{tot}, which includes all sources of decay, we fit the evolution of the total population in the single-excitation subspace. The solid lines show the prediction using FGR. (right) Time until the dynamics enter the shaded regions in Fig. 3.5.1, measured from the numerical evolution as the time at which the population at the dimer differs from the Markovian prediction by a 6%. The solid line shows the prediction using the length of the array and the group velocity at k to calculate the time at which the excitation in the corresponding guided mode reaches the dimer after being reflected at the ends of the array. (both) The black arrow indicates the quasi-momentum of the array mode with which the dimer in Fig. 3.5.1(left) is at resonance. The deviation of the points at higher k from the predictions is due to the non-Markovian dynamics close to the band edge. Here we use $N = 500$, $d = \lambda_0/4$, $\Delta = 8\gamma_0$, and $\Omega = 0.2\gamma_0$.

ever, breaks down at large Γ_{1D} before reaching such divergence, as observed from the deviation between the model and the numerical results in Fig. 3.5.2. The value of P at a certain k depends on the parameters d and h, but not on Ω or Δ. The value of k at which the Markovian approximation breaks down, however, depends on d, h, and also on Ω/Δ (smaller Ω/Δ reduces both the coupling strength and the linewidth of the dimer). Hence, by making Ω/Δ smaller, the evolution stays Markovian for larger k, allowing for larger Purcell factors. This improvement in the Purcell factor is, however, achieved at the cost of slower dynamics.

The presence of a 1D bath allows for different dimers along the array to have a finite probability to interact with the photon emitted by the originally excited dimer, despite the large separations that make free-space interactions negligible. Those interactions through the guided modes lead to a constructive interference if n dimers are prepared in a symmetric state $\hat{a}_-^{sym\,\dagger} = \frac{1}{\sqrt{n}}\sum_{i=1}^{n}\hat{a}_{i-}^{\prime\,\dagger}$ and placed in an atomic mirror configuration, $|\rho_i - \rho_j|k = 2\pi q$, with $q \in \mathbb{Z}$. In this state, the decay rate is enhanced by $\Gamma_{1D}^{sym} = n\Gamma_{1D}$, while emission into free space is unaltered. This type of superradiance is also observed in conventional waveguide QED [55]. In Fig. 3.5.3, we show this feature with three dimers. Specifically, we plot the band J_k and indicate which energies correspond to values of k that satisfy the atomic mirror condition. The shaded regions indicate the resonance energy of the dimers for which we observe a decay rate into the array which is a factor of three larger than the FGR

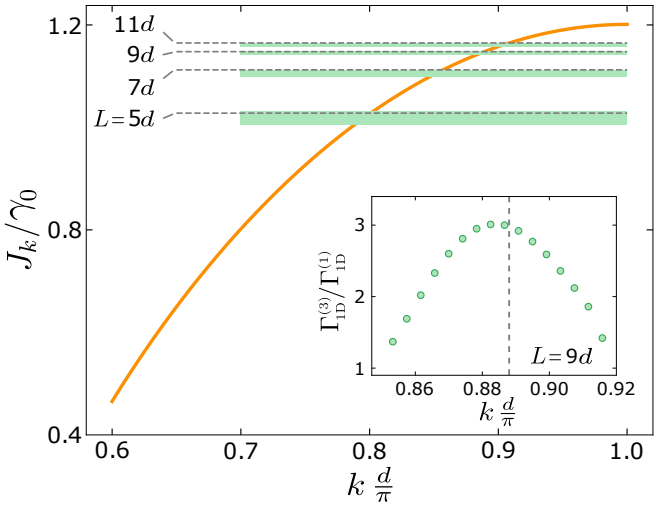

Figure 3.5.3: Dispersion relation of the array. The shaded regions indicate the energies for which the emission rate of a symmetric state of $n = 3$ dimers into the array shows $n\,\Gamma_{1D}$ superradiance for dimer–dimer separations of $L = 5$, 7, 9, and $11d$. Since the possible spacing between the impurities in our setup is a multiple of the array spacing, d, only a discrete set of energies give rise to such superradiance. The dashed lines indicate the predicted energy at which superradiance is observed, which corresponds to $k = (L - d)\pi/Ld$. The inset displays one of the plots used to obtain the green shaded regions. For $L = 9$, it shows the ratio between the decay rate into the array modes extracted from the numerical evolution with $n = 3$ and the expected decay rate of a single dimer into the array modes using FGR. Parameters for all the plots are $N = 500$, $d = \lambda_0/4$, $\Delta = 8\ \gamma_0$, and $\Omega = 0.2\ \gamma_0$.

prediction, Eq. (3.22). We extract these regions from plots like the sample that we show as an inset, in which we show Γ_{1D} as a function of k. This collective emission can be exploited to achieve larger Γ_{1D}/Γ'_{0-}.

3.5.2 Non-Markovian regime

The breakdown of the Markovian regime due to the diverging density of states at the edge of the band discussed before is also observable in waveguide QED setups [71, 72]. In our system, we observe another type of non-Markovianity due to the finite array length. Note that the results discussed above are independent of the number of array atoms, N, except that the decay rate Γ_k of the subradiant array modes is slightly larger for smaller N. However, the length of the array determines the time for which the dynamics stay Markovian [see the shaded regions in Fig. 3.5.1 and Fig. 3.5.2(right)]. For a dimer aligned with the center of the array, the outgoing plane waves return to the dimer after a characteristic time-scale $\tau = Nd/v_g = Nd/\partial_k J_k$, where v_g is the mode's group velocity, due to reflection at the ends of the array. We understand these non-Markovian effects as the retarded back-action via the reflected electric field of the emitter. Mathematically, these non-Markovian effects originate from the discrete spectrum of the atomic waveguide

[73], as the dynamics of the emitter at long times are able to resolve the energy difference between two array modes.

The evolution of the array and dimer population in the non-Markovian regime is highly dependent on the resonance energy of the dimer, which makes the system highly tunable. We can distinguish two particular cases (i) when the dimer is resonant with an anti-symmetric array mode and (ii) when its energy is resonant with a symmetric array mode. The phase of the reflected wave at the dimer's position differs by a factor of π in the two cases. In the first case, the reflected wave is in phase with the dimer and leads to an enhanced emission [note the kink in Fig. 3.5.1(left)]. In the second case, the reflected wave accumulates a difference in dynamical phase. Since the coupling rate of the dimer with a symmetric mode, $\tilde{\nu}$, at the center of the array is zero, the dimer energy effectively lies between two anti-symmetric modes. For large N, the energy difference with the two modes is approximately equal, $\Delta E \simeq \left|J_{k_{\tilde{\nu}\pm1}} - J_{k_{\tilde{\nu}}}\right|$, and $\tau \simeq \pi/\left|J_{k_{\tilde{\nu}\pm1}} - J_{k_{\tilde{\nu}}}\right|$, accumulating a phase difference $\varphi = \Delta E \tau \simeq \pi$. The reflected wave is, thus, out of phase and leads to an increase of population in the dimer, as can be seen in Fig. 3.5.1(right). The interaction with the reflected field can also be understood as the dimer interacting with its mirror image [74, 75], in which the non-Markovian effects are a form of retarded Dicke super or subradiance, with the emitters having (i) parallel or (ii) opposite polarization, respectively [60]. The slow propagation of the guided modes, especially close to the band edge, enhances the retardation effects responsible of the non-Markovian behavior.

3.6 Band-gap dynamics

If the dimer state resonance energy is located at the band-gap of the array, such that the detuning with the band edge, $\delta = \omega_{\mathrm{a}}' - J_{\frac{\pi}{d}}$, is larger than the coupling strength to the corresponding array modes, $g_{\frac{\pi}{d}}'$, the emission into the array is blocked. However, an atom–photon bound state with an exponentially decaying tail is formed [56], as depicted in Fig. 3.6.1. The width of the tail scales as $1/\sqrt{\delta}$ and, for sufficiently small δ, an overlap between distant atoms can be obtained [40, 41], giving rise to coherent interactions. Note that the array modes are off-resonant with the dimers, for which they do not acquire population during this process.

In this section, we study this regime for our system, and show that we can realize the same physics with atom-based waveguides, allowing for the long-range exchange of population between dimers with high fidelities. In Section 3.6.1, we derive the effective model for the time dynamics in this regime. In Section 3.6.2, we show array-mediated Rabi oscillations between distant dimers and discuss their scaling with the

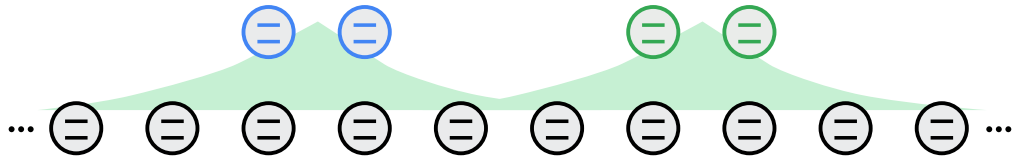

Figure 3.6.1: Schematic depiction of the atom–photon bound states that originate for dimer energies in the band gap. The waveguide-mediated effective interaction between dimers depends on the overlap between the exponential tails of the bound states, whose width scales as $\sqrt{1/\delta}$, where δ is the detuning of the dimers with the edge of the band.

system parameters. Finally, in Section 3.6.3, we discuss the different sources of loss in the system and make some predictions for the expected fidelity. Here, we observe a discrepancy between our results and the prediction for an infinitely long array, whose origin we explain in Section 3.6.4, where we discuss the scaling with system size of the optimal fidelity of a finite array.

3.6.1 Effective dimer–dimer long-range interaction

Assuming that the dimers' energy is off-resonant with the guided modes of the array, we can adiabatically eliminate the array modes in Eq. (3.20). For this, as we did in Section 3.4.2, we start by writing the evolution of the wavefunction coefficients associated to the operators a'_{i-} and b_k under the Hamiltonian Eq. (3.20)

$$\dot{a}'_{i-}(t) = -i\left(\omega_{\mathrm{a}}{}' - \frac{i}{2}\Gamma'_{0-}\right) a'_{i-}(t) - i\sum_k g'_k\, e^{ik\rho_i}\, b_k(t) \tag{3.23}$$

$$\dot{b}_k(t) = -i\left(J_k - \frac{i}{2}\Gamma_k\right) b_k(t) - i\sum_i g'_k\, e^{-ik\rho_i}\, a'_{i-}(t)\ . \tag{3.24}$$

Moving to a rotating frame, $\tilde{a}'_{i-}(t) = a'_{i-}(t)\, e^{i\omega_{\mathrm{a}}{}' t}$ and $\tilde{b}_k(t) = b_k(t)\, e^{iJ_k t}$, solving for $\tilde{b}_k(t)$, and substituting into the equation for $\dot{\tilde{a}}'_{i-}(t)$, we obtain an effective equation for the dimer's population,

$$\dot{\tilde{a}}'_{i-}(t) = -\frac{\Gamma'_{0-}}{2}\tilde{a}'_{i-} - i\sum_{k,j} {g'_k}^2\, e^{ik(\rho_j-\rho_i)} \int_0^t \mathrm{d}t'\, e^{i[\omega_{\mathrm{a}}{}' - (J_k - \frac{i}{2}\Gamma_k)](t-t')} \tilde{a}'_{j-}(t')\ . \tag{3.25}$$

We assume that, after summing over momenta, the time integral only contributes for a small correlation time τ_c (Markov approximation). Since g'_k is approximately constant close to the band edge, the region that is closest in resonance with the dimers, τ_c is short. Assuming that the dimer operator evolves over time scales much longer than τ_c, we approximate $\tilde{a}'^{\dagger}_{i-}(t') \simeq \tilde{a}'^{\dagger}_{i-}(t)$. For $t \gg \tau_c$ and $\omega'_{\mathrm{a}} - J_{\pi/d} > 0$, the

equation for the evolution of the dimer population reads

$$\begin{aligned}\dot{a}'_{i-}(t) = &- i\left(\omega_{\mathrm{a}}{}' - \frac{i}{2}\Gamma'_{0-}\right) a'_{i-}(t) \\ &-i\sum_{k,j} \frac{{g'_k}^2}{\omega_{\mathrm{a}}{}' - \left(J_k - \frac{i}{2}\Gamma_k\right)} e^{ik(\rho_j-\rho_i)}\, a'_{j-}(t)\,,\end{aligned} \tag{3.26}$$

from which we can infer the following effective dimer–dimer interaction

$$\hat{H}^{\mathrm{LR}}_{\mathrm{eff}} = \sum_{i,j,k} \frac{{g'_k}^2}{\omega_{\mathrm{a}}{}' - J_k + \frac{i}{2}\Gamma_k} e^{ik(\rho_i-\rho_j)}\, \hat{a}'^{\dagger}_{i-}\hat{a}'_{j-}. \tag{3.27}$$

For a small detuning of the dimers with the band edge $\delta = \omega'_{\mathrm{a}} - J_{\frac{\pi}{d}}$, the major contributions to the sum over k above are concentrated around $k = \pi/d$. We thus approximate the band at the edge of the Brillouin zone as $J_{\frac{\pi}{d}(1-x)} = J_{\frac{\pi}{d}} - A_d\, x^2$, and $g'_k \simeq g'_{\frac{\pi}{d}}$, since g_k varies slowly close to $k = \pi/d$ (see Fig. 3.4.2). Likewise, the decay rate of the most subradiant modes can be approximated by $\Gamma_{\frac{\pi}{d}(1-x)} \simeq \gamma_N\, x^2$ [28], with $\gamma_N/\gamma_0 \simeq 1/N$. For subwavelength arrays, we have $\gamma_N/A_d < 1/N$. For compactness, we use $\tilde{A}_d = A_d + \frac{i}{2}\gamma_N$. With these approximations and in the continuum limit, $\Sigma_k \to \frac{Nd}{2\pi}\int \mathrm{d}k$, we obtain a closed form for the effective coupling between two dimers mediated by the guided modes of the array (see Appendix 3.C),

$$H^{\mathrm{LR}}_{\mathrm{eff}} \simeq \sum_{i,j} g^{ij}_{\mathrm{eff}}\, e^{i\frac{\pi}{d}(\rho_i-\rho_j)}\, \hat{a}'^{\dagger}_{i-}\hat{a}'_{j-}\,, \tag{3.28}$$

with

$$g^{ij}_{\mathrm{eff}} = \frac{N\pi {g'_{\frac{\pi}{d}}}^2}{2\sqrt{\tilde{A}_d\,\delta}}\, e^{-\frac{\pi}{d}|\rho_i-\rho_j|/l}\,, \tag{3.29}$$

where we identified the length scale of the interactions $l = \sqrt{\tilde{A}_d/\delta}$. These expressions are valid as long as $\delta \gg g^{ij}_{\mathrm{eff}}$, such that elimination of the array modes is justified.

3.6.2 Rabi oscillations between distant dimers

We consider a system of two dimers separated by a distance L with a negligible free-space interaction. Initializing the system with the excitation in one of the dimers, and for a sufficiently large g^{ij}_{eff} in relation to the free-space decay, Eq. (3.28) predicts array-mediated Rabi oscillations between the dimers, as shown in Fig. 3.6.2 for a distance $L = 14\,d$. The fidelity of the population exchange is dictated by the ratio $g^{ij}_{\mathrm{eff}}/\Gamma'_{0-}$. This ratio does not depend on the Raman transition parameters Δ and

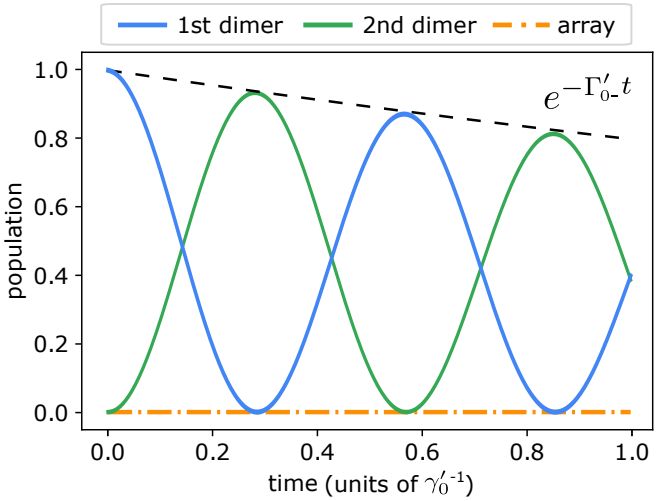

Figure 3.6.2: Population dynamics for two dimers with a separation $L = 14\,d$, and a detuning with the band edge $\delta = \epsilon^{-1} g^{ij}_{\text{eff}}$, with $\epsilon = 2 \times 10^{-3}$. The dimer lines represent the anti-symmetric state of the dimers, and the array integrates the population of all array modes. The population of the rest of the states is negligible. The dashed line indicates the dimer's free space decay. Here we use $d = \lambda_0/4$, $N = 100$, $\Delta = 200\gamma_0$, and $\Omega = 0.03\gamma_0$.

Ω. However, a small Ω/Δ allows reducing g^{ij}_{eff} while staying off-resonant with the array. Thus, one can still fulfill $\delta \gg g^{ij}_{\text{eff}}$ with a smaller detuning δ. Fixing the ratio $\epsilon = g^{ij}_{\text{eff}}/\delta$, we can rewrite Eq. (3.29) as

$$\frac{g^{ij}_{\text{eff}}}{\Gamma'_{0-}} = \frac{\epsilon^{1/3}}{\Gamma_{0-}} \left(\frac{\Delta}{\Omega}\right)^{2/3} \left(\frac{N\pi \left|g^{-}_{\frac{\pi}{d}}\right|^2}{\sqrt{\tilde{A}_d}}\right)^{2/3} e^{-\frac{2\pi}{3d}|\rho_i - \rho_j|/l}\,. \tag{3.30}$$

Note that, as expected from the continuum limit, Eq. (3.30) is independent of N, since $|g^{-}_{k}| \sim 1/\sqrt{N}$, with the exception of small corrections due to a finite $\Gamma_k(N)$, which vanishes for large N. The dependency on Δ/Ω indicates that the effective coupling can be made arbitrarily large at the expense of slower dynamics.

3.6.3 Analysis of the fidelity of a full Rabi cycle

We aim at maximizing the fidelity of preparing the first dimer again in the excited state after one full Rabi cycle. We measure the error from the numerical evolution as one minus the first relative maximum of population of the initial dimer.

The error of the protocol due to population loss to free space comes from (i) the free space decay rate Γ'_{0-} of the dimers and (ii) the finite linewidth Γ_k of the guided modes that mediate the interactions. There is also a small dephasing contribution to the exponential envelope, which we neglect in our discussion. Another source to the measured error is (iii) the transfer of population to the array modes. When

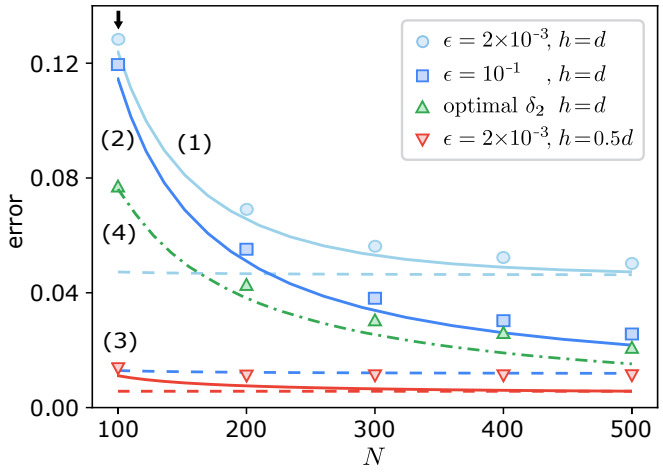

Figure 3.6.3: Error defined as the population loss in the initial dimer after one full Rabi cycle, i.e., one minus the first relative maximum of the "1st dimer" in Fig. 3.6.2. The black arrow indicates the point extracted from Fig. 3.6.2. The markers represent the values extracted from the numerical evolution of the full system initialized at one of the dimers' anti-symmetric state, while the lines correspond to analytical predictions for the markers with the same color. The solid lines are computed with Eq. (3.27). The dashed lines represent the continuum limit, Eq. (3.28). The dash-dotted line corresponds to Eq. (3.36) for an optimal δ_2 given by Eq. (3.35). Here we use $d = \lambda_0/4$, $L = 14d$, $\Delta = 200\gamma_0$, and $\Omega = 0.03\gamma_0$.

$\Gamma'_{0-} \ll \mathrm{Re}[g^{ij}_{\mathrm{eff}}]$, the first contribution is approximated as $\pi\Gamma'_{0-} \,/\, \mathrm{Re}[g^{ij}_{\mathrm{eff}}] \sim \epsilon^{-1/3}$, which is minimized for large values of ϵ. The third contribution, instead, grows with ϵ, as the maximum population transferred to the array during the dynamics can be shown to be upper bound by a function proportional to ϵ (see Appendix 3.D.1). The second contribution to the error is independent of ϵ, and has a value $\gamma_N/(2A_d) \sim 1/N$, which sets a lower bound to the error independent of the ratio Ω/Δ.

In Fig. 3.6.3, we plot the error for dimers interacting with arrays of different lengths. We compare the numerical results with the predictions by Eq. (3.27) and Eq. (3.28), which both include the first and second sources of error described above. We discuss four scenarios labeled (1-4) in Fig. 3.6.3. Case (1) corresponds to the regime $\delta \gg g'_k$, for which the only relevant source of error is Γ'_{0-}. Case (2) corresponds to the regime $\delta \sim g'_k$, in which a smaller error is obtained in expense of an exchange of population with the array modes. Case (3) shows that placing the dimer closer to the array as compared to the lattice spacing d reduces the error thanks to the larger effective coupling rate $g'_{\frac{\pi}{d}}/\Gamma'_{0-}$. The improvement is remarkable already at small N. Finally, because of the discrete nature of the modes, the prediction in the continuum limit, Eq. (3.28), leads to an overestimation of the resonance frequency of the modes near the band edge (see Appendix 3.D.2). This explains the disagreement of the results for a finite array with the prediction assuming an infinite array, indicated with horizontal dashed lines, especially at smaller N. Taking this into consideration, we can optimize the resonance energy of the emitters for

finite arrays, which we show as case (4) and we discuss in the following. Note that, although barely captured in the plots, the population in the array modes becomes non-negligible for smaller $\delta/g_{\text{eff}}^{ij}$, as in cases (2) and (4) with larger N.

3.6.4 Optimizing the fidelity for finite arrays

Since the resonance energy of the highest array eigenstate is lower than the band edge obtained in the infinite-length limit, we can obtain a larger effective coupling between distant dimers by taking $\delta < 0$, while staying off-resonant with the array modes. For this, we define a new detuning between the dimer and the highest-energy array mode, $\delta_2 = \omega_{\text{a}}' - J_{k_N} > 0$. The condition $\delta_2 \gg g_{\text{eff}}^{ij}$ can again be made arbitrarily small by tuning Ω/Δ. For small δ_2, however, Γ_k also becomes a dominant source of error. In this section, we minimize the error for the simplified model including only the interaction with the highest-energy array mode and obtain an optimal δ_2 for which we predict an error that scales as $1/N$, as we show in case (4) in Fig. 3.6.3. The error deviates from the prediction at larger N, as the energy spacing between array modes is reduced with N and, thus, the contribution of further array modes becomes non-negligible, for which one should go back to using Eq. (3.27).

Analyzing the system from the picture of a discrete spectrum of array modes with momenta k_μ, as defined in Section 3.C and sketched in Fig. 3.D.1 (left), instead of a continuous band, the expression for the effective dimer–dimer coupling reads

$$g_{\text{eff}}^{ij} \simeq g_{\frac{\pi}{d}}'^2 \sum_{\mu=1}^{N} \frac{\xi_{k_\mu}^{-}(\rho_i)\,\xi_{k_\mu}^{-*}(\rho_j)}{\delta + \left(A_d + \frac{i}{2}\gamma_N\right)\frac{\mu^2}{N^2}} \,. \tag{3.31}$$

Introducing the detuning, δ_2, of the emitters from the highest ($\mu = 1$) energy mode of the array,

$$g_{\text{eff}}^{ij} \simeq g_{\frac{\pi}{d}}'^2 \sum_{\mu=1}^{N} \frac{\xi_{k_\mu}^{-}(\rho_i)\,\xi_{k_\mu}^{-*}(\rho_j)}{\delta_2 + \frac{i}{2}\gamma_N\frac{\mu^2}{N^2} + \frac{A_d}{N^2}\left(\mu^2 - 1\right)} \,. \tag{3.32}$$

To stay off-resonant with the mode $k_{\mu=1}$, we need $\delta_2 > \frac{\gamma_N}{N^2}$. For $N \gg 1$, $(\delta_2 - J_{k_2}) = \frac{3A_d}{N^2} \gg \frac{\gamma_N}{N^2} \sim \delta_2$. Thus, we approximate Eq. (3.32) with the first term of the sum,

$$g_{\text{eff}}^{ij} \simeq g_{\frac{\pi}{d}}'^2 \frac{\delta_2 - i\frac{\gamma_N}{2N^2}}{\delta_2^2 + \left(\frac{\gamma_N}{2N^2}\right)^2} \,, \tag{3.33}$$

where for simplicity we have also used $\xi_{k_1}^{-}(\rho_i)\xi_{k_1}^{-*}(\rho_j) \simeq 1$, valid for a long array and dimers located near its center.

As discussed in Section 3.6.3, the dimer–dimer long-range coupling has three main sources of error. Here, we include the free-space decay of the dimers, $\pi\,\Gamma_{0-}'/\text{Re}[g_{\text{eff}}^{ij}]$ after one full Rabi cycle and the decay of the array mode that we are considering in

this model, $2\pi\,\mathrm{Im}[g^{ij}_{\mathrm{eff}}]/\mathrm{Re}[g^{ij}_{\mathrm{eff}}]$. We neglect the finite population transfer to the array mode, upper bound by $4g'^2_{\frac{\pi}{d}}/(\delta_2^2+4g'^2_{\frac{\pi}{d}})$, if $\delta_2 \gg g'_{\frac{\pi}{d}}$ is not satisfied. The error reads

$$\text{error} \;\simeq\; \frac{\pi\Gamma_{0-}}{\left|g^{-}_{\frac{\pi}{d}}\right|^2}\,\delta_2 \;+\; \pi\frac{\gamma_N}{N^2}\,\frac{1}{\delta_2}\,. \tag{3.34}$$

By minimizing the error, we obtain an optimal value of δ_2

$$\delta_2^{\mathrm{opt}} = \frac{\left|g^{-}_{\frac{\pi}{d}}\right|}{\sqrt{N^2\,\Gamma_{0-}/\gamma_N}}\,, \tag{3.35}$$

for which we predict an error

$$\text{error}_{\mathrm{opt}} \simeq \frac{2\pi}{\left|g^{-}_{\frac{\pi}{d}}\right|}\,\frac{\sqrt{\Gamma_{0-}}}{N^{3/2}}\,. \tag{3.36}$$

Since $\left|g^{-}_{\frac{\pi}{d}}\right|$ scales as $1/\sqrt{N}$, the optimal error scales as $1/N$.

3.7 Physical Feasibility

Throughout this chapter, we have assumed a lattice spacing of $d = 0.25\,\lambda_0$. Our methods apply equally well to smaller interatomic separations. They also offer a substantial improvement at larger separations closer to the limit $d = 0.5\,\lambda_0$. The suppression of the coupling of the dimer's anti-symmetric state to the superradiant modes of the array becomes only partial at larger d, resulting in increased decay rates. Nevertheless, the features of interest discussed in this chapter are retained, as we show, as a mode of example, for $d = 0.4\,\lambda_0$ in Fig. 3.7.1. At any rate, creating lattices with $d < 0.5\,\lambda_0$ is currently an experimental challenge and, in this section, we briefly discuss some of the issues and potential solutions.

To create an atomic array with a subwavelength lattice spacing, there are some proposals that exploit the fact that one can use one transition to trap atoms in an optical lattice, and another – less energetic – transition as the main dipole transition. A scheme for alkaline-earth atoms has been proposed [76]. In this scheme, a trapping laser with wavelength $\lambda_{\mathrm{opt}} \sim 400$ nm is used to trap atoms which are then excited on a dipole transition with characteristic wavelength $\lambda_0 \sim 2.6\ \mu$m, thus achieving in principle a ratio $d/\lambda_0 \sim 0.08$ (where $d = \lambda_{\mathrm{opt}}/2$). While this proves the possibility to realize highly subwavelength lattices in the future, a less demanding interatomic separation of order $\lambda_0/4$ might be already within reach, as in [77], where the experimental realization of a $\lambda_0/4$ stroboscopic optical lattice has been

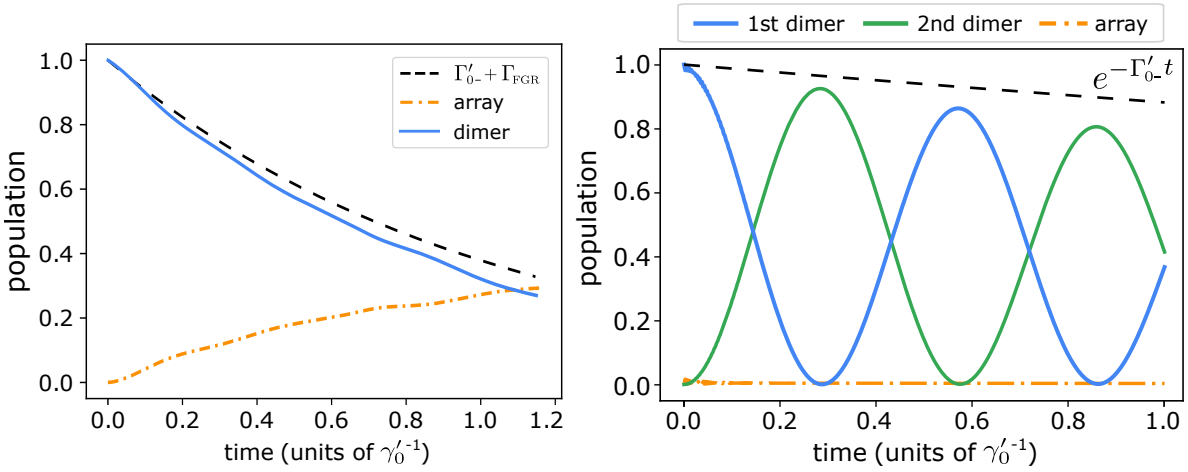

Figure 3.7.1: Population dynamics of a dimer anti-symmetric state in a setup with $d = 0.4\,\lambda_0$. The dimer lines represent the anti-symmetric state of the dimer, and the array line integrates the population of all array modes. The population of all other states is negligible. The loss of total population is due to free space decay. The solid lines are computed with the full-system Hamiltonian, Eq. (3.19). The offset of the dimer population with respect to the dashed lines is due to the coupling of the anti-symmetric dimer's state to the superradiant modes of the array, which is not entirely suppressed at larger d. (left) Dynamics for an emitter in the band, resonant with $k\cdot = 0.967\pi/d$. The dashed line indicates the prediction including FGR and the dimer's free space decay. Here we use $N = 500$, $\Delta = 8\ \gamma_0$, and $\Omega = 0.2\ \gamma_0$. (right) Dynamics in the band-gap showing Rabi oscillations between two dimers with a separation $L = 14d$. Here we use $\epsilon = 1$, $\Delta = 200\gamma_0$, and $\Omega = 0.01\gamma_0$.

demonstrated.

An emitter–array separation smaller than the interatomic spacing of the array could be achieved by engineering the trapping potential using optical superlattices [78–82]. This is experimentally more challenging, but leads to large improvements in the fidelity as shown in Fig. 3.6.3.

Coupling light to the subradiant modes of the array is also a challenge itself. There are different proposals using, for instance, phase imprinting techniques (proposed in [83] and realised in [84]), or exciting a multi-photon transition [85]. In our setup, we study the case in which the target atoms are excited, and these couple to the subradiant modes. We propose to excite the dimer atoms without affecting the array atoms by placing the array on a node of the laser field. Optionally, the Raman laser could be used to shift the transition frequency to outside the array bandwidth, which allows for frequency-selective coupling. Driving the anti-symmetric excitation of the dimer, however, might also be challenging due to its reduced coupling to light. Similar techniques than the ones mentioned above to excite the subradiant modes of the array could be used on the anti-symmetric state of the dimer.

The atomic array may have imperfections in its preparation. Although we have not studied the effect of vacancies in the array, we expect this to be a problem, as

they create defects that scatter the photon propagating in the array. This issue is discussed in the supplemental material of [86]. One could consider repeating the preparation of the array until a perfect array is created.

Finally, the finite spread of the atom wavefunctions on the trapping potential needs to be considered. This issue is discussed for a similar setup in [85]. We expect it to increase the linewidth of the subradiant array modes and, thus, to reduce the fidelity of the results shown here. Since the physics that we observe in this chapter do not rely on resolving a very narrow feature in the spectrum of the Hamiltonian, we expect that the discussed phenomena survives after introducing atomic motion in the model. One exception might be the ability to resolve the different non-Markovian dynamics discussed in Section 3.5.2 because of the broadening of the discrete guided modes. We leave a more detailed discussion on accounting for atomic motion and describing it effectively, for Chapter 4.

3.8 Discussion and Outlook

In this chapter, we have proposed a setup to achieve a coherent and Markovian interaction between an emitter and the subradiant modes of an atomic array, a system which mirrors conventional waveguide QED of atoms coupled to waveguides. Our proposal is based on two main ingredients: (i) the use of ground and anti-symmetric dimer states as an effective two-level system and (ii) the use of a Raman transition to control the linewidth of the dimer. The first method exploits the particular symmetry of the dimer state to improve the coherent coupling to the array's guided modes by decoupling the emitter from the highly radiating modes of the array. The second method allows to reduce the dimer's linewidth as compared to the array's bandwidth, thus achieving the regime of Markovian dynamics. Accordingly, we observe similar dynamics as in conventional waveguide QED both in the in-band and band-gap regimes for the case of an atomic array with interatomic separation of quarter wavelength. Along with the well-known Markovian dynamics, we also observe non-Markovian effects due to the finiteness of the array and retardation effects introduced by the slow group velocity at the band edge.

Another approach to suppress the coupling of the emitter to the superradiant modes of the array consists on positioning the emitter at "magic points" [63]. It could be interesting to combine this idea with the methods used in this chapter to yet further improve the optical depth of the system. The reflection of the excitations at the ends of the atomic waveguide gives rise to non-Markovian effects, as discussed in Section 3.5.2. To increase the time during which the dynamics stays Markovian, it could be interesting to study ways of engineering the ends of the array

to encourage emission, as in [28]. While here we focused on a simple linear geometry for both the array and the dimers, in analogy to the conventional setup of atoms coupled to a waveguide, several generalizations could be considered. In particular, since in the band-gap regime of emitter–array coupling the fidelity is ultimately limited by the intrinsic decay of the array's dark modes, we could consider emitters coupled to an atomic ring – the atomic equivalent of a ring-resonator–, where subradiant modes are expected to have an exponential suppression of the decay rate as $\sim \gamma_0 \exp(-N)$ [28, 87]. Furthermore, it would be interesting to exploit the dimer interference to reduce the coupling to the array's bright modes also in 2D and 3D lattices. In higher-dimensional lattices, the use of dimers (or the corresponding generalization) could be particularly advantageous due to the scaling with the array's size of the superradiant modes' linewidth [68]. Finally, while we only considered $d = \lambda_0/4$, our methods apply equally well to smaller interatomic separations, where the system's dynamics would benefit from the additional reduction in the decay to free space.

This work paves the way toward observing and exploiting the rich phenomenology of waveguide QED in a clean, atom-based, setup. The additional non-Markovian effects due to the finiteness of the array are difficult to observe in standard waveguide QED and are a distinguishing feature of this platform.

Appendix

3.A Analytical expressions for the interaction between emitters and array modes

In this appendix we outline the derivations of a closed expression for the coupling between a single atom emitter and a array mode k, as in Eq. (3.8), and of the extension to an atomic dimer to obtain Eq. (3.10).

The coupling between a target atom at $\mathbf{r}_i$ and a Bloch mode of the array in Eq. (3.6) reads

$$g_k^i - \frac{i}{2}\gamma_k^i = -\frac{3\pi\gamma_0}{k_0\sqrt{N}}\sum_j e^{-i\mathbf{k}\cdot\mathbf{r}_j}\, G_0^{zz}(\mathbf{r}_i,\mathbf{r}_j)\,. \tag{3.37}$$

We express Eq. (2.44) in cylindrical coordinates by using

$$\frac{e^{ik_0|\mathbf{r}_i-\mathbf{r}_j|}}{|\mathbf{r}_i-\mathbf{r}_j|} = \frac{i}{2}\sum_{m=-\infty}^{\infty}\int dk\, e^{im(\phi_j-\phi_i)}e^{ik(z_j-z_i)}J_m\left(k_\perp\rho_j\right)H_m^{(1)}\left(k_\perp\rho_i\right)\,, \tag{3.38}$$

where $\rho_i > \rho_j$, and J_m and $H_m^{(1)}$ are Bessel and Hankel functions of the first kind, respectively. For array atoms sitting on the $\hat{z}$ axis, $\rho_j = 0$ and $\phi_j = 0$, multiplying Eq. (3.38) by $e^{-i\mathbf{k}\cdot\mathbf{r}_j}$ and summing over the array atoms yields

$$\begin{aligned}
&\frac{i}{2}\sum_j\int dk'\, e^{ik'(z_j-z_i)}e^{-ikz_j}H_0^{(1)}\left(k_\perp\rho_i\right)\\
&= i\frac{\pi}{d}\sum_{m\in\mathbb{Z}}\int dk'\,\delta\left(k'-k-\frac{2\pi n}{d}\right)e^{-ik'z_i}H_0^{(1)}\left(k_\perp\rho_i\right)\\
&= i\frac{\pi}{d}\sum_{m\in\mathbb{Z}}e^{-i(k+\frac{2\pi n}{d})z_i}\,H_0^{(1)}\left(k_\perp\rho_i\right)\,.
\end{aligned} \tag{3.39}$$

Plugging Eq. (3.39) into Eq. (3.37) yields Eq. (3.8).

For an even N, setting $z = 0$ at the center of the array, $\mathbf{r}_j = dj\hat{z}$ with $j = -N+\frac{1}{2}, -N+\frac{3}{2}, \ldots, N-\frac{1}{2}$, and for dimer's atoms in position $\mathbf{r}_i^{\pm} = [h\hat{\rho} + (\rho_i \pm \rho_0)\hat{z}]$, the coupling to the symmetric ($\lambda = 1$) and anti-symmetric ($\lambda = -1$) state reads

$$g_k^{i\lambda} - \frac{i}{2}\gamma_k^{i\lambda} = -\frac{3\pi\gamma_0}{k_0\sqrt{2N}}\sum_j e^{-i\mathbf{k}\cdot\mathbf{r}_j}\left[G_0^{zz}(\mathbf{r}_i^+,\mathbf{r}_j) + \lambda G_0^{zz}(\mathbf{r}_i^-,\mathbf{r}_j)\right] \tag{3.40}$$

Assuming that the dimer is located far from the edges of the array, we can extend the sum to infinite j without affecting its total value. Shifting the origin to $\rho_i\hat{z}$, the sum above becomes

$$\begin{aligned}
&\sum_{j\in\mathbb{Z}+\frac{1}{2}} e^{-i\mathbf{k}\cdot(\mathbf{r}_j-\rho_i\hat{z})}\left[G_0^{zz}(\rho_0,j)+\lambda G_0^{zz}(-\rho_0,j)\right]\\
=\;& e^{ik\rho_i}\sum_{j\in\mathbb{Z}+\frac{1}{2}}\left[G_0^{zz}(\rho_0,j)e^{-i\mathbf{k}\cdot\mathbf{r}_j}+\lambda G_0^{zz}(-\rho_0,-j)e^{i\mathbf{k}\cdot\mathbf{r}_j}\right]\\
=\;& e^{ik\rho_i}\sum_{j\in\mathbb{Z}+\frac{1}{2}} G_0^{zz}(\rho_0,j)\left[e^{-i\mathbf{k}\cdot\mathbf{r}_j}+\lambda e^{i\mathbf{k}\cdot\mathbf{r}_j}\right] \qquad (3.41)\\
=\;& 2e^{ik\rho_i}\sum_{j\in\mathbb{Z}} G_0^{zz}\left(\rho_0-d/2,j\right)\begin{cases}\sin\left[k(r_j+\frac{d}{2})\right] & \text{if } \lambda=-1\\ \cos\left[k(r_j+\frac{d}{2})\right] & \text{if } \lambda=1\end{cases},
\end{aligned}$$

where $(-)\rho_0$ and j stand for $\left[\mathbf{r}_i^{+(-)}-\rho_i\hat{z}\right]$ and $\mathbf{r}_j$, respectively. For $\rho_0=d/2$, i.e., the emitters are aligned with the array atoms as in the text, we obtain Eq. (3.10). Repeating the above treatment with the finite-array Ansatz in Eq. (3.4) to replace e^{-ikr_j}, we derive the following definitions in the final result for $\lambda=-1$,

$$\xi^{-}_{k_\nu}(\rho_i)=\begin{cases}\sqrt{\frac{2}{N+1}}\sin(k_\nu\rho_i) & \text{if } \nu \text{ is odd}\\ \sqrt{\frac{2}{N+1}}\cos(k_\nu\rho_i) & \text{if } \nu \text{ is even}\end{cases}, \qquad (3.42)$$

and for $\lambda=1$,

$$\xi^{+}_{k_\nu}(\rho_i)=\begin{cases}\sqrt{\frac{2}{N+1}}\cos(k_\nu\rho_i) & \text{if } \nu \text{ is odd}\\ \sqrt{\frac{2}{N+1}}\sin(k_\nu\rho_i) & \text{if } \nu \text{ is even}\end{cases}. \qquad (3.43)$$

Note that, for a finite array, the eigenstates of the array consist of standing waves. In the infinite-array limit, neighboring even and odd modes as defined above are separated by an infinitesimally small energy. By considering the superposition of a pair of neighboring even and odd modes, the plane wave result is recovered.

3.B Derivation of the effective Hamiltonian with a Raman transition

In this appendix, we extend the effective description developed in Section 3.4.2 to the case of target atoms driven on a Raman transition (see Section 3.4.3). We start from Eq. (3.19) and separate it into a bare, $\hat{H}_0$, and an interacting, $\hat{V}$, part as

$$\hat{H}_{\mathrm{R}}=\hat{H}_0+\hat{V}, \qquad (3.44)$$

with

$$\begin{aligned}\hat{H}_0 = &\textstyle\sum_\alpha \left(\omega_{\mathsf{a}} - \frac{i}{2}\gamma_0\right) |e^\alpha\rangle \langle e^\alpha| + \sum_\alpha (\omega_{\mathsf{a}} - \Delta) |g_1^\alpha\rangle \langle g_1^\alpha| \\ &+ \textstyle\sum_k \left(J_k - \frac{i}{2}\Gamma_k\right) \hat{b}_k^\dagger \hat{b}_k + \left(\tilde{g}_{ab} |e^a\rangle\langle g_2^a| \otimes |g_2^b\rangle\langle e^b| + \text{h.c.}\right),\end{aligned} \tag{3.45}$$

and for target atoms at position $(h, 0, z_i)^T$

$$\hat{V} = \frac{\Omega}{2} \sum_\alpha \left(|g_1^\alpha\rangle\langle e^\alpha| + \text{h.c.}\right) + \sum_{k,\alpha} \left(\tilde{g}_k^i |e^\alpha\rangle\langle g_2^\alpha| \hat{b}_k + \text{h.c.}\right), \tag{3.46}$$

where we use the definition of $\tilde{g}_k^*$ in Section 3.4.2.

We shift the energy by $\Delta - \omega_{\mathsf{a}}$, such that the excited states $|e^\alpha\rangle$ evolve fast, and define the projectors

$$\begin{aligned}\hat{P} = &\left(|g_1^a\rangle\langle g_1^a| \otimes |g_2^b\rangle\langle g_2^b| + |g_2^a\rangle\langle g_2^a| \otimes |g_1^b\rangle\langle g_1^b|\right) \otimes |0\rangle\langle 0| \\ &+ |g_2^a\rangle\langle g_2^a| \otimes |g_2^b\rangle\langle g_2^b| \otimes \sum_k |1_k\rangle\langle 1_k| \,,\end{aligned} \tag{3.47}$$

and

$$\hat{Q} = \mathbb{1} - \hat{P} = \left(|e^a\rangle\langle e^a| \otimes |g_2^b\rangle\langle g_2^b| + |g_2^a\rangle\langle g_2^a| \otimes |e^b\rangle\langle e^b|\right) \otimes |0\rangle\langle 0| \,, \tag{3.48}$$

where $\hat{b}_k^\dagger |0\rangle = |1_k\rangle$. We then calculate $\hat{P}\hat{V}(\hat{Q}\hat{H}_0\hat{Q})^{-1}\hat{V}\hat{P}$ and use that, for $\Delta, \gamma_0 \gg \Omega, g_{ab}, \gamma_{ab}, g_k^i, \gamma_k^i$, and to second order in perturbation [88, 89],

$$\hat{H}_{\text{eff}} = \hat{P}(\hat{H}_0 + \hat{V})\hat{P} - \hat{P}\hat{V}(\hat{Q}\hat{H}_0\hat{Q})^{-1}\hat{V}\hat{P} \,. \tag{3.49}$$

The resulting effective Hamiltonian in the dimer eigenstate basis and after undoing the previous energy shift reads,

$$\begin{aligned}\hat{H}_{\text{eff}} = &\sum_{kk'} \left[\left(J_k - \frac{i}{2}\Gamma_k\right)\delta_{kk'} - \sum_\lambda \frac{\tilde{g}_k^{i\lambda *}\, \tilde{g}_{k'}^{i\lambda}}{(\Delta + \lambda g_{ab}) - \frac{i}{2}(\gamma_0 + \lambda\gamma_{ab})}\right] \hat{b}_k^\dagger \hat{b}_{k'} \\ &+ \sum_\lambda \left[\omega_{\mathsf{a}} - \Delta - \frac{\Omega^2}{4} \frac{(\Delta + \lambda g_{ab}) + \frac{i}{2}(\gamma_0 + \lambda\gamma_{ab})}{(\Delta + \lambda g_{ab})^2 + \frac{1}{4}(\gamma_0 + \lambda\gamma_{ab})^2}\right] \hat{a}_{i\lambda}'^\dagger \hat{a}_{i\lambda}' \\ &- \sum_{\lambda,k} \frac{\Omega/2}{(\Delta + \lambda g_{ab}) - \frac{i}{2}(\gamma_0 + \lambda\gamma_{ab})} \left(\tilde{g}_k^{i\lambda}\, \hat{a}_i^\dagger \hat{b}_k + h.c.\right) \,.\end{aligned} \tag{3.50}$$

Although we derive the effective Hamiltonian considering one dimer, the extension to multiple dimers in the case in which their interaction through free space is negligible is straightforward.

In the regime $\Delta \gg \gamma_0 \gg \Omega, g_{ab}, \gamma_{ab}, g_k^i, \gamma_k^i$, the dimer energy and the dimer–array

coupling can be approximated as in Eq. (3.20). For the dimer energy resonant with the subradiant region of the array's band, we can eliminate the symmetric dimer state and the superradiant array modes in the same way than in Section 3.4.2. Note that with the Raman transition, the symmetric state is also resonant with the subradiant modes. Nevertheless, its coupling is smaller and its linewidth larger than the one of the anti-symmetric state, and we verify that it can be safely neglected when studying the dynamics of the latter. In contrast to Section 3.4.2, the reduced dimer linewidth due to the Raman transition maintains the correction due to the superradiant array modes small at energies close to J_{k_0}.

The additional $\sim g_k^2$ term in Eq. (3.50) introduces small shifts in the energy of the array modes. We account for them by correcting the k axes in Fig. 3.5.3 with the momentum extracted from the array mode holding the excitation, which might not coincide exactly with the k expected from J_k.

3.C Analytical expression for effective coupling between dimers near the band-gap

In this appendix, we obatin an approximated analytical expression for the effective array-mediated dimer-dimer interaction of Eq. (3.27). The biggest contributions come from the momenta k near the band edge. To obtain a closed form of the effective coupling between dimers through the guided modes of the array, we approximate $g'_k \simeq g'_{\frac{\pi}{d}}$ and do a quadratic-band approximation of J_k around the band edge. Expanding the analytical form of the dispersion relation for an infinite array [28] around $k = \pi/d$ and truncating to second order, we obtain $J_{\frac{\pi}{d}(1-x)} \simeq J_{\frac{\pi}{d}} - A_d\, x^2$, with

$$A_d = \frac{3\pi^2\gamma_0}{2k_0^3 d^3}\left[\log\left[2\cos\left(\frac{k_0 d}{2}\right)\right] + \frac{k_0 d}{2}\tan\left(\frac{k_0 d}{2}\right)\right], \tag{3.51}$$

for $d < \lambda_0/2$. In particular, for $d = \lambda_0/4$, $A_d/\gamma_0 \simeq 4.3$. Defining $\mu \in [1, N]$ that labels the discrete momenta $k_\mu = \frac{\pi}{d}\left(1 - \frac{\mu}{N+1}\right)$, the decay rate of the most subradiant modes scales as $\Gamma_\mu \simeq \gamma_N \mu^2/N^2$ [28]. Thus, $\Gamma_{\frac{\pi}{d}(1-x)} \simeq \gamma_N x^2$, and in the continuous band approximation,

$$\sum_k \frac{{g'_k}^2\, e^{ik(\rho_i-\rho_j)}}{{\omega_a}' - J_k + \frac{i}{2}\Gamma_k} \simeq \frac{N{g'_{\frac{\pi}{d}}}^2}{2\,\delta}\int_{-1}^{1} dx\, \frac{e^{i\frac{\pi}{d}(\rho_i-\rho_j)(1-x)}}{1 + \frac{1}{\delta}\left(A_d + \frac{i}{2}\gamma_N\right)x^2}, \tag{3.52}$$

where $\delta = {\omega_a}' - J_{\frac{\pi}{d}}$. For $\delta \ll A_d$, the integration limits can be extended to infinity without affecting the solution. We introduce the parameter η by substituting $(1 - x)$ with $(\eta - x)$. Using the convolution theorem $(f * g)(\eta) =$

$\mathcal{F}^{-1}\{\mathcal{F}(f)\cdot\mathcal{F}(g)\}$, and the results of the Fourier transform $\mathcal{F}(e^{ik\rho x})(\nu)=\delta(k\rho-\nu)$, and $\mathcal{F}\left((1+A\,x^2)^{-1}\right)(\nu)=\frac{\pi}{\sqrt{A}}e^{-|\nu|/\sqrt{A}}$, Eq. (3.52) becomes

$$\begin{aligned}\sum_k \frac{{g_k'}^2\, e^{ik(\rho_i-\rho_j)}}{{\omega_a}' - J_k + \frac{i}{2}\Gamma_k} \simeq \frac{N\pi}{2}\frac{{g'_{\frac{\pi}{d}}}^2}{\delta}\sqrt{\frac{\delta}{A_d+\frac{i}{2}\gamma_N}} \\ \times\int_{-\infty}^{\infty} d\nu\, e^{i\nu\eta}\,\delta\left(\frac{\pi}{d}(\rho_i-\rho_j)-\nu\right)e^{-|\nu|\sqrt{\delta/(A_d+\frac{i}{2}\gamma_N)}}\,,\end{aligned} \tag{3.53}$$

and Eq. (3.28) and Eq. (3.29) follow trivially. Note that the exponential envelope in real space introduces a length scale for the interactions $l=\sqrt{A_d/\delta}$.

3.D Analysis of error in the band-gap dynamics

3.D.1 Error due to populating the array modes

In the regime in which $\delta \gg g'_{\frac{\pi}{d}}$ is not satisfied, but $\epsilon = g'_{\frac{\pi}{d}}/\delta$ is still small, the transition probability to the array modes from an initial dimer state with energy $J_{\frac{\pi}{d}}+\delta$ and to lowest order in interaction [22]

$$\mathcal{P}(t)=4\,g'^2_{\frac{\pi}{d}}\sum_k \frac{\sin^2\left[\left(J_{\frac{\pi}{d}}+\delta-J_k\right)t/2\right]}{\left(J_{\frac{\pi}{d}}+\delta-J_k\right)^2}\,. \tag{3.54}$$

In the continuum limit, $\Sigma_k \to \frac{Nd}{2\pi}\int dk$, we approximate an expression for the absolute maximum of population at the array

$$\max[\mathcal{P}(t)] \simeq \frac{5}{2}N\epsilon^{3/2}\sqrt{\frac{g'_{\frac{\pi}{d}}}{A_d}}\,. \tag{3.55}$$

Note that this probability is an upper bound both because it is the maximum of population at the array and because the integral in the continuum limit overestimates the value of the sum over k for a small $\delta/(J_{\frac{\pi}{d}}-J_{\frac{\pi}{d}(1-1/N)})$, as discussed in Section 3.6 and Appendix 3.D.2. Since here we compute $1/\delta^2$, the mismatch between the results from using a continuum or a discrete band scales faster than in the calculation of g^{ij}_{eff}. Finally, the error defined in the text is not well suited to capture error due to populating the array modes, as the time scale of the oscillations between array and dimers is much shorter than the one of the oscillations between dimers. The error at the dimer's maximum is, therefore, most likely measured at a time in which the population in the array is zero, as the probability that such point of time exists close to the maximum of dimer population is high.

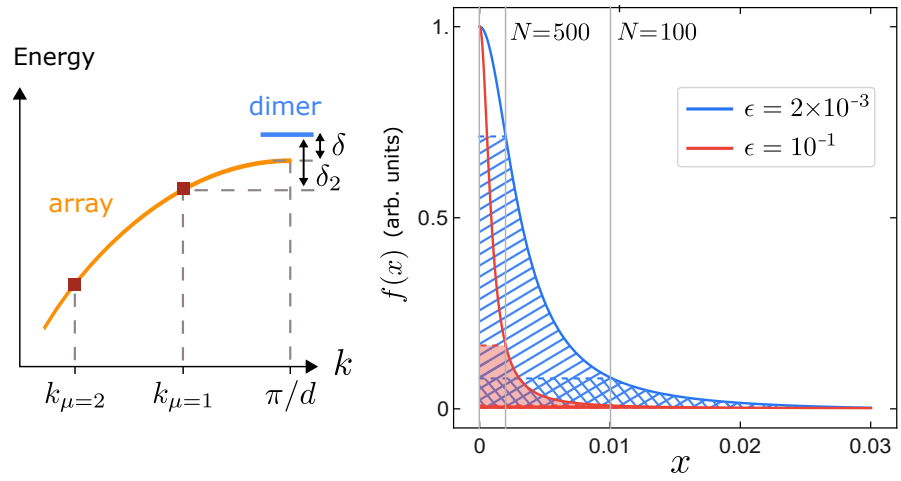

Figure 3.D.1: (left) Sketch of the energy of the system consisting of emitters in the array's band-gap discussed in Section 3.6. The solid line represents the array's band in the continuum limit, while the markers point at the discrete levels of a finite array. The dimer energy is detuned by δ with the band edge, and by δ_2 with the highest-energy discrete state. (right) $f(x)$ [see Eq. (3.56)] for the different values of $\epsilon = g^{ij}_{\text{eff}}/\delta$ used in Fig. 3.6.3. The three vertical lines indicate, from left to right, $x = 0$ and the value of x corresponding to $k_{\mu=1}$, $x = \mu/(N+1)$, for $N = 500$ and $N = 100$, respectively. The shaded regions highlight the area under $f(x)$ obtained by integrating between $x = 1$ and $x = 1/(N+1)$, and integrating a constant value from that point to $x = 0$. The parameters used are $d = \lambda_0/4$, $\Delta = 200\gamma_0$, and $\Omega = 0.03\gamma_0$.

3.D.2 Prediction mismatch due to the finite array size

In Fig. 3.6.3, we observe a difference between the effective dimer–dimer interaction as described by Eq. (3.27) and Eq. (3.28) for a dimer' energy in the band-gap, as depicted in Fig. 3.D.1 (left). This disagreement is due to the discreteness of the array modes, for which the highest-energy mode has quasi-momentum $k_{\mu=1}$ (see Section 3.6.1), with $k_{\mu=1} \simeq \frac{\pi}{d}(1-1/N)$. Since the biggest contributions to g^{ij}_{eff} come from the modes closest in energy to the band edge, and $J_{k_{\mu=1}} < J_{\frac{\pi}{d}}$, the larger detuning between the dimer and the mode with $k_{\mu=1}$ (δ_2 in Fig. 3.D.1) explains the smaller coupling rates predicted by Eq. (3.27). In other words, the approximation in Eq. (3.52) may not be appropriate below a certain N.

We can better understand the mismatch between the discrete and infinite array predictions by looking at the integrand in Eq. (3.52)

$$f(x) = \frac{\cos\left[\frac{\pi}{d}(\rho_i - \rho_j)x\right]}{1 + \frac{1}{\delta}A_d\, x^2}\,, \tag{3.56}$$

as we do in Fig. 3.D.1 (right). For simplicity, we focus the comparison on the most dominant term of the discrete sum, the one with $k_{\mu=1}$, for which the difference in total value between the two sides of Eq. (3.52) is captured by the non-shaded areas

in Fig. 3.D.1. For instance, the ratio between the non-shaded part of the area under $f(x)$ and the full integral is rather small for $\epsilon = 2 \times 10^{-3}$ and $N = 500$, and the offset between the corresponding marker and dashed line in Fig. 3.6.3 is also small. However, the steepness of the function at small x can lead to large underestimations of the area under the function. This becomes critical at smaller N. For $\epsilon = 2 \times 10^{-3}$ and $N = 100$, the non-shaded part amounts to multiple times the shaded part of the area under $f(x)$. The value of the mismatch between the discrete and continuum predictions also depends on δ, as smaller δ are better able to resolve the detuning of the mode $k_{\mu=1}$ with the band edge. In other words, $f(x)$ becomes steeper, and the amount of underestimation of the integral using the discrete sum is larger, as shown in Fig. 3.D.1 for $\epsilon = 10^{-1}$. This, again, can be verified by observing Fig. 3.6.3.

The predictions with Eq. (3.28) are, thus, in general overly optimistic. However, by studying the discrete spectrum, we can optimize the predicted coupling rates, as we do in Section 3.6.4.

4 Cavity QED using two-dimensional atom arrays

The content of this chapter is based on

[2] D. Castells-Graells, J. I. Cirac, and D. S. Wild,
Cavity Quantum Electrodynamics with Atom Arrays in Free Space
arXiv preprint arXiv:2409.15434 (2024)

4.1 Motivation

Quantum networks have been a focus of research in the field of quantum optics as they hold great potential for applications in quantum communication [90, 91], quantum cryptography [92], distributed quantum computing [93, 94], quantum metrology [9, 95], and the study of exotic many-body systems [8, 96]. Photons are ideal carriers of quantum information between nodes of a quantum network as they can travel over long distances while interacting weakly with the environment. A key challenge in realizing robust and scalable quantum networks thus lies in coherently controlling the interaction between matter and light at the single-photon level. Due to the small optical cross-section of a dipole emitter and the diffraction limit, deterministic light-matter interaction is unfeasible with far-field optics in free space [11–13]. Cavity quantum electrodynamics (cavity QED) overcomes these limitations by placing the emitter inside an optical resonator [14, 34]. Although high-fidelity, deterministic light-matter interaction has been demonstrated in a variety of cavity QED setups [97–101], incorporating these systems into large networks presents a major technological challenge owing to the complexity of placing individual emitters inside high-finesse optical resonators while maintaining the coherence of both components [15, 102].

The shortcomings related to placing quantum emitters close to dielectric surfaces can be circumvented by using the collective response of ordered arrays of emitters [28, 103, 104]. For concreteness, we consider optical transitions in neutral atoms, although the approach readily applies to other types of dipole emitters. Previous works showed that a two-dimensional, ordered array of atoms with a subwavelength lattice spacing acts as a perfect reflector when the incident light is resonant with a collective excitation [29, 30, 37]. Combining two such array mirrors to form an *array cavity*, within which additional target atoms are placed, we show that a cavity QED setup can be realized with a system consisting entirely of trapped atoms in an optical lattice.

Beyond obviating the need for trappig atoms close to dielectric surfaces, the properties of atom arrays create new opportunities beyond existing cavity QED schemes. Atom array setups have been proposed to store light with high fidelity [28, 86, 105–107], modify the optical wavefront [108–110], enhance absorption [111–113], and mediate long-range interactions [1, 63, 114]. The combination of such applications with the setup presented here leads to a powerful toolbox for designing quantum networks with desirable attributes not accessible with conventional mirrors. The ability to optically trap atoms at relatively short distances can be used to explore more complex schemes within the same experimental setup, involving multiple atoms inside a cavity, or even multiple connected cavities. Another compelling feature is the ability to dynamically control the properties of atom arrays by means of external fields [115–117]. For instance, the mirrors could be rapidly switched on or off by optical control and the polarization of the optical transition could be modulated to create cavity modes with time-dependent chirality. Novel schemes could further take advantage of the motional degrees of freedom of the atoms within the framework of optomechanics [118, 119] or of the intrinsic nonlinearity of the arrays. Unlike standard nonlinear media [120, 121], atom arrays display nonlinearities at the level of few photons [45, 63, 122] or even at the single-photon level in cavity configurations [123, 124]. Finally, Rydberg states can be leveraged to realize photonic gates [38, 125–127]. Applications of the cavity setup involving Rydberg states might be of special interest, as they are highly susceptible to interfering fields from nearby surfaces [128].

4.2 Summary

In this chapter, we demonstrate the possibility of creating cavities with high cooperativities entirely from optically trapped atoms. Similar setups without atoms inside the cavity were considered in previous studies, which identified narrow resonances

in the reflection and transmission spectra due to long-lived collective excitations delocalized across the two arrays [86, 123]. By studying the dynamics of an atom inside the array cavity, we show that these resonances can be viewed as discrete cavity modes.

We find a large regime of parameters in which our setup is accurately described by a model of conventional cavity QED with a coupling strength g, cavity decay rate κ, and spontaneous emission rate γ_{3D}. Despite the similarities, the setup differs in important aspects from conventional cavity QED, arising from the narrow bandwidth over which the atom arrays reflect light. First, the array cavity only supports modes with frequencies near the resonance of the atoms that form it. Therefore, the array mirrors must be separated by a distance close to a half-integer multiple of their resonant wavelength. This is in contrast to a cavity formed by broadband mirrors, which supports modes at arbitrary separations of the mirrors. Secondly, the cavity QED parameters are modified as they are governed by the lifetime of the array atoms instead of the cavity round-trip time. Nevertheless, we show that an atom-array cavity achieves the same cooperativity as a conventional cavity QED setup with matching mirror specifications, i.e., the radius of curvature and the reflection and transmission coefficients.

An atom-array cavity presents its own challenges related to the precise positioning of the atoms. As illustrated in Fig. 4.6.5, the cooperativity saturates when the transmission of the mirrors is less than the scattering loss. For atoms pinned at locations that match the curved wavefront of the cavity mode, the loss is small and cooperativities on the order of the 10^4 can be achieved. Disorder and motion of the atoms significantly increase scattering loss. Nevertheless, cooperativities exceeding unity can be achieved with current experimental parameters. We show below that the requirement on the curved positioning of the atoms can be relaxed by subjecting a flat array to a spatially varying Stark shift.

The chapter is structured as follows. In Section 4.3, we describe our setup and discuss the fundamental differences between array and conventional mirrors. In Section 4.4, we analyze in detail the atom-array cavity and compute the cavity QED parameters g, κ, and γ_{3D}. In Section 4.5, we show how to achieve the strong-coupling regime and test the system dynamics with some cavity QED protocols. We address practical concerns, including transmission through the cavity and the effect of motion, in Section 4.6. The section further includes a scheme to achieve a high cooperativity by applying a position-dependent Stark shift to flat mirrors instead of curving them. We conclude in Section 4.7, providing an outlook on the future potential of atom-array cavities.

4.3 Setup and System Description

Our setup consists of N atoms located at positions $\mathbf{r}_i$, where $i \in \{1, 2, \dots, N\}$ labels the atoms. We assume that the atoms are subject to an external driving field with optical frequency ω_L and slowly varying, spatially dependent envelope $\mathbf{E}_0^+(\mathbf{r}, t)$, which results in the local Rabi frequencies $\Omega_i(t) = \mathbf{d}_i^* \cdot \mathbf{E}_0^+(\mathbf{r}_i, t)$. The effective non-Hermitian Hamiltonian Eq. 2.38 reads

$$\hat{H} = \sum_{i,j} \left[(\omega_i - \omega_\mathrm{L})\delta_{ij} + \Delta_{ij} - \frac{i}{2}\Gamma_{ij} \right] \hat{\sigma}_i^+ \hat{\sigma}_j^- - \sum_i \left(\Omega_i \hat{\sigma}_i^+ + \mathrm{h.c.} \right), \tag{4.1}$$

where we work in the frame that rotates with frequency ω_L. We recall that the coefficients Δ_{ij} and Γ_{ij} are Hermitian matrices that capture the coherent and dissipative interaction between atoms mediated by the electromagnetic field.

To fully describe the dynamics of the atoms, the non-Hermitian Hamiltonian in Eq. (4.1) must be supplemented by quantum jump terms [129]. In the limit of weak driving, however, we neglect them following Section 2.2.2. Moreover, in this regime, the number of excited atoms remains small, which allows us to treat the atomic spin operators, $\hat{\sigma}_i^\pm$, as bosonic operators. We work within these approximations throughout this chapter unless stated otherwise.

The atoms are organized on two parallel planar arrays forming a cavity. The two atom arrays are separated by a distance L, where each array consists of a square lattice of $N \times N$ atoms with lattice spacing a as depicted in Fig. 4.3.1. One or more additional atoms are placed inside the cavity. We refer to the atoms forming the arrays as "array atoms" and to the atoms inside the cavity as "target atoms".

We model all atoms as two-level systems with a transition dipole moment that is linearly polarized along the direction of one of the lattice vectors. We assume

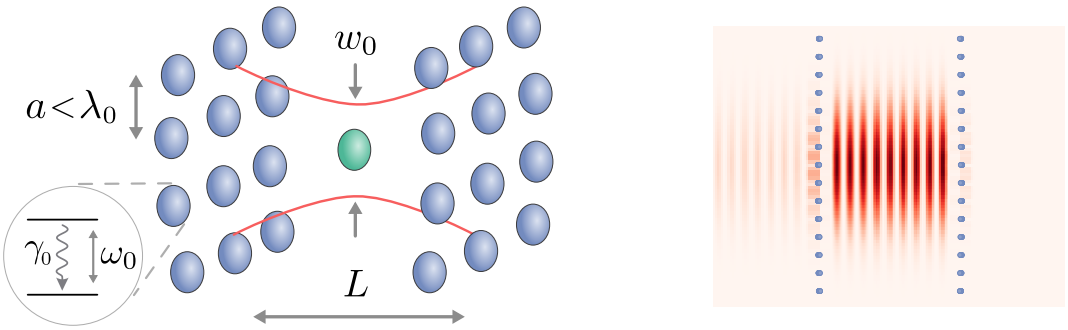

Figure 4.3.1: Cavity QED with atom arrays. (left) An atom (green circle) interacts with the field between two subwavelength arrays (blue circles). The system efficiently absorbs and emits light, rendering it a suitable node of a quantum network. (right) Spatial distribution of the steady state field intensity of an empty array cavity excited by a Gaussian beam impinging orthogonally from the left.

that the array atoms are identical with resonance frequency ω_0 and free-space decay rate γ_0. The corresponding quantities of the target atoms, denoted by ω_a and γ_a, can in general be different. In the applications considered below, the resonance frequencies ω_0 and ω_a differ by an amount proportional to γ_0 and we require $\gamma_a \ll \gamma_0$. The target and array atoms may nevertheless belong to the same species as the transition frequency and decay rate can be tuned by local dressing fields as described in Section 4.5.

The wavelength $\lambda_0 = 2\pi c/\omega_0$ is an important length scale of the system. We will neglect the difference between λ_0 and $\lambda_a = 2\pi c/\omega_a$ throughout, which is valid because $|\omega_0 - \omega_a| \ll \omega_0$. For the arrays to act as resonant mirrors without Bragg scattering at normal incidence, we require subwavelength lattice spacing, $a < \lambda_0$. We treat a as a free parameter and discuss how the cavity QED parameters depend on it. We showcase many of our results at a fixed lattice spacing of $a = 0.47\lambda_0$, which corresponds to a predicted magic wavelength for the D_2 manifold of ^{87}Rb [130]. To achieve high quality factors, it is necessary to curve the arrays such that they match the optical wavefront of a Gaussian beam with waist radius w_0. To this end, we shift the lattice atoms in the direction of the cavity axis, as detailed next.

4.3.1 Curved array mirrors

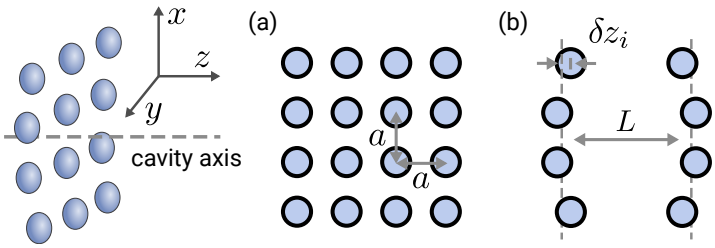

Figure 4.3.2: Schematic depiction of the displacement of the atoms to realize curved array mirrors. (a) Projection onto the $z = 0$ plane. The x and y positioning of the atoms remains a regular square lattice with spacing a. (b) $y = 0$ plane cut. The atoms are displaced in the z direction. The positions $z_i = \pm L/2 + \delta z_i$ are determined by solving Eq. (4.2).

For a cavity to support a Gaussian beamshape, the mirrors need to be curved to match the wavefront of the beam and refocus it at each reflection. To this end, we shift the position of the atoms along the z direction corresponding to the axis of the optical cavity (see Fig. 4.3.2). The position of the atoms in the $x - y$ plane remains unaltered. To determine the required displacement δz of each mirror atom, we solve the phase-matching condition,

$$k_0 z + k_0 \frac{x^2 + y^2}{2R(z)} - \psi(z) = k_0 \frac{L}{2}\,, \tag{4.2}$$

where $R(z) = (z^2 + z_\mathrm{R}^2)/z$ is the radius of curvature of the wavefront at position z and $\psi(z) = \arctan(z/z_\mathrm{R})$ is the Gouy phase of the fundamental Gaussian mode. Both quantities depend on the Rayleigh range $z_\mathrm{R} = k_0 w_0^2/2$, which is set by the wavenumber k_0 and the beam waist w_0. The left-hand-side of Eq. (4.2) corresponds to the phase of a Gaussian beam centered at the origin, which we match to the phase of a plane wave at the surface of a planar mirror of a cavity with length L on the right-hand-side. Since Eq. (4.2) is a transcendental equation, we solve for the position z_i corresponding to each lattice site (x_i, y_i) numerically. Note that the distance between the arrays on the axis becomes slightly larger than L to accommodate for the Gouy phase.

4.3.2 A LONGER ROUND-TRIP TIME

A recurrent observation in this chapter is that the cavity QED parameters are modified in comparisson with the expectation from cavity QED, as they are governed by the lifetime of the array atoms instead of the cavity round-trip time. Resonant reflection by a mirror with bandwidth Γ_0 incurs the Wigner time delay $\tau_\mathrm{delay} = 2/\Gamma_0$ [131–133]. In the parameter regime considered here, τ_delay far exceeds the propagation time $\tau_\mathrm{prop} = L/c$ of the photon traveling the distance L between the arrays. The photon only spends a fraction $\tau_\mathrm{prop}/(\tau_\mathrm{prop}+\tau_\mathrm{delay}) \approx L\Gamma_0/2c \ll 1$ of the time propagating and the number of round trips in a given time is reduced by the factor

$$\zeta = \frac{\Gamma_0 L}{2c} \tag{4.3}$$

compared to broadband mirrors. This will be an important quantity in our analysis below. Within the paraxial limit, we expect Γ_0 to be close to the decay rate of the zero momentum of an infinite array. From Eq. (2.51), we find $\Gamma_0 \approx 3\pi\gamma_0/(k_0 a)^2$ and

$$\zeta \approx \frac{3\pi}{2}\frac{1}{(k_0 a)^2}\frac{\gamma_0 L}{c}. \tag{4.4}$$

We will assume throughout that $\gamma_0 L/c \ll 1$ and $\zeta \ll 1$, which follows provided a is not deeply subwavelength. These assumptions are valid for optical dipole transitions and array cavities with lengths on the order of a few wavelengths. The condition $\gamma_0 L/c \ll 1$ indicates that retardation is negligible, which is separately required to apply the formalism of Section 2.2.

As we show in Section 4.4, it follows that κ and g^2, the latter of which is proportional to the energy density of the electromagnetic field inside the cavity, are reduced by this factor. Intriguingly, both g and κ are therefore approximately independent of the cavity length L in our setup. We highlight that the factors cancel

when computing the cooperativity $C = 4g^2/\kappa\gamma_{3D}$, which is a key figure of merit. An atom-array cavity thus achieves the same cooperativity as a conventional cavity QED setup with matching mirror specifications, i.e., the radius of curvature and the reflection and transmission coefficients.

4.4 Atom-cavity coupling

4.4.1 Cavity modes

To formalize the connection between cavity QED and the above setup, we consider the dynamics of a single target atom initialized in the excited state at time $t = 0$. The array atoms all start in the ground state. As shown in Appendix 4.A, the amplitude that the excitation is on the target atom after time t is given by

$$c_{\mathrm{a}}(t) = \frac{i}{2\pi}\int_{-\infty}^{\infty} \mathrm{d}\omega\, e^{-i\omega t}\frac{1}{\omega - \omega_{\mathrm{a}} + i\gamma_{\mathrm{a}}/2 - \Sigma_{\mathrm{a}}(\omega)}\,. \tag{4.5}$$

The function $\Sigma_{\mathrm{a}}(\omega)$, known as the self-energy, describes a frequency-dependent modification of the resonance frequency and decay rate of the target atom due to the presence of the arrays. We denote by $|i\rangle$ the state in which the atom with index i is excited and all other atoms are in the ground state. We choose $i = 0$ for the target atom and $i \in \{1, 2, \ldots, 2N^2\}$ for the array atoms. We define the $2N^2$ vector components $H_i^{\mathrm{TA}} = \langle 0|\hat{H}|i\rangle$ and $H_i^{\mathrm{AT}} = \langle i|\hat{H}|0\rangle$ and the $2N^2 \times 2N^2$ matrix $H_{ij}^{\mathrm{AA}} = \langle i|\hat{H}|j\rangle$, with i and j restricted to array atoms. The self-energy may then be written as

$$\Sigma_{\mathrm{a}}(\omega) = \mathbf{H}^{\mathrm{TA}} \cdot \left[\omega\mathbf{I} - \mathbf{H}^{\mathrm{AA}}\right]^{-1} \cdot \mathbf{H}^{\mathrm{AT}}, \tag{4.6}$$

where $\mathbf{I}$ is the $2N^2 \times 2N^2$ identity matrix.

Since the self-energy is complex, it is convenient to consider its real and imaginary parts separately. We focus in particular on the spectral function

$$A(\omega) = \gamma_{\mathrm{a}} - 2\,\mathrm{Im}[\Sigma_{\mathrm{a}}(\omega)]\,, \tag{4.7}$$

which can in certain regimes be interpreted as the modified decay rate of the target atom due to the presence of the arrays. To see this, we observe that if $\Sigma_{\mathrm{a}}(\omega)$ varies slowly, the target atom experiences the array atoms as a bath that can be treated within the Markov approximation. Formally, this corresponds to replacing the self-energy by a constant in Eq. (4.5), resulting in the exponential dependence $c_a(t) \approx \exp\{-i[\omega_a - i\gamma_a/2 + \Sigma_{\mathrm{a}}(\omega_a)]t\}$. This interpretation is valid provided that the self-energy is approximately constant over the frequency interval $\omega_a \pm |\Sigma_{\mathrm{a}}(\omega_a)|$. Because

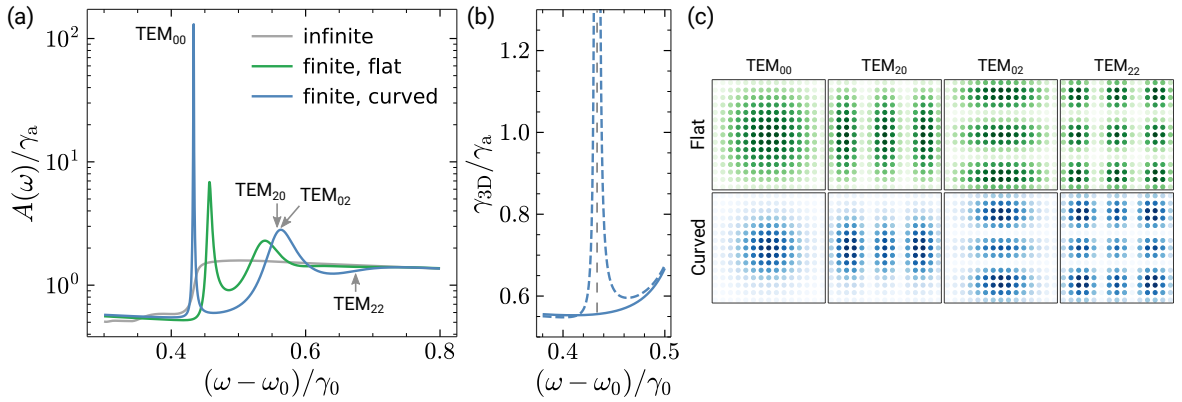

Figure 4.4.1: Spectral response of a target atom placed at the center of an array cavity. (a) Spectral function, Eq. (4.7), for a square lattice arrays with lattice spacing $a = 0.47\lambda_0$ and distance $L = 1.5\lambda_0$ between the arrays. We consider infinite arrays and finite arrays composed of $N \times N = 15 \times 15$ atoms. For the blue line, the arrays are curved to match a Gaussian beam with waist $w_0 = 2\lambda_0$ and the labels indicate the energy of the eigenmodes illustrated in (c). (b) By subtracting the contribution of the TEM_{00} mode from the spectral function close to the cavity resonance (dashed curve), we obtain a smooth background (solid curve). The value of the background at the cavity resonance can be interpreted as γ_{3D}, i.e., the modified decay rate of the target atom into free space. (c) Illustration of the four eigenmodes of $\mathbf{H}^{AA}$ with the largest contribution to the spectral function for finite arrays with the same parameters as in (a). For each atom in one of the arrays, we draw a circle whose color is determined by the absolute value of the amplitude that the atom is excited. Darker colors correspond to larger amplitudes.

$\Sigma_a(\omega)$ is proportional to γ_a, this condition can always be satisfied for smooth $\Sigma_a(\omega)$ and a sufficiently small γ_a.

In Fig. 4.4.1(a), we plot $A(\omega)$ for a target atom placed at the center of two arrays separated by $L = 1.5\lambda_0$. We first consider a pair of infinite square lattices, for which we compute the self-energy numerically by converting the sum over lattice sites into an integral over momenta [30]. The spectral function displays plateaus, where the emission rate of the target atom is either suppressed or enhanced compared to free space. The plateaus are the result of coupling to a continuum of guided modes supported by the arrays. The sharp transitions between the plateaus arise at the band edges of the dispersion relation of these modes. This behavior is in stark contrast to finite-sized arrays, for which $A(\omega)$ displays sharp resonances on top of a smooth background. Due to the nearly singular behavior of the spectral energy at these resonances, they cannot be interpreted as a simple modification of the decay rate.

The form of Eq. (4.6) indicates that the resonances arise from coupling of the target atom to individual eigenmodes of the array. Concretely, an eigenmode of $\mathbf{H}^{AA}$ with complex eigenvalue $\omega_c - i\kappa/2$ and associated left and right eigenvectors $\mathbf{v}^L$ and $\mathbf{v}^R$ contributes $g^2/(\omega - \omega_c + i\kappa/2)$ to the self-energy, where $g^2 = (\mathbf{H}^{TA} \cdot \mathbf{v}^R)(\mathbf{v}^L \cdot \mathbf{H}^{AT})$ quantifies the coupling strength between the eigenmode and the target atom. Hence,

an eigenmode with small decay rate κ and large coupling strength g gives rise to a sharp resonance of height g^2/κ. The resonance takes the same shape as the resonance found in the atom self-energy of the Jaynes-Cummings model with corresponding parameters (see Appendix 4.A for details). We can thus view the eigenmodes that lead to resonances in the self-energy as cavity modes.

To characterize the cavity modes, we numerically diagonalize the matrix $\mathbf{H}^{\mathrm{AA}}$ and compute the ratio g^2/κ for each eigenmode. The distribution of the excitation across the array according to the right eigenvector is illustrated in Fig. 4.4.1(c) for the eigenmodes with the four largest magnitudes of g^2/κ. The distributions closely resemble the profile of Hermite-Gaussian modes, TEM_{mn}. We identify the sharpest resonance in the spectral function with the fundamental TEM_{00} mode and the second largest peak with the degenerate TEM_{20} and TEM_{02} modes. The next smaller value of g^2/κ, corresponding to the TEM_{22} mode, is insufficient to give rise to a discernible resonance. We note, however, that higher-order resonances can be observed in larger arrays. Odd modes, such as TEM_{10}, do not appear in Fig. 4.4.1(a) because they do not couple to the target atom.

We observe that the frequency splitting between the TEM_{00} and TEM_{mn} modes, denoted by δ_{mn}, is on the order of γ_0. This frequency scale, set by the array atoms, is not present in a conventional cavity, where the mode splitting is instead given by $\delta_{mn}^{\mathrm{conv}} = (c/L)(m+n)\arccos(1-L/R)$. Here, $R = (L/2) + (k_0^2 w_0^4/2L)$ is the radius of curvature of the mirrors. The expression for $\delta_{mn}^{\mathrm{conv}}$ can be obtained by matching the propagation phase to the Gouy phase [134]. The transverse mode splitting in a conventional cavity is therefore proportional to the free spectral range, which is much greater than γ_0 for the range of parameters considered here. The mode splitting in the array cavity differs due to the dispersive response of the arrays. According to Eq. (2.53), reflection by one of the mirrors results in a phase shift $\phi = \arctan(2\delta_{mn}/\Gamma_0)$, where we assumed that the fundamental mode is resonant with the mirror. In the regime $\zeta \ll 1$, this phase shift is much greater than the propagation phase. We therefore replace the propagation phase in the resonance condition by ϕ to obtain

$$\delta_{mn} \approx \frac{\Gamma_0}{2} \tan\left[(m+n)\arccos\left(1-\frac{L}{R}\right)\right]. \tag{4.8}$$

For the finite, curved arrays in Fig. 4.4.1(a), this expression yields $\delta_{20} \approx 0.13\,\gamma_0$, in perfect agreement with the numerically computed splitting of the resonances in the spectral function.

We note that the above expression only applies if $\delta_{mn} \ll \Gamma_0$ since the arrays otherwise reflect only weakly and do not give rise to a cavity resonance. Moreover, there

are significant deviations from Eq. (4.8) in small arrays with little or no curvature. This is evident for the finite, flat arrays in Fig. 4.4.1(a), where the TEM_{00} and TEM_{20} modes are clearly split, although they should be degenerate according to Eq. (4.8). The observed mode splitting is due to boundary effects, which effectively localize the beam to a smaller waist. The boundaries also induce diffraction losses and thereby broaden the resonances [106].

Below, we focus on the fundamental mode, TEM_{00}, which couples most strongly to the target atom. This is justified if the target atom is tuned close to the resonance of this mode and γ_a is small enough such that off-resonant coupling to other modes is negligible. We will treat the cavity mode separately from all other eigenmodes and may therefore subtract its contribution from the self-energy to recover a smooth frequency dependence as shown in Fig. 4.4.1(b). This background value can be interpreted as the modification of the properties of the target atom by the weakly coupled eigenmodes and allows us to compute the modified decay rate γ_3D into free space. Before proceeding to applications, we quantitatively analyze the dependence of the cavity QED parameters g, κ, γ_3D, and the cooperativity C on the design parameters w_0, L, and a.

4.4.2 Cavity parameters

Coupling strength, g

As noted above, a particular eigenmode of the array with left and right eigenvector $\mathbf{v}^\mathrm{L}$ and $\mathbf{v}^\mathrm{R}$ couples to the target atom with strength $g = \sqrt{(\mathbf{H}^\mathrm{TA} \cdot \mathbf{v}^\mathrm{R})(\mathbf{v}^\mathrm{L} \cdot \mathbf{H}^\mathrm{AT})}$. Since the Hamiltonian is non-Hermitian, g will in general be complex. Its imaginary part captures the fact that the field emitted by the target atom and the eigenmode of the array interfere, which leads to enhanced or suppressed collective emission. However, in the regimes discussed in this chapter, the imaginary part of g is much smaller than its real part. We will therefore neglect the imaginary part throughout.

In Fig. 4.4.2, we show the coupling strength g computed in this way as a function of the lattice spacing a, the cavity length L, and the beam waist w_0. These parameters determine the radius of curvature of the array mirrors via the relation $R = (L/2) + (k_0^2 w_0^4 / 2L)$. We observe that g is inversely proportional to w_0 and a but largely independent of L. To interpret this result, we compare it to the case of a conventional cavity. According to Section 2.4.3, the maximum coupling strength in a conventional cavity can be written as

$$g^\mathrm{conv} = \sqrt{\frac{3\pi}{2} \frac{\gamma_\mathrm{a} \omega_0}{k_0^3 V}}, \tag{4.9}$$

where the mode volume for a Gaussian beam is given by $V = \pi w_0^2 L/4$ [135]. Al-

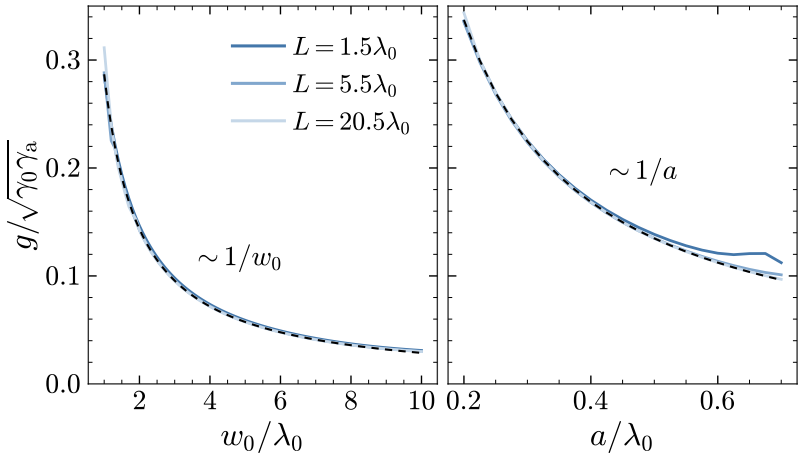

Figure 4.4.2: Coupling strength, g, between the fundamental mode of an array cavity and a target atom placed at the field maximum. The left panel shows the dependence on the beam waist w_0, which is determined by the curvature of the mirrors, for a fixed lattice spacing $a = 0.47\lambda_0$ and array size $N \times N = 60 \times 60$. In the right panel, we vary a with $w_0 = 2\lambda_0$ fixed and $N \times N = 45 \times 45$. The three curves for different separations of the array mirrors (legend in the left panel) lie on top of each other except for the largest values of a. The dashed lines represent the analytical prediction, Eq. (4.10).

though this expression correctly captures the dependence of g on w_0, it is clearly inconsistent with the observed dependence on L and a.

Even though we computed the value of g from the spin model in Eq. (4.1), its physical origin lies in the coupling of the target atom to the electric field of a single excitation in the cavity mode. The reason for the discrepancy can then be understood from the fact that Eq. (4.9) does not include the time delay τ_{delay} in the reflection caused by the finite bandwidth of the array mirrors. Due to the delay, the field tends to localize close to the arrays and we expect that the energy density at the center of the cavity will be suppressed by the factor ζ. Since the target atom couples to the electric field, which is proportional to the square root of the energy density, the argument suggests that the coupling strength in an array cavity is given by

$$g \approx \sqrt{\zeta} \cdot g^{\text{conv}} \approx \frac{\sqrt{9\pi\gamma_a\gamma_0}}{k_0^2 w_0 a}\,, \tag{4.10}$$

where we used Eq. (4.4). This expression correctly captures the dependence on w_0, L, and a observed in Fig. 4.4.2. It is indeed in excellent quantitative agreement over a wide range of parameters as shown by the black dashed curve. The only significant deviations occur for large values of a/λ_0 and small L, predominantly $L = 1.5\lambda_0$, which we attribute to near-field coupling between the target atom and the arrays.

CAVITY DECAY RATE, κ

Following our discussion of the self-energy, the cavity decay rate κ is determined by the imaginary part of the eigenvalue of the non-Hermitian Hamiltonian $\mathbf{H}^{\mathrm{AA}}$ belonging to the array eigenmode that is responsible for the cavity resonance. In Fig. 4.4.3 we show the cavity linewidth as a function of w_0 and L obtained by numerically diagonalizing $\mathbf{H}^{\mathrm{AA}}$ for an array cavity of size $N \times N = 60 \times 60$. We observe the smallest decay rate when the beam waist is a few wavelengths, at which point $\kappa < 10^{-6}\gamma_0$ can be achieved.

To explain the qualitative features in Fig. 4.4.3, we again appeal to a physical picture involving the electric field, despite it having been traced out in our calculation. In a conventional cavity comprising identical mirrors with reflection coefficient $\mathcal{R}$, a fraction $1-\mathcal{R}$ of the energy is lost at each reflection, leading to the cavity decay rate $\kappa^{\mathrm{conv}} = c(1-\mathcal{R})/L$. For the array mirrors, we have to take into account that the reflection time delay is much greater than the round-trip time. Therefore, we expect

$$\kappa \approx \zeta\kappa^{\mathrm{conv}} = (1-\mathcal{R})\frac{\Gamma_0}{2}\,. \tag{4.11}$$

Since Γ_0 is approximately independent of w_0 and L, the dependence of κ on these parameters is governed by the reflection coefficient of a single mirror. We outline the pertinent features of the reflection coefficient below, while postponing a more detailed analysis to the discussion of the cavity transmission in Section 4.6.1.

If the beam waist is large, reflection is imperfect because the arrays do not capture the entire beam. This effect was analyzed in detail in Ref. [106] for a Gaussian beam focused onto a flat array, where it reduces the reflection coefficient to $1-\mathcal{R} \approx \mathrm{Erf}^2(Na/\sqrt{2}w_0)$. The expression qualitatively captures the increase in κ at large values of w_0 (see dashed-dotted line Fig. 4.4.3). There are however significant quantitative deviations, that can be attributed to the dependence of diffraction losses on the separation between the mirrors, as diffracted light spreads out over longer distances between reflections [136], and to the modification of the cavity mode due to boundary effects, as discussed in relation to Fig. 4.4.1(c). We note that the finite size of the arrays also leads to losses at small values of w_0, especially when L is large, owing to the strong divergence of the cavity mode.

In the regime where the arrays are sufficently large to contain the cavity mode, we observe that κ is roughly proportional to $1/w_0^4$ (dashed line in Fig. 4.4.3). This scaling was shown in Ref. [106] to be the result of higher in-plane momentum components of the Gaussian beam, which are imperfectly reflected due to the quadratic dispersion relation of the eigenmodes of the array. The value of κ is independent of the size of the array in this regime. We conclude that to minimize κ, one should

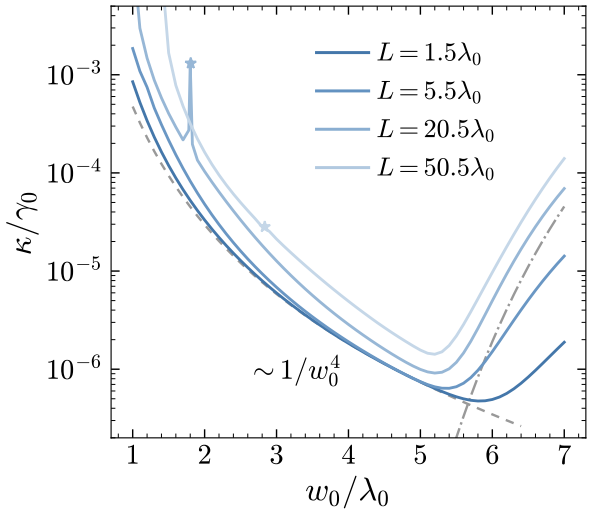

Figure 4.4.3: Cavity decay rate, κ, for a target atom placed at the maximum of intensity as a function of the beam waist w_0, determined by the curvature of the mirrors, for a fixed lattice spacing $a = 0.47\lambda_0$ and array size $N \times N = 60 \times 60$. We include four different values of L (legend in the central panel). The dashed-dotted line represents the prediction of Eq. (4.11) using an estimate for the portion of the beam that extends beyond the mirrors, $1 - \mathcal{R} \approx \text{Erf}^2(Na/\sqrt{2}w_0)$. The dashed line shows the scaling $\kappa \sim 1/w_0^4$ arising from nonzero in-plane momentum components. The stars indicate the values of w_0 for which the cavity is in the confocal configuration, $R = L$. At this point, the fundamental mode becomes degenerate with higher-order TEM_{mn} modes, which may lead to increased loss.

choose the largest possible value of w_0 for which losses due to the finite size of the array are negligible. We note that other decay channels may significantly modify the dependence of κ on w_0. In Section 4.6.1, we consider enhanced cavity decay by detuning the cavity resonance from the array mirrors, while in Section 4.6.2 we explore the detrimental contributions due to motion and disorder.

Decay rate of the target atom, γ_{3D}

The presence of the array atoms modify the decay rate of the target atom. As discussed in the context of Fig. 4.4.1(b), this decay rate, denoted by γ_{3D}, can be computed by evaluating the spectral function after subtracting the contribution from the cavity mode. The resulting values are shown in Fig. 4.4.4 as a function of w_0 and L.

For weakly curved mirrors (large w_0), γ_{3D} is close to the decay rate in free space, γ_a, when the separation between the mirrors is much greater than the wavelength. The decay rate is reduced by about 50% for a short cavity with $L = 1.5\lambda_0$, which can be interpreted as the suppression of free-space decay channels due to the modification of the electromagnetic environment caused by the mirror atoms. This effect tends to be enhanced as the cavity mode becomes more tightly focused. However, γ_{3D} stops being a smooth function for smaller w_0 and may even take unphysical nega-

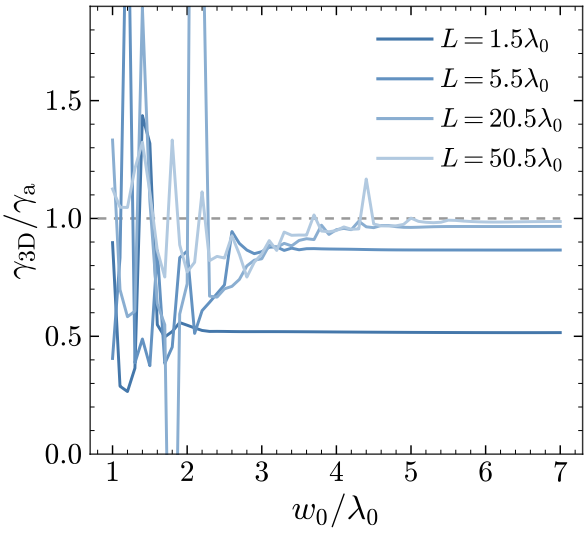

Figure 4.4.4: Decay rate of the target atom, γ_{3D}, for a target atom placed at the maximum of intensity. Here we use the same parameters as in Fig. 4.4.3. The values of γ_{3D} do not follow a smooth curve at small beam waists due to the presence of nearby cavity modes [see Eq. (4.8)]. In this regime, γ_{3D} cannot be simply interpreted as a decay rate.

tive values. We attribute this behavior to weak resonances with higher-order cavity modes that, according to Eq. (4.8), can become degenerate with the fundamental mode. In such cases, the single-mode cavity assumption is not justified, and our method to compute γ_{3D} is not valid. These resonances also contribute to increased losses in Fig. 4.4.3.

Cooperativity

We now combine the results of the preceding sections to compute the cooperativity $C = 4g^2/\kappa\gamma_{3D}$. From Eqs. (4.10) and (4.11), we obtain

$$C \approx \frac{6}{\pi^2}\frac{\gamma_a}{\gamma_{3D}}\frac{1}{1-\mathcal{R}}\left(\frac{\lambda_0}{w_0}\right)^2 . \tag{4.12}$$

We highlight that this expression also holds for conventional cavities because the factors of ζ in the expression for g and κ cancel. This reflects the fact that the cooperativity is independent of the round-trip time or, in the case of the array cavity, the lifetime of the mirror eigenstate associated with the cavity mode. Since the resonant cross section of the target atom is proportional to λ_0^2, the cooperativity has the appealing physical interpretation as the number of times that a cavity photon interacts with the atom during its lifetime [135]. For a given reflection coefficient and curvature of the mirrors, we thus expect an array cavity and a conventional cavity to have approximately the same cooperativity. In practice, deviations may arise because the different setups lead to different values of γ_{3D}. This result is compatible

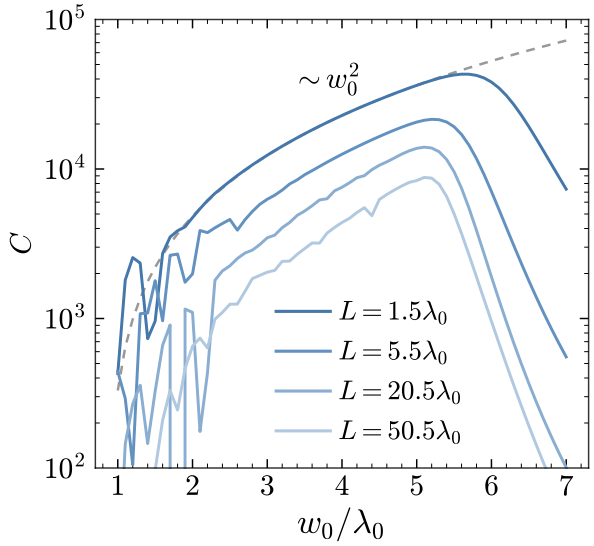

Figure 4.4.5: Cooperativity, C, for a target atom placed at the maximum of intensity. Here we use the same parameters as in Fig. 4.4.3. The cooperativity follows the relation $C \sim w_0^2$ (dashed curve) up until the reflection coefficient is significantly affected by the finite size of the mirrors.

with the observation that, in the paraxial regime, the reflection coefficient of planar atom arrays determines the efficiency of various quantum tasks [137].

As shown in Fig. 4.4.5, the cooperativity reaches a maximum at the largest beam waist that is supported with low loss by the finite-sized arrays. For the parameters considered here, values exceeding $C = 10^4$ can be reached. Leading up to the maximum, the cooperativity is approximately proportional to w_0^2. This follows from the dependence $1 - \mathcal{R} \propto 1/w_0^4$, observed in Fig. 4.4.3, combined with the $1/w_0^2$ factor in Eq. (4.12). This result could be extrapolated to larger w_0 by increasing the size of the arrays to prevent the detrimental increase in κ. However, the splitting between the fundamental and higher TEM$_{mn}$ modes will decrease for larger w_0 [see Eq. (4.8)], which may render the single-mode approximation invalid. Moreover, if other decay channels are present, $\mathcal{R}$ may become independent of w_0. In this case, we recover the more conventional scaling $C \propto 1/w_0^2$ and the cooperativity is maximized at the smallest achievable beam waist.

4.5 Strong-coupling regime

Although the cooperativity is an important figure of merit, it does not capture the relative magnitudes of g, κ, and γ_{3D}, which qualitatively impact the dynamics. The strong-coupling regime, where $g \gg \kappa, \gamma_{3D}$, is of particular interest as the target atom and the cavity can coherently exchange excitations. Using the results of the previous section, we find that the strong-coupling conditions are equivalent to

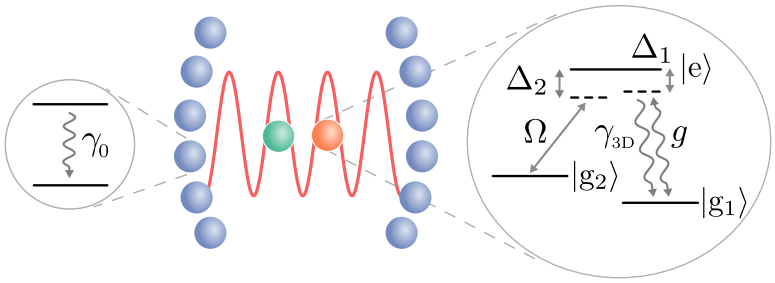

Figure 4.5.1: To achieve strong coupling, a three-level Λ-system is introduced for the target atoms. Under a classical drive with large detuning Δ_2, the excited state $|e\rangle$ can be eliminated. The resulting effective coupling of the two-level system $\{|g_1\rangle, |g_2\rangle\}$ to the cavity is controlled by the strength Ω of the drive. The array atoms remain unchanged.

$\gamma_0 \gg \gamma_a \gg (1-\mathcal{R})^2\gamma_0$, where we assumed that $\gamma_{3D} \approx \gamma_a$, $w_0 \approx a \approx \lambda_0$, and ignored numerical prefactors. The strong-coupling regime is thus accessible for a sufficiently large reflection coefficient $\mathcal{R}$ by a suitable choice of γ_a. By varying γ_a it is also possible to reach different regimes. For instance, the Purcell regime, also known as the bad-cavity regime, requires that $\gamma_a \ll (1-\mathcal{R})^2\gamma_0$.

In practice, it may be challenging to identify a transition that satisfies the requirements on γ_a and that is at the same time resonant with the cavity mode. A common approach to overcome this limitation is to employ a Raman scheme, which enables continuous tuning of the effective transition dipole of the target atom [1, 39–41]. This scheme requires that each target atom contains a Λ-system, comprising two long-lived states $|g_1\rangle$ and $|g_2\rangle$ which are both connected to an excited state $|e\rangle$ via a dipole transition [see Fig. 4.5.1]. The cavity couples to the transition $|g_1\rangle \leftrightarrow |e\rangle$ with coupling strength g. The decay rate of the excited state is given by γ_{3D}, as before. Crucially, we assume that the detuning Δ_1 between this transition and the cavity can be varied, which may be realized in practice using light shifts or a static field. A classical field drives the transition $|g_2\rangle \leftrightarrow |e\rangle$ with Rabi frequency Ω and detuning Δ_2 to complete the Raman scheme.

This arrangement leads to a cavity-mediated two-photon transition between $|g_1\rangle$ and $|g_2\rangle$, which is resonant when $\Delta_1 = \Delta_2$, ignoring small corrections due to Stark shifts. As shown in App. 4.B, the excited state can be adiabatically eliminated if g and Ω are much smaller than the detunings. The two ground states then form an effective two-level system whose transition dipole is reduced compared to the dipole moment of the $|g_1\rangle \leftrightarrow |e\rangle$ transition by a factor $\epsilon \approx \Omega/\Delta_1$, where we assumed that $|\Delta_1| \gg \gamma_{3D}$. The effective coupling strength and decay rate are thus given by $g_{\text{eff}} = \epsilon g$ and $\gamma_{\text{eff}} = \epsilon^2\gamma_{3D}$. Since $g_{\text{eff}}^2/\gamma_{\text{eff}} = g^2/\gamma_{3D}$, the effective cooperativity for the Raman transition $|g_1\rangle \leftrightarrow |g_2\rangle$ is the same as for the transition to which the cavity couples. We show in App. 4.B that this conclusion in fact relies on the stronger condition $|\Delta_1| \gg \sqrt{C}\gamma_{3D}$, which is needed to suppress additional decoherence caused by the

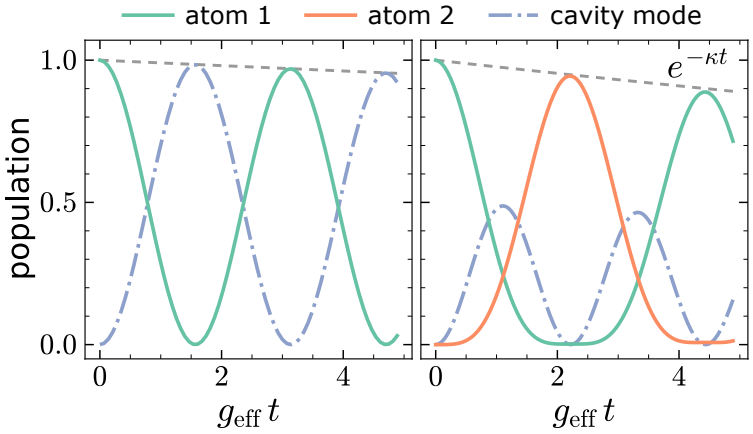

Figure 4.5.2: Cavity QED dynamics in the strong coupling regime. The left panel shows vacuum Rabi oscillations of a target atom placed at the maximum of field intensity of an array cavity with $a = 0.47\lambda_0$, $L = 1.5\lambda_0$, $w_0 = 5.5\lambda_0$, and $N \times N = 60 \times 60$. The right panel shows population exchange between two target atoms placed at the two adjacent field maxima near the center of a cavity with $a = 0.47\lambda_0$, $L = 4\lambda_0$, $w_0 = 3\lambda_0$ and $N \times N = 45 \times 45$. The setups correspond to cooperativities $C = 4.3 \times 10^4$ and $C = 7.1 \times 10^3$, respectively. We choose a large detuning $\Delta_2 = 500\gamma_a$ and set $\Delta_1 \approx \Delta_2$, where a small difference between the detunings corrects for Stark shifts in order to satisfy the two-photon resonance condition. In both panels, one of the atoms is initialized in the state $|g_2\rangle$ before the system is evolved without approximations under the non-Hermitian Hamiltonian including the Λ-systems and all array atoms. We obtain the displayed cavity population by projecting the array atoms on the corresponding eigenstate of the $\mathbf{H}^{\text{AA}}$. The population of all orthogonal states is negligible.

Raman scheme. Provided that this condition is met, we can tune the ratio $g_{\text{eff}}/\gamma_{\text{eff}}$ by adjusting ϵ while keeping the cooperativity constant. The scheme thus enables access to the strong-coupling regime without having to tune the value of γ_a.

To demonstrate the effectiveness of this approach, we consider vacuum Rabi oscillations of a single atom placed at the center of an array cavity. We choose identical decay rates for the excited states of the array atoms and the target atom, i.e., $\gamma_0 = \gamma_a$. This corresponds to the practically relevant scenario where all atoms are identical. The fidelity of vacuum Rabi oscillations is maximized when the effective decay rate of the target atom equals the decay rate of the cavity [39]. This can be achieved using the Raman scheme by setting $\Omega/\Delta_1 = \sqrt{\kappa/\gamma_{3D}}$.

In Fig. 4.5.2(b,left), we show the oscillations for an array cavity with cooperativity $C = 4.3 \times 10^4$. We highlight that we did not perform an approximate adiabatic elimination but instead included the full Λ-system describing the target atom in the calculation. The target atom is prepared in the state $|g_2\rangle$ at time $t = 0$ while the array atoms all start in the ground state. The excitation is transferred to the cavity mode after the time $t = \pi/2g_{\text{eff}}$. The vacuum Rabi oscillations, however, decay with an envelope $\exp(-\kappa t)$, which leads to the transfer fidelity $F = \exp\left(-\pi/\sqrt{C}\right)$, where we used the fact that κ is equal to the effective free-space decay rate of the target atom.

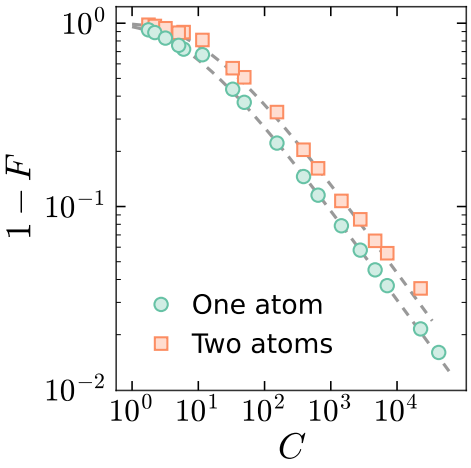

Figure 4.5.3: Transfer fidelity as a function of the cooperativity for a range of parameters a, L and w_0, including flat mirrors, and the experimentally relevant scenarios discussed in Section 4.6. The fidelity agrees well with the analytical predictions shown as dashed lines. We use $\Delta_2 = 500\gamma_a$ for all setups, although smaller values would suffice for most points.

The Raman scheme can be readily extended to multiple target atoms. In Fig. 4.5.2(right), we plot the excitation probabilities of the $|g_2\rangle$ state of two target atoms placed at adjacent antinodes close to the center of the array cavity. One of the target atoms is initialized in the state $|g_2\rangle$, whereas the other target atom is prepared in $|g_1\rangle$ and the array atoms start in the ground state. The excitation is exchanged between the two atoms after a time $t = \pi/\sqrt{2}g_{\text{eff}}$. This population exchange can be viewed as the consequence of a complete vacuum Rabi oscillation of the bright state $(|g_2\rangle|g_1\rangle + |g_1\rangle|g_2\rangle)/\sqrt{2}$, which couples to the cavity with enhanced Rabi frequency $\sqrt{2}g_{\text{eff}}$. The dark mode $(|g_2\rangle|g_1\rangle - |g_1\rangle|g_2\rangle)/\sqrt{2}$ is decoupled from the cavity and evolves trivially. As above, the oscillations decay at $\exp(-\kappa t)$, which results in the fidelity $F = \exp\left(-\pi\sqrt{2/C}\right)$ for the population transfer from one target atom to the other.

We repeated the above computations for different configurations of the array cavities. The resulting fidelities for population exchange is plotted in Fig. 4.5.3 as a function of the cooperativity, which we compute independently for each array cavity. The excellent agreement of the fidelities from the dynamics with the theoretical prediction based on the cooperativity confirms that array cavities can be accurately described by conventional cavity QED parameters. We highlight that our setup could potentially also realize protocols with a more favorable dependence of the fidelity on the cooperativity [138].

4.6 Practical considerations

4.6.1 Cavity transmission

We have focused so far on the internal dynamics of the array cavity and the target atom. In this section, we extend our analysis to include the incident and scattered fields, which are of great relevance for many applications in, e.g., quantum communication.

To compute the transmission and reflection coefficient of an array, we drive the array with a field $\mathbf{E}_0^+$ and reconstruct the total field using the input-output formula in Eq. (2.27). When discussing transmission and reflection of the mirrors of a cavity, it is important that the reflected light beam retains its spatial profile. For experimental realizations, it is also desirable that the transmitted beam is in some target collimated mode. Therefore, to distinguish between transmission (reflection) and scattering into arbitrary directions, we project the total field onto a detection mode $\mathbf{E}_{\text{det}}^+(\mathbf{r})$ ($\mathbf{E}_{\text{det}}^-(\mathbf{r})$). Following a similar approach to previous works [106, 123] and working within the paraxial approximation, we obtain the transmission and reflection coefficients

$$t = \int \mathrm{d}x\,\mathrm{d}y\,\mathbf{E}_{\text{det}}^-(\mathbf{r})\cdot\mathbf{E}_0^+(\mathbf{r}) + \frac{i}{2k_0}\frac{\omega_0^2}{\epsilon_0 c^2}\sum_i \mathbf{E}_{\text{det}}^-(\mathbf{r}_i)\cdot\mathbf{d}_i\,\langle\hat{\sigma}_i^-\rangle \tag{4.13}$$

$$r = \frac{i}{2k_0}\frac{\omega_0^2}{\epsilon_0 c^2}\sum_i \mathbf{E}_{\text{det}}^+(\mathbf{r}_i)\cdot\mathbf{d}_i\,\langle\hat{\sigma}_i^-\rangle \tag{4.14}$$

where the input and detection fields are normalized such that $\int \mathrm{d}x\,\mathrm{d}y\,\mathbf{E}_\alpha^-(\mathbf{r})\cdot\mathbf{E}_\alpha^+(\mathbf{r}) = 1$. For both input field and detection mode, we use the same Gaussian beam

$$\mathbf{E}_{\text{G}}^+(\mathbf{r}) = \mathbf{e}_x\sqrt{\frac{2}{\pi}}\frac{1}{w(z)}\exp\left(-\frac{x^2+y^2}{w(z)^2}\right)\times\exp\left[-i\left(k_0 z + k_0\frac{x^2+y^2}{2R(z)} - \psi(z)\right)\right], \tag{4.15}$$

with a linear polarization aligned with the atom dipoles. The beam waist w_0 is the same as the waist chosen to determine the curvature of the array mirrors. The quantities $R(z)$ and $\psi(z)$ are as defined in Section 4.3.1 and $w(z) = w_0\sqrt{1+(2z/k_0 w_0^2)^2}$.

For $\langle\hat{\sigma}_i^-\rangle$, we use the steady state solution of the internal dynamics, $\langle\dot{\hat{\sigma}}_i^-\rangle = 0$. Assuming a weak drive, such that saturation of the atoms is negligible, the Heisenberg equations of motion from the Hamiltonian Eq. (4.1) read

$$\langle\dot{\boldsymbol{\sigma}}^-(t)\rangle = -i\,\mathbf{h}\cdot\boldsymbol{\sigma}^-(t) + i\,\boldsymbol{\Omega}\,, \tag{4.16}$$

where we have written the Hamiltonian in matrix form, $\hat{H} = \boldsymbol{\sigma}^+\cdot\mathbf{h}\cdot\boldsymbol{\sigma}^- - (\boldsymbol{\Omega}\cdot\boldsymbol{\sigma}^+ + \text{h.c.})$.

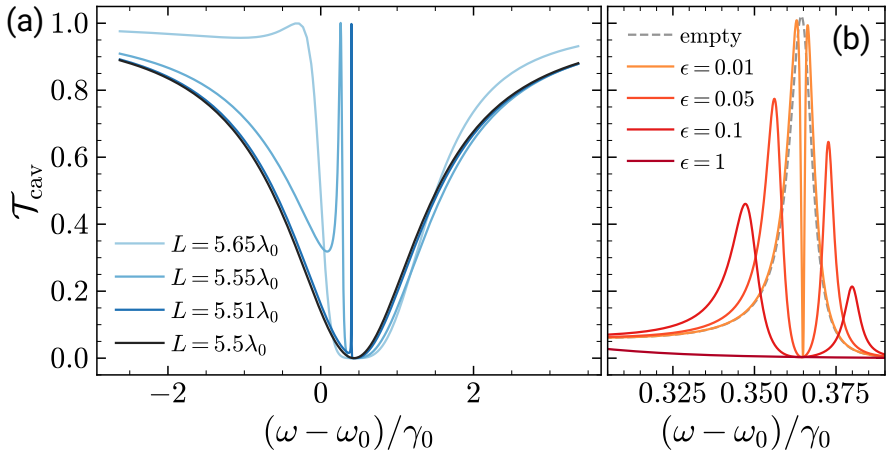

Figure 4.6.1: Transmission spectrum of array cavities probed with a Gaussian beam whose wavefront matches the curvature of the arrays. (a) Transmission through an empty cavity with $a = 0.47\lambda_0$, $w_0 = 4\lambda_0$, $N \times N = 40 \times 40$, and varying values of L (see legend). (b) Transmission through a cavity with one target atom at its center. The cavity parameters are $a = 0.47\lambda_0$, $w_0 = 1.8\lambda_0$, $L = 2.52\lambda_0$, and $N \times N = 20 \times 20$. We employ the Raman scheme described in Section 4.5 to vary the linewidth of the target atom as $\gamma_{\text{eff}} = \epsilon^2\gamma_{\text{a}}$, which enables us to smoothly interpolate between different cavity regimes. The two-photon resonance condition is always satisfied. The average height of the transmission peaks is approximately $\kappa^2/(\kappa + \gamma_{\text{eff}})^2$ in the strong coupling regime [139].

The steady state solution is, thus,

$$\boldsymbol{\sigma}^- = \mathbf{h}^{-1} \cdot \boldsymbol{\Omega}\,. \tag{4.17}$$

We recall that $\Omega_i = \mathbf{d}_i^* \cdot \mathbf{E}_0^+(\mathbf{r}_i)$.

In Fig. 4.6.1(a), we show the transmission spectrum of a Gaussian probe beam impinging on an array cavity for different values of the cavity length, L. The waist of the Gaussian beam is matched to the curvature of the arrays. We evaluate the intensity transmission coefficient, $\mathcal{T}_{\text{cav}}$, and reflection coefficient, $\mathcal{R}_{\text{cav}}$, by projecting the scattered field onto the same Gaussian mode as detailed above. The cavity transmission shows a Lorentzian dip of width $\sim \Gamma_0$, which arises from the reflection resonance of the individual mirrors. In addition, there is a cavity-like resonance, whose width and location depends sensitively on the cavity length.

As discussed in [110, 123], the transmission spectrum is accurately described by the Fabry-Pérot formula $\mathcal{T}_{\text{cav}}(\omega) = \left|t(\omega)^2/[1 - r(\omega)^2 e^{2i\omega L/c}]\right|^2$, where $r(\omega)$ and $t(\omega)$ are the amplitude reflection and transmission coefficients of a single array mirror. The frequency of the cavity resonance is determined by the interplay of the propagation phase, which depends on the cavity length, and the frequency-dependent phase of $r(\omega)$. When L is an integer multiple of $\lambda_0/2$, the cavity resonance occurs at the center of the resonance of a single mirror. There is no discernible transmission

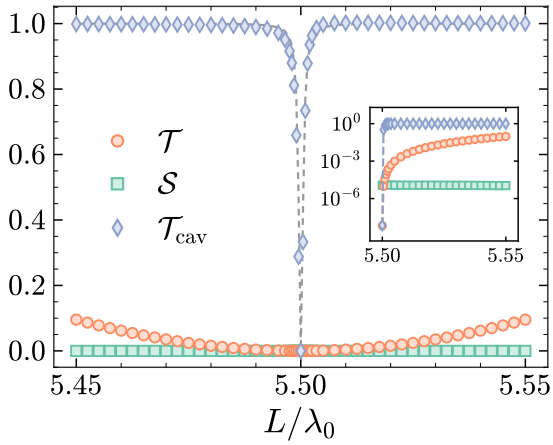

Figure 4.6.2: Dependence of the transmission, $\mathcal{T}$, and scattering loss, $\mathcal{S}$, of a single mirror at a frequency shifted by $\tan(k_0 L)\Gamma_0/2$ from the mirror resonance on the separation between the array mirrors. The shift corresponds to the location of the cavity transmission peak. We show the results for arrays with the same parameters as in Fig. 4.6.1(a). We also show the height of the cavity transmission peak (blue diamonds) and compare it to the expectation for a conventional cavity, $\mathcal{T}_{\text{cav}} = \mathcal{T}/(\mathcal{T}+\mathcal{S})$ (dashed curve). The inset shows the same data in semi-logarithmic scale.

peak in Fig. 4.6.1(a) for this case because the transmission $t(\omega)$ is small compared to scattering losses (see below). As we vary L, the cavity resonance moves away from the resonance of the mirror and consequently the relevant value of $t(\omega)$ increases. This causes the cavity resonance to broaden and to become clearly visible in transmission. We note that the transmission spectrum can alternatively be viewed as the result of interference between bright and dark modes corresponding to in-phase and out-of-phase excitation of the two mirrors [86, 133].

The presence of a target atom can strongly modify the transmission spectrum. In Fig. 4.6.1(b), we show the transmission of an array cavity with a target atom placed at the center. We take $\gamma_{\text{a}} = \gamma_0$ and tune the linewidth of the target atom using a Raman transition as described in Section 4.5. The single-photon detuning is again assumed to be large, and the cavity is resonant with the two-photon transition. For $\epsilon \approx 1$, we have $\epsilon^2\gamma_{\text{3D}} > \epsilon g > \kappa$. In this regime, the target atom has a large absorption, resulting in the suppression of the cavity transmission. For smaller values of ϵ, we access the strong coupling regime, where two peaks separated by the vacuum Rabi splitting $2\epsilon g$ can be resolved. In all regimes, the presence of the target atom suppresses the transmission at the cavity resonance by a factor $1/(C+1)^2$, which can be used to realize quantum gates between photons and the target atom [98].

Transmission vs. scattering loss

The maximum transmission through the cavity is limited by scattering into modes with little spatial structure. For a single mirror, we define $\mathcal{R}$ and $\mathcal{T}$ as the intensity reflection and transmission coefficients for a single collimated mode, which can be interfaced with conventional far-field optics. We always project onto the Gaussian beam determined by the length of the cavity and the curvature of the array mirror. The scattering loss coefficient is given by $\mathcal{S} = 1 - \mathcal{R} - \mathcal{T}$. To compute the transmission through the cavity, these coefficients must be evaluated at the cavity resonance.

As shown in Fig. 4.6.2, the scattering loss $\mathcal{S}$ is approximately independent of the resonance frequency determined by the cavity length. By contrast, the transmission coefficient satisfies $\mathcal{T} \approx \mathcal{T}_0 + (k_0 \delta L)^2$, where δL is the difference of the cavity length from the nearest integer multiple of $\lambda_0/2$, assuming $k_0 \delta L \ll 1$. This follows from the fact that $\mathcal{T}$ is approximately a Lorentzian function of frequency with width Γ_0 and that the cavity resonance is shifted from the resonance of the mirror by $\tan(k_0 \delta L)\Gamma_0/2$ [133]. Just as for a conventional cavity, we expect the maximum transmission at the cavity resonance to be given by $\mathcal{T}_{\text{cav}} = \mathcal{T}/(\mathcal{T} + \mathcal{S})$. This expression, indicated by the dashed line in Fig. 4.6.2, is indeed in excellent agreement with the data for array cavities of differenth lengths. Cavity transmission is strongly suppressed at $\delta L = 0$ because $\mathcal{S} \gg \mathcal{T}_0$, i.e., the scattering losses are much greater than transmission through the array mirror.

For many purposes, it is useful to distinguish between cavity decay due to transmission and due to loss. Following Section 4.4.2, the corresponding cavity decay rates are given by $\kappa_{\text{out}} = \mathcal{T}\,\Gamma_0/2$ and $\kappa_{\text{loss}} = \mathcal{S}\,\Gamma_0/2$. From their sum, we recover the total cavity decay rate in agreement with Eq. (4.11). The nonzero value of κ_{loss} explains the saturation in the scaling of the cooperativity at small $\mathcal{T}$ in Fig. 4.6.5. Figure 4.6.3(a) shows that this approach of computing the cavity decay rate using the reflection coefficient of a single mirror agrees well with the value of κ obtained from the imaginary part of the eigenvalue of $\mathbf{H}^{\text{AA}}$ corresponding to the cavity eigenmode. The only significant deviation occurs close to $\delta L = 0$, where the values of κ obtained from the mirror properties are an overestimate. We attribute this discrepancy to the profile of the cavity mode, which notably differs at those cavity lengths from the Gaussian beam used to probe the reflectivity of the mirrors.

The mismatch between the cavity mode and a Gaussian mode is evident in Fig. 4.6.3(b), where we show the far-field emission from the cavity eigenstate. For this, we compute the emitted field using Eq. (2.27), and evaluate the field intensity $\langle \mathbf{E}^-(\mathbf{r})\mathbf{E}^+(\mathbf{r})\rangle$, using that in the linear, unsaturated, regime $\langle \mathbf{E}^-(\mathbf{r})\mathbf{E}^+(\mathbf{r})\rangle \approx \langle \mathbf{E}^-(\mathbf{r})\rangle \langle \mathbf{E}^+(\mathbf{r})\rangle$. The emission profile matches the Gaussian mode set by the cavity length and the curvature of the mirrors for sufficiently large δL. At $\delta L = 0$, however,

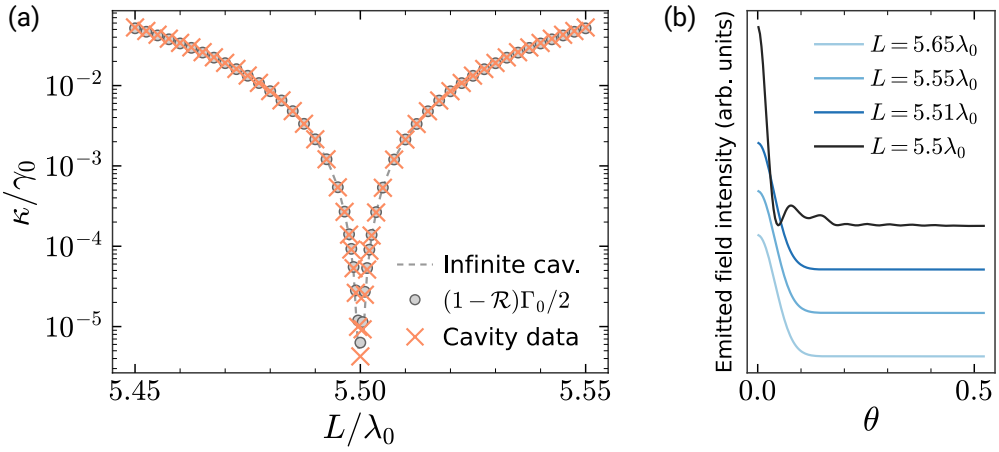

Figure 4.6.3: (a) Comparison between the cavity decay rate computed as in Section 4.4.2 (orange crosses) and the prediction of Eq. (4.11) using the reflection coefficient of a single mirror at the cavity resonance frequency (gray circles). Here, we show the results for arrays with the same parameters as in Fig. 4.6.1(a). We also show the analytical prediction $\kappa \approx (k_0\delta L)^2\Gamma_0/2$ (dashed curve) derived for infinite arrays whose length differs by a small amount from an integer multiple of $\lambda_0/2$. (b) Far-field electric field intensity emitted by the cavity eigenstate as a function of the polar angle, θ, and averaged over the azimuthal angle. The data have been rescaled and shifted for illustrative purposes. The emission pattern deviates significantly from a Gaussian at $L = 5.5\lambda_0$, where the cavity resonance coincides with the resonance of the array mirrors and transmission through the mirrors is strongly suppressed.

the emission pattern is distinctly non-Gaussian. Nevertheless, the emitted field remains collimated within a small solid angle, thereby allowing for efficient detection.

4.6.2 Motion and disorder

So far, we have considered the ideal case of point dipoles in a perfectly ordered lattice. For a realistic prediction, however, we need to include position fluctuations, which persist even in the motional ground state of a trapping potential. Motion deteriorates the properties of the array mirrors, as experimentally observed in Ref. [37], because the near-perfect reflection relies on the collective interplay of dipole–dipole interactions, which depend strongly on the relative positions of the atoms. Although a full quantum treatment of atomic motion is computationally prohibitive due to the many atoms involved, we can estimate the impact of motion on the cavity parameters by considering two extreme regimes distinguished by the speed of the motion compared to the characteristic time scale of the internal dynamics [68].

In the *frozen-motion regime*, we assume that the positions of the atoms fluctuate much more slowly than the slowest internal dynamics. Assuming that the atoms are located in harmonic traps with trapping frequency ν_T, this corresponds to the condition $\nu_T \ll \min\{g, \kappa, \gamma_{3D}\}$ (in the case of the Raman dressing scheme, g and γ_{3D}

should be replaced by the effective quantities rescaled by ϵ and ϵ^2, respectively). Each atom may then be viewed as fixed at a certain position during the time evolution. We obtain instances of such disordered realizations by sampling the position of the i^{th} atom from the distribution $p_i(\mathbf{r}) = \exp[-(\mathbf{r}-\mathbf{r}_i)^2/2\sigma^2]/(\sqrt{2\pi}\sigma)^3$, where $\mathbf{r}_i$ is the ideal position. For simplicity, we take the standard deviation σ to be the same in all three spatial directions. The expectation value of physical observables, such as g and κ, are computed by averaging over many disordered realizations. This approach has been shown to be exact in the limit of unsaturated atoms with infinite mass [140].

In the *fast-motion regime*, we consider the position fluctuations to be much faster than the internal dynamics, $\nu_{\text{T}} \gg \gamma_0$. As discussed in previous works [85, 86], the motional degrees of freedom can be adiabatically eliminated in this limit, which corresponds to averaging the dipole-dipole interaction over the position distribution of the atoms. Using the same position distributions $p_i(\mathbf{r})$ as for the frozen case, we show in Appendix 4.C that the resulting Hamiltonian is given by

$$\begin{aligned}\hat{H}_{\text{fast}} = &\sum_i H_{ii}\,\hat{\sigma}_i^+\hat{\sigma}_i^- - e^{-k_0^2\sigma^2/2}\sum_i\left(\Omega_i\hat{\sigma}_i^+ + \text{h.c.}\right)\\ &+ e^{-k_0^2\sigma^2}\sum_{i\neq j}\left(\Delta_{ij} - \frac{i}{2}\Gamma_{ij}\right)\hat{\sigma}_i^+\hat{\sigma}_j^-,\end{aligned} \tag{4.18}$$

where H_{ii} denotes the original coefficient of the $\hat{\sigma}_i^+\hat{\sigma}_i^-$ term in Eq. (4.1). The above expression is valid in the Lamb-Dicke limit, where $\eta = k_0\sigma \ll 1$.

In Fig. 4.6.4, we show κ and g as a function of σ for the two regimes. Motion causes scattering loss, resulting in an additional contribution to the cavity decay rate that is approximately given by $\kappa_{\text{loss}}^{\text{mot}} = \eta^2\gamma_0$ in both regimes [dashed curve in Fig. 4.6.4(a)]. For fast motion, this decay rate results from imperfect cancellation of the individual free-space decay rate γ_0 due to the suppression of the dipole–dipole interaction by the factor $e^{-\eta^2}$ in Eq. (4.18). We also show the results for frozen motion when we only add disorder in one of the three spatial dimensions. The impact of motion on κ is the largest in the z direction, orthogonal to the arrays, and smallest in the x direction. We attribute the latter to the fact that the atoms are polarized along the x axis such that the interaction in this direction is much weaker due to the dipole emission pattern. We have verified this claim by repeating the computation for atoms with a circularly polarized transition, in which case frozen disorder has identical effects in both in-plane directions. The coupling strength g is affected less significantly by the motion as it is merely rescaled by $e^{-\eta^2}$ [dashed curve in Fig. 4.6.4(b)]. For fast motion, this modification can again be understood in terms of the modified dipole-dipole interaction in Eq. (4.18).

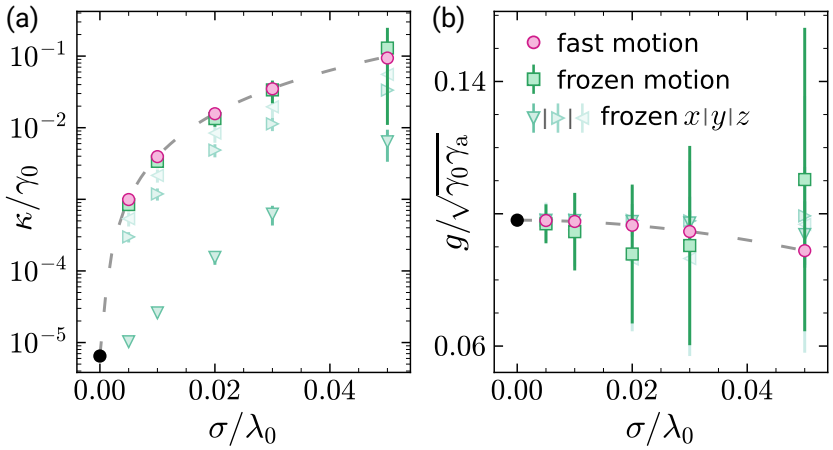

Figure 4.6.4: Effect of motion of the array atoms. (a) Cavity decay rate and (b) coupling strength as a function of the root-mean-square displacement σ. In both plots, we consider fast and frozen motion for an array cavity with $a = 0.47\lambda_0$, $w_0 = 3\lambda_0$, $L = 1.5\lambda_0$, and $N \times N = 30 \times 30$. In the frozen motion regime, we average over 200 disorder realizations and also show the results when the atoms are only free to move along the x axis (direction of the transition dipole), y axis, or z axis (cavity axis). The dashed lines represent the prediction from the fast-motion Hamiltonian in the Lamb-Dicke limit. The black dots indicate the results without motion.

We remark that the quantitative agreement of frozen and fast motion does not hold universally. We numerically observe that the loss in the two regimes is similar when the lattice constant satisfies $a \gtrsim 0.4\lambda_0$. When $a \lesssim 0.4\lambda_0$, frozen motion affects the cavity lifetime more severely whereas the impact of fast motion is independent of a. The enhanced sensitivity to frozen motion is caused by a degeneracy of the cavity mode with other subradiant eigenstates of the array. The static position disorder, which breaks the order of the array, induces detrimental hybridization of these modes. Small lattice constants should therefore be avoided in practice unless the (quasi) static positions of the atoms can be controlled to a high degree. Motional sidebands, which are relevant in intermediate regimes between frozen and fast motion, can also give rise to similar hybridization of the cavity mode with states detuned by an energy equal to the trap frequency. We do a quantitative analysis of this effect in [3].

Prediction for atoms trapped in an optical lattice

The above results indicate that losses due to motion are in many cases the dominant contribution to κ and therefore have a significant impact on the cooperativity. In this case, the highest cooperativities are achieved by cavities that maximize the coupling strength g while the value of the intrinsic cavity linewidth, previously discussed in Section 4.4.2, is unimportant. To estimate experimentally achievable values of the cooperativity, we consider an optical lattice as in [37, 38], where three pairs

of counterpropagating laser beams generate a three-dimensional, periodic trapping potential. For simplicity, we assume that the trapping potential is isotropic with trap depth V_0. Assuming deep traps, such that tunneling is weak, the trapping potential around the minima can be approximated by harmonic oscillators, with trap frequency $\nu_\mathrm{T} = 2\sqrt{V_0 E_\mathrm{r}}/\hbar$. Here, $E_\mathrm{r} = h^2/(8ma^2)$ is the recoil energy of an atom, which are assumed to all have equal mass m. The Wannier functions of the atoms are approximately Gaussian, characterized by the oscillator length $l = \sqrt{\hbar/2m\nu_\mathrm{T}}$.

We expect the lowest losses when all atoms are in their vibrational ground states such that $\sigma = l$. Following the preceeding discussion, we estimate the contribution to the cavity decay rate due to motion as

$$\kappa_\mathrm{loss}^\mathrm{mot} \approx \eta^2 \gamma_0 = 2\left(\frac{a}{\lambda_0}\right)^2 \sqrt{\frac{E_\mathrm{r}}{V_0}}\,\gamma_0\,. \tag{4.19}$$

By assuming that this rate is the dominant source of cavity decay, we obtain the estimate

$$C \approx \frac{4g^2}{\kappa_\mathrm{loss}^\mathrm{mot}\gamma_\mathrm{3D}} \approx \frac{9}{8\pi^3}\left(\frac{\lambda_0}{w_0}\right)^2\left(\frac{\lambda_0}{a}\right)^4 \sqrt{\frac{V_0}{E_\mathrm{r}}}\,\frac{\gamma_\mathrm{a}}{\gamma_\mathrm{3D}} \tag{4.20}$$

for the cooperativity. Here, we used the value of g as estimated without motion.

Our results indicate that the cooperativity can be maximized by minimizing the beam waist and lattice spacing while maximizing the trap depth. We note, however, that the validity of the expression is limited to regimes without motion-induced hybridization as discussed above, and that heating places a practical constraint on V_0 if the excited state is anti-trapped [37, 141]. We circumvent the latter concern by

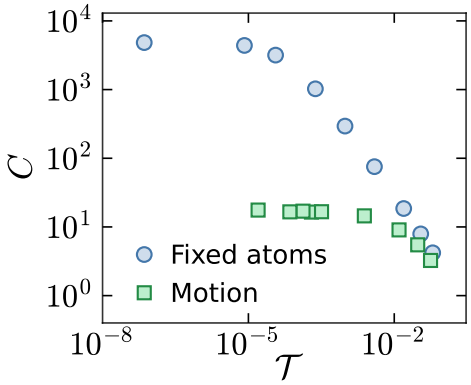

Figure 4.6.5: Cooperativity of an atom-array cavity as a function of the mirror transmission, $\mathcal{T}$. The array mirrors, each composed of 30×30 atoms, have lattice spacing $a = 0.47\lambda_0$ and are curved to achieve a beam waist $w_0 = 2\lambda_0$. The mirror transmission is determined by the frequency of the cavity mode, which is tuned by varying the cavity length from $1.5\lambda_0$ (smallest $\mathcal{T}$) to $1.54\lambda_0$ (largest $\mathcal{T}$). We show the results for the ideal case of pinned atoms (blue circles) and including losses due to atomic motion (green squares) as computed for ^{87}Rb in an optical lattice with a depth of 2000 recoil energies.

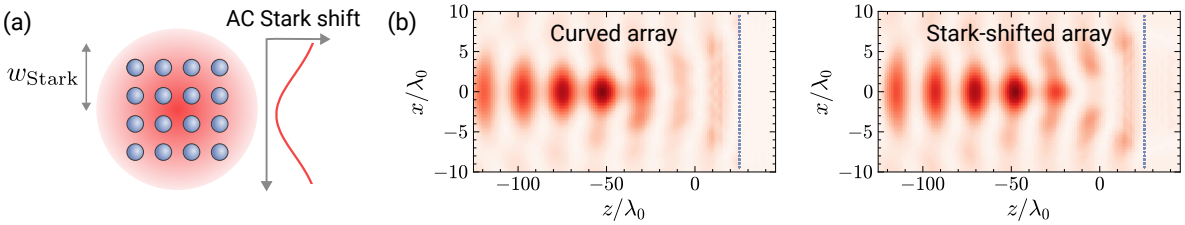

Figure 4.6.6: Effective curving of the mirrors with a position-dependent AC Stark shift. (a) The profile of a wide Gaussian beam produces a local detuning on the lattice atoms [see Eq. (4.21)], which imparts a position-dependent phase on the reflected light that mimics a curved mirror. (b) Electric field intensity for a plane wave incident from the left on a curved array (left panel) and a flat array with a position-dependent Stark shift (right panel). The array parameters are $a = 0.47\lambda_0$ and $N \times N = 40 \times 40$ in both cases and the frequency of the incident light is chosen to maximize reflection. The Stark shift on the flat array, quantified by $\alpha/w_{\mathrm{Stark}}^2 = 7 \times 10^{-3}\gamma_0/\lambda_0^2$, has been adjusted to match the radius of curvature $R = 270\lambda_0$ of the curved array. The maximum of the color scale for the Stark-shifted array is approximately 30% lower than that of the curved array.

assuming that the atoms are trapped at a magic wavelength. For the D_2 transition in ^{87}Rb ($\lambda_0 \approx 780$ nm) such a magic wavelength exists at $\lambda_{\mathrm{T}} \approx 740$ nm [130], this corresponds to $a = \lambda_{\mathrm{T}}/2 \approx 0.47\lambda_0$. Choosing a deep, yet realistic, lattice depth of $V_0 = 2000E_{\mathrm{r}}$ and a nearly diffraction limited beam waist of $w_0 = 2\lambda_0$, Eq. (4.20) yields a cooperativity of $\gamma_{3\mathrm{D}}C/\gamma_{\mathrm{a}} \approx 8.3$, in agreement with Fig. 4.6.5 considering that $\gamma_{3\mathrm{D}} \simeq 0.5\gamma_{\mathrm{a}}$ for $L \simeq 1.5\lambda_0$. We remark that these parameters correspond to an intermediate regime between frozen and fast motion since the trap frequency $\nu_{\mathrm{T}} \approx 2\pi \times 0.4$ MHz is much smaller than the D_2 linewidth $\gamma_0 \approx 2\pi \times 6$ MHz but greater than the cavity linewidth $\kappa_{\mathrm{loss}}^{\mathrm{mot}} \approx 2\pi \times 0.06$ MHz.

4.6.3 Optically induced curvature

The highest cooperativities computed above were obtained using curved array mirrors. When the atoms are trapped in an optical lattice, the curvature may in principle be created using the optical force of a focused laser or by means of a static field gradient. Owing to the accurate positioning required, this may, however, pose a significant practical challenge. In this section, we propose an alternative to curving the mirrors based on a position-dependent AC Stark shift, as shown in Fig. 4.6.6(a). The AC Stark shift induces a position-dependent phase that mimics the phase dependence of the wavefront of a Gaussian beam as illustrated in Fig. 4.6.6(b).

To analyze this effect, we suppose that the AC Stark shift is caused by a Gaussian beam with width w_{Stark} at the location of the mirror. The local detuning is given by

$$\delta_{\mathrm{Stark}}(r) = \alpha\left(1 - e^{-2r^2/w_{\mathrm{Stark}}^2}\right) \approx \frac{2\alpha r^2}{w_{\mathrm{Stark}}^2}, \tag{4.21}$$

where the coefficient α is set by the intensity of the Stark shift beam. We added a global offset to zero the shift at the center. The expansion of the exponential to first order is valid provided the width w_{Stark} is much larger than the size of the array mirrors. Since the mirror has a Lorentzian response with width Γ_0, the detuning causes the light in the cavity to acquire a phase shift

$$\Delta\phi(r) = \frac{2\delta_{\text{Stark}}(r)}{\Gamma_0} \approx \frac{4\alpha r^2}{\Gamma_0 w_{\text{Stark}}^2} \tag{4.22}$$

upon reflection, where we assumed that the central portion of the incident light is resonant with the mirror.

This phase shift results in an effective curvature of the wavefront. For a cavity with curved mirrors, the corresponding phase shift is given by $\Delta\phi(r) = k_0 r^2/R(L/2)$. We recall that the curvature of the mirrors is related to the waist by $R(L/2) = (L/2) + (k_0^2 w_0^4/2L) \approx k_0^2 w_0^4/2L$, where we restrict ourselves to the regime $k_0 w_0^2 \gg L$, which applies to the examples presented here. By equating the two expressions for the phase shift, we predict that the AC Stark shift induces an effective curvature that results in a cavity mode with beam waist

$$w_0 = \left(\frac{L\lambda_0 w_{\text{Stark}}^2}{4\pi}\frac{\Gamma_0}{\alpha}\right)^{1/4}. \tag{4.23}$$

We verify this prediction by computing the cavity modes of an array cavity as described in Section 4.4.1 including the position-dependent detuning. To extract the beam waist w_0, we fit a Gaussian to the wavefunction on one of the mirrors. This yields the beam width $w(L/2)$, from which the beam waist can be computed using the relation $w(L/2) = \sqrt{w_0^2 + (L/k_0 w_0)^2}$. The obtained value is in excellent agreement with Eq. (4.23) as shown in Fig. 4.6.7(a). We note that the values saturate at small α due to the finite size of the arrays. We also compute the coupling strength g and the cavity decay rate κ using the approaches described in Section 4.4.2. Figure 4.6.7(b) shows that the analytic expression for g, Eq. (4.10), remains valid when the waist is induced by the AC Stark shift instead of the curvature of the mirrors. However, as shown in Fig. 4.6.7(c), the Stark shift leads to an enhanced cavity decay rate compared to curved mirrors corresponding to the same beam waist. We attribute this to the fact that the detuned atoms modify the collective resonance of the array, reducing its reflectivity. The enhanced decay rate may not be detrimental in practice, where we expect the main contribution to κ to be caused by the motion of the atoms.

We note that the cavity length that yields the minimum values of κ deviates slightly from integer multiples of $\lambda_0/2$ due to the Gouy phase of the confined mode. We have accounted for this effect in Figs. 4.6.7(a–c) by adjusting L in the proximity of

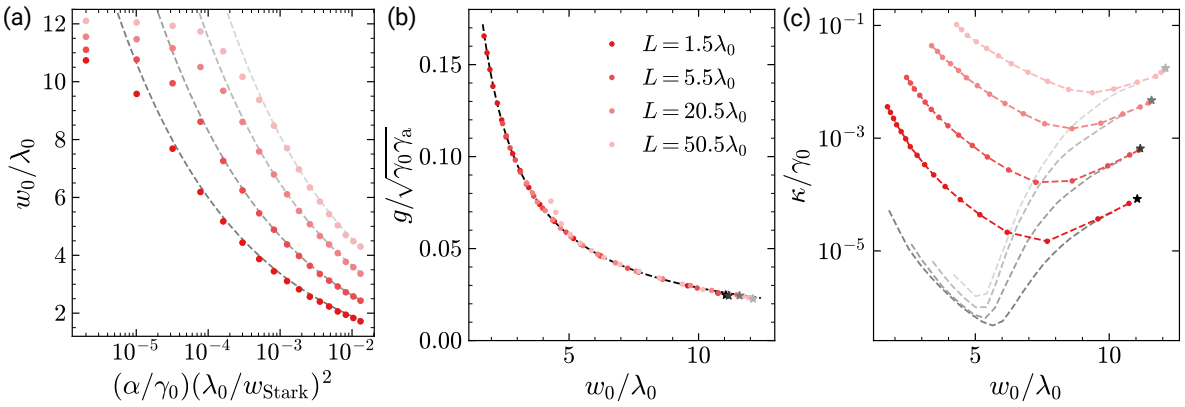

Figure 4.6.7: Cavity paramaters under an AC Stark shift. (a) Dependence of the beam waist, w_0, on the strength of the Stark shift for a cavity with $a = 0.47\lambda_0$, $N \times N = 60 \times 60$. We obtain w_0 by fitting a Gaussian to the wavefunction of the cavity eigenstate on the mirror. We fix $w_{\mathrm{Stark}} = 500\lambda_0$ although the exact value is unimportant. Deviations from the prediction [dashed curves, Eq. (4.23)] are due to the finite size of the arrays. (b) Dependence of the coupling strength, g, on the fitted value of w_0 for the same cavities as in (c). The stars are the results for flat mirrors without the AC Stark shift. As for curved mirrors, the coupling strength follows Eq. (4.10), represented by the dashed line. (c) By contrast, the cavity decay rate κ under the AC Stark differs significantly from value with curved mirrors with the same beam waist (dashed curves). Smaller values of w_0, corresponding to larger values of α, lead to increased loss.

the stated values such that κ is at a local minimum. The observed correction to L is proportional to $L/(k_0 w_0)^2$, in accordance with the expectation from the Gouy phase.

4.7 Discussion and outlook

Our work establishes atom arrays as a promising platform for cavity QED. We show that atom array cavities can be described by the same parameters as conventional cavity QED setups. The coupling strength g and the cavity decay rate κ, however, are reduced compared to conventional setups due to the time delay that light experiences when reflected by a narrow-band mirror. The reduction in these two parameters cancels when computing the cooperativity $C = 4g^2/\kappa\gamma_{3D}$. Hence, array cavities and conventional cavities with equivalent mirrors in terms of curvature and reflection result in the same cooperativity. We highlight that in the case of array cavities, the cavity length determines the detuning of the cavity mode from the resonance of the array mirrors. The reflection coefficient of the mirror should therefore be viewed as a function of the cavity length.

Figure 4.7.1 summarizes these findings by showing the cooperativity as a function of $\lambda_0^2/[(1-\mathcal{R})w_0^2]$ for a variety of configurations, including the limitations considered in Section 4.6. We show $\gamma_{3D}C/\gamma_a$ instead of C to simplify comparison as the value

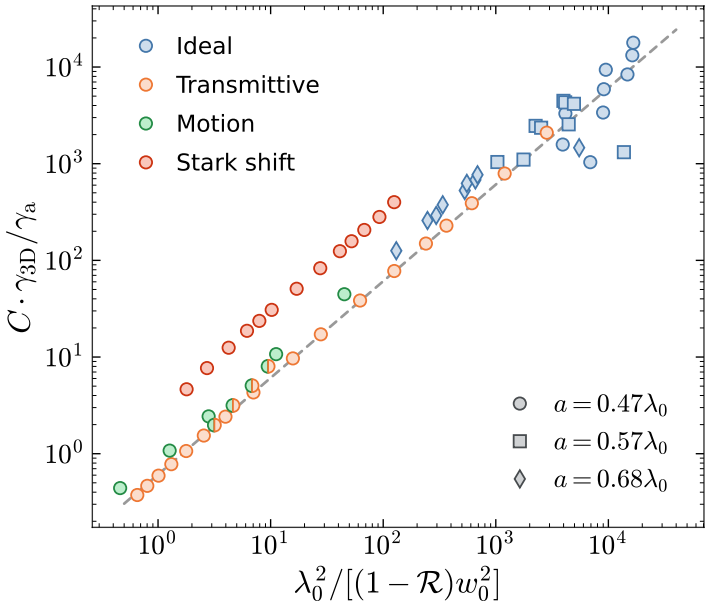

Figure 4.7.1: Cooperativity, C, as a function of $\lambda_0^2/[(1-\mathcal{R})w_0^2]$, where $\mathcal{R}$ is the reflection coefficient of a single mirror at the resonance frequency of the cavity. We provide the range of parameters of the cavities in Appendix 4.D. The points labeled "ideal" correspond to the cavities considered in Section 4.4, where the atoms are fixed and L is an integer multiple of $\lambda_0/2$. The labels "transmittive", "motion", and "Stark shift" refer to the practical scenarios discussed in Section 4.6.1, 4.6.2, and 4.6.3, respectively. We scale the cooperativity by γ_{3D}/γ_a to highlight the dependence on $\mathcal{R}$ and w_0. All data points agree well with the theoretical prediction, Eq. (4.12) (dashed line), which also holds for conventional cavities.

of γ_{3D}, which ranges from $0.5\,\gamma_a$ to γ_a for the array cavities displayed in the figure, would lead to increased scatter. The computed cooperativities are all close to the analytical prediction [Eq. (4.12), dashed line] based on the beam waist and the separately obtained reflection coefficient of a single array mirror. We observe the most significant deviation for array cavities where the beam waist is defined using an AC Stark shift (red circles). The discrepancy is explained by the fact that the AC Stark shift results in a weakly non-Gaussian profile of the cavity mode. This in turn leads to a systematic underestimate of the reflection coefficient because $\mathcal{R}$ is computed by projecting onto a Gaussian beam. The same reasoning applies to cavities with minimal transmission, where L is an integer multiple of $\lambda_0/2$ [c.f. Fig. 4.6.3(b)]. For the points below the dashed line, we hypothesize that their cooperativity is reduced due to coupling between different cavity modes, which results in loss not captured by the reflection coefficient of a single mirror.

Our work focuses on maximizing the cooperativity as a key figure of merit for applications in quantum communication protocols. We highlight that simpler configurations may be sufficient to demonstrate the experimental viability of the proposed platform in the near term. For instance, our numerical results indicate that small flat arrays, where the transverse confinement of the cavity mode is due to boundary

effects, can achieve cooperativities exceeding unity. Concretely, using $a = 0.47\lambda_0$, $L = 1.5\lambda_0$, $N \times N = 10 \times 10$, and $V_0 = 2000E_\mathrm{r}$, we obtain $C \simeq 4$. The cooperativity can be subsequently improved by adding a position-dependent AC Stark shift. This scheme may be of interest in its own right and could, for instance, be used to create metalenses from flat atom arrays.

There are several avenues to improving the properties of array cavities. The cooperativity can be increased by a tighter confinement with higher laser intensities, assuming trapping at a magic wavelength. To reduce the sensitivity to motion and disorder, one could optimize the individual positions of the atoms beyond the simple curved arrays considered here. Scattering may be suppressed by closing the cavity with a cylindrical array, albeit at the cost of increased experimental complexity. We emphasize that our proposal is not limited to ultracold atoms in optical lattices but applies to arrays of dipoles in general. It may be fruitful in this context to explore realizations based on optical tweezer arrays, which allow for versatile geometries [142]. The limitations due to motion could be overcome by using solid-state emitters, although such systems often suffer from detrimental inhomogeneous broadening [143]. Finally, similar phenomena may be explored in two-dimensional semiconductors, where delocalized excitons take the role of the discrete emitters [144–146].

Our results establish a theoretical foundation for the description of array cavities using the language of conventional cavity QED. It will be exciting to move beyond this framework to explore phenomena that take advantage of features of atom arrays not accessible with conventional mirrors. A particularly intriguing direction is to explore the dynamics of two or more excitations since atom-array cavities have been shown to exhibit quantum nonlinearities at the single-photon level [123, 124]. In combination with the ability to dynamically control the arrays, this approach may enable on-demand generation of complex quantum states of light.

APPENDIX

4.A SELF-ENERGY

In this section, we justify the use of the spectral function Eq. (4.7) to study the atom-array cavity and motivate the underlying physical intuition. To understand the interaction of the target atom with the atom-array cavity, we initialize the target atom in its excited state and let it evolve under the presence of the cavity. We consider a single target atom and do not include an external drive. Using the definitions introduced in Section 4.4.1, the Hamiltonian Eq. (4.1) reads

$$\hat{H} = (\omega_{\mathrm{a}} - \frac{i}{2}\gamma_{\mathrm{a}})\hat{\sigma}_{\mathrm{a}}^{+}\hat{\sigma}_{\mathrm{a}}^{-} + \sum_{i,j} \mathbf{H}_{ij}^{\mathrm{AA}}\, \hat{\sigma}_{i}^{+}\hat{\sigma}_{j}^{-} + \sum_{i} \left(\mathbf{H}_{i}^{\mathrm{AT}}\, \hat{\sigma}_{i}^{+}\hat{\sigma}_{\mathrm{a}}^{-} + \mathbf{H}_{i}^{\mathrm{TA}}\, \hat{\sigma}_{\mathrm{a}}^{+}\hat{\sigma}_{i}^{-}\right) . \tag{4.24}$$

We define the state $|\psi(t)\rangle = c_{\mathrm{a}}(t)\, \hat{\sigma}_{\mathrm{a}}^{+}\, |0\rangle + \sum_i c_i(t)\, \hat{\sigma}_i^{+}\, |0\rangle$, with $c_{\mathrm{a}}(0) = 1$. By projecting the Schrödinger equation onto the different basis states, we obtain the equations of motion

$$\dot{c}_{\mathrm{a}}(t) = -i(\omega_{\mathrm{a}} - \frac{i}{2}\gamma_{\mathrm{a}})\, c_{\mathrm{a}}(t) - i \sum_{i} \mathbf{H}_{i}^{\mathrm{TA}}\, c_i(t)\,, \tag{4.25}$$

$$\dot{c}_i(t) = -i \sum_{j} \mathbf{H}_{ij}^{\mathrm{AA}}\, c_j(t) - i\mathbf{H}_{i}^{\mathrm{AT}}\, c_{\mathrm{a}}(t)\,. \tag{4.26}$$

This set of equations can be solved by performing a Laplace transform, which we define with an imaginary variable $f(\omega) = \mathcal{L}\{f(t)\}(-i\omega)$. The transformed equations of motion read

$$-i\omega\, c_{\mathrm{a}}(\omega) - 1 = -i(\omega_{\mathrm{a}} - \frac{i}{2}\gamma_{\mathrm{a}})\, c_{\mathrm{a}}(\omega) - i \sum_{i} \mathbf{H}_{i}^{\mathrm{TA}}\, c_i(\omega) \tag{4.27}$$

$$-i\omega\, c_i(\omega) = -i \sum_{j} \mathbf{H}_{ij}^{\mathrm{AA}}\, c_j(\omega) - i\mathbf{H}_{i}^{\mathrm{AT}}\, c_{\mathrm{a}}(\omega)\,, \tag{4.28}$$

Isolating $c_i(\omega)$ from Eq. (4.28) and substituting it into Eq. (4.27), yields

$$c_{\mathrm{a}}(\omega) = i\left[\omega - \omega_{\mathrm{a}} + \frac{i}{2}\gamma_{\mathrm{a}} - \Sigma_{\mathrm{a}}(\omega)\right]^{-1}\,, \tag{4.29}$$

with the self-energy of the target atom $\Sigma_a(\omega)$ as defined in Eq. (4.6). To obtain the time dynamics, we would then proceed to carry out the inverse Laplace transform, which coincides with the inverse Fourier transform in Eq. (4.5).

If the cavity perturbs the target atom only weakly, such that the self-energy is flat across the range of frequencies probed by the atom, we can make the pole approximation, $\Sigma_a(\omega) \approx \Sigma_a(\omega_a)$. The solution to the time dynamics is that of an atom in free space with the resonance energy and decay rate modified by $\Sigma_a(\omega_a)$.

For frequencies near strong poles of Eq. (4.29), the solution is more involved. In this case, we can compare Eq. (4.29) to the equivalent solution using the effective Jaynes-Cummings Hamiltonian,

$$c_a^{\text{conv}}(\omega) = i\left[\omega - \omega_a + \frac{i}{2}\gamma_{3D} - \frac{g^2}{\omega - \omega_c + \frac{i}{2}\kappa}\right]^{-1}, \tag{4.30}$$

and observe that an isolated resonance in $\Sigma_a(\omega)$ generates the same dynamics as conventional cavity QED. The imaginary part of the last term of Eq. (4.30) is a Lorentzian with height g^2/κ, centered at the resonance energy of the cavity mode ω_c. Therefore, we can extract g, κ and ω_c from fitting a Lorentzian to $\text{Im}\{\Sigma_a(\omega\}$. As we discuss in Section 4.4.1, single eigenstates of the atom-array cavity are responsible for the observed cavity-like resonances. This allows us to also extract the cavity parameters from the Hamiltonian without the need for fitting.

Finally, by subtracting from $\Sigma_a(\omega)$ the contribution of the cavity eigenstates responsible for a cavity resonance, which yields $\Sigma_{a,\text{weak}}(\omega)$ that perturbs the target atom weakly, we can obtain the effective free-space decay of the target atom, $\gamma_{3D} = \gamma_a - 2\,\text{Im}\{\Sigma_{a,\text{weak}}(\omega_a)\}$.

4.B Raman scheme

In this section we derive the Hamiltonian governing the effective dynamics between the two long-lived states $|g_1\rangle, |g_2\rangle$ of the Raman scheme presented in Fig. 4.5.1. To this end, we adiabatically eliminate the excited state of the target atoms $|e\rangle$ to second order in perturbation theory. Because we are interested in the regimes in which the atom-array cavity sustains a well-defined cavity mode, we approximate the array part of the Hamiltonian by a conventional cavity as described in Section 2.4.3. When the free-space interaction between target atoms is much smaller than the atom–cavity coupling, as in the configurations discussed in Fig. 4.5.3, we can neglect the former and derive the effective dynamics for a single target atom. The extension to multiple atoms is straightforward.

The Hamiltonian including the Raman scheme described in Section 4.5, in a frame in which $|g_2\rangle$ rotates with the frequency of the Raman drive and $\hat{a}$ and $|g_1\rangle$ rotate with ω_c, reads

$$\begin{aligned}\hat{H} =& -\frac{i}{2}\kappa\,\hat{a}^\dagger\hat{a} + (\omega_c - \Delta_1 + \Delta_2)\,|g_2\rangle\langle g_2| + (\omega_c - \Delta_1 - \frac{i}{2}\gamma_{3D})\,|e\rangle\langle e| \\ &+ \omega_c\,|g_1\rangle\langle g_1| + \frac{\Omega}{2}\,(|g_2\rangle\langle e| + \text{h.c.}) + g\,(|g_1\rangle\langle e|\,\hat{a}^\dagger + \text{h.c.})\ .\end{aligned} \tag{4.31}$$

By shifting the energy of the atomic subspace by $(\Delta_1 - \Delta_2)/2 - \omega_c$, the diagonal part of the Hamiltonian becomes

$$\hat{H}_0 = -\frac{i}{2}\kappa\,\hat{a}^\dagger\hat{a} + \frac{\Delta_2 - \Delta_1}{2}\,(|g_2\rangle\langle g_2| - |g_1\rangle\langle g_1|) - \left(\frac{\Delta_1 + \Delta_2}{2} + \frac{i}{2}\gamma_{3D}\right)|e\rangle\langle e|\,. \tag{4.32}$$

For $|\Delta_1 + \Delta_2|/2 \gg |\Delta_1 - \Delta_2|/2, \Omega, g$, the state $|e\rangle$ will only be weakly populated. We define the projector onto the subspace that includes $|g_1\rangle$ and $|g_2\rangle$,

$$\hat{P} = (|g_2\rangle\langle g_2| + |g_1\rangle\langle g_1|) \otimes \mathbf{I}_c\,, \tag{4.33}$$

and the complementary projection containing $|e\rangle$,

$$\hat{Q} = \mathbf{I} - \hat{P} = |e\rangle\langle e| \otimes \mathbf{I}_c\,, \tag{4.34}$$

where $\mathbf{I}_c$ is the identity matrix acting on the cavity subspace. Upon adiabatically eliminating $|e\rangle$, the dynamics in the low-energy subspace are described to second order in perturbation theory by the Hamiltonian [88, 147]

$$\hat{H}_{\text{eff}} = \hat{P}(\hat{H}_0 + \hat{V})\hat{P} - \hat{P}\hat{V}(\hat{Q}\hat{H}_0\hat{Q})^{-1}\hat{V}\hat{P}\,, \tag{4.35}$$

where

$$\hat{V} = \frac{\Omega}{2}\,|g_2\rangle\langle e| + g\,|g_1\rangle\langle e|\,\hat{a}^\dagger + \text{h.c.} \tag{4.36}$$

is the part of the Hamiltonian that couples $\hat{P}$ and $\hat{Q}$.

The second-order term of the effective Hamiltonian reads

$$\left(\frac{\Omega}{2}\,|g_2\rangle + g\,|g_1\rangle\,\hat{a}^\dagger\right)\left(\frac{1}{2}(\Delta_1 + \Delta_2) + \frac{i}{2}\gamma_{3D} + \frac{i}{2}\kappa\hat{a}^\dagger\hat{a}\right)^{-1}\left(\frac{\Omega}{2}\,\langle g_2| + g\,\langle g_1|\,\hat{a}\right). \tag{4.37}$$

In the main text, we only consider the single-excitation subspace $\{|g_2\rangle\,|0\rangle_c\,, |g_1\rangle\,|1\rangle_c\}$, with $|1\rangle_c = \hat{a}^\dagger\,|0\rangle_c$, for which the $i\kappa\hat{a}^\dagger\hat{a}/2$ term in the denominator equals zero. This term can also be safely neglected for a small number of photons in the cavity if $\kappa \ll |\Delta_1 + \Delta_2|/2, \gamma_{3D}$. We will therefore neglect this term in what follows.

The resulting effective Hamiltonian after adding a global energy shift $(\Delta_2-\Delta_1)/2$ to the atomic states reads

$$\begin{aligned}\hat{H}_{\text{eff}} = &\left(-\frac{i}{2}\kappa + \frac{2g^2}{(\Delta_1+\Delta_2)+i\gamma_{3D}}\,|g_1\rangle\langle g_1|\right)\hat{a}^\dagger\hat{a} \\ &+ \left(\Delta_2-\Delta_1+\frac{\Omega^2/2}{(\Delta_1+\Delta_2)+i\gamma_{3D}}\right)|g_2\rangle\langle g_2| \\ &- \frac{g\,\Omega}{(\Delta_1+\Delta_2)+i\gamma_{3D}}\left(|g_2\rangle\langle g_1|\,\hat{a}+\text{h.c.}\right).\end{aligned} \tag{4.38}$$

The two-photon transition connecting $|g_1\rangle \leftrightarrow |g_2\rangle$ is resonant for $\Delta_1 \approx \Delta_2$ up to small Stark shift corrections. In the regime $|\Delta_1| \gg \gamma_{3D}$, the dynamics of the effective target atom are well approximated by a two-level atom with the reduced free-space decay rate and coupling strength with the cavity mode defined in Section 4.5. Note that for smaller $|\Delta_1| \sim \gamma_{3D}$, the first and third line of Eq. (4.38) contain additional dissipative (anti-Hermitian) terms. By requiring that the corresponding rates are much smaller than the cavity decay rates, we can obtain a more precise condition for Δ_1 in relation to γ_{3D}. In particular we need $g^2\gamma_{3D}/\Delta_1^2 \ll \kappa$ and $g\Omega\gamma_{3D}/\Delta_1^2 \ll \kappa$. Using $\Omega/\Delta_1 = \sqrt{\kappa/\gamma_{3D}}$, both conditions are satisfied when $|\Delta_1| \gg \sqrt{C}\gamma_{3D}$.

4.C Effective Hamiltonian in the fast-motion regime

In the fast-motion regime, the effective Hamiltonian should be averaged over the fluctuations of the positions of the atoms. There are two distinct quantities in Eq. (4.1) that depend on the position of the atoms: the interaction coefficients $\Delta_{ij} - i\Gamma_{ij}/2$ and the Rabi frequencies Ω_i. For both quantities, the average can be evaluated analytically in the limit that the fluctuations are small compared to the wavelength λ_0 and the lattice spacing a.

For the interaction coefficients, we have to compute the average of the Green's function $\mathbf{G}(\mathbf{r}_i+\mathbf{r}, \mathbf{r}_j+\mathbf{r}'; \omega_0)$, where $\mathbf{r}$ and $\mathbf{r}'$ are drawn independently from the probability distribution $p(\mathbf{r}) = e^{-r^2/2\sigma^2}/(2\pi\sigma^2)^{3/2}$. To simplify notation, we introduce the shorthand $\mathbf{G}(\mathbf{r}_i-\mathbf{r}_j) = \mathbf{G}(\mathbf{r}_i, \mathbf{r}_j; \omega_0)$. We obtain the averaged Green's function

$$\begin{aligned}\bar{\mathbf{G}}(\mathbf{r}_i-\mathbf{r}_j) &= \int \mathrm{d}^3\mathbf{r}\int \mathrm{d}^3\mathbf{r}' p(\mathbf{r})p(\mathbf{r}')\mathbf{G}(\mathbf{r}_i+\mathbf{r}-\mathbf{r}_j-\mathbf{r}') \\ &= \frac{1}{(4\pi\sigma^2)^{3/2}}\int \mathrm{d}^3\mathbf{r}\,\mathbf{G}(\mathbf{r}_i-\mathbf{r}_j+\mathbf{r})e^{-r^2/4\sigma^2} \\ &\approx \mathbf{G}(\mathbf{r}_i-\mathbf{r}_j) + \sigma^2\,\nabla^2\mathbf{G}(\mathbf{r})\big|_{\mathbf{r}=\mathbf{r}_i-\mathbf{r}_j},\end{aligned} \tag{4.39}$$

where the last line follows from expanding $\mathbf{G}(\mathbf{r}_i - \mathbf{r}_j + \mathbf{r})$ to second order in $\mathbf{r}$, corresponding to a saddle-point approximation. To evaluate the Laplacian, we make use of the definition of the Green's function,

$$\nabla \times \nabla \times \mathbf{G}(\mathbf{r}) - k_0^2 \mathbf{G}(\mathbf{r}) = \delta(\mathbf{r})\mathbf{I}. \tag{4.40}$$

At $\mathbf{r} \neq 0$, the Green's function further satisfies $\nabla \cdot \mathbf{G}(\mathbf{r}) = 0$ because $\mathbf{G}(\mathbf{r})$ is an electric field, which is divergence free in the absence of sources. Using $\nabla \times \nabla \times \mathbf{G} = \nabla(\nabla \cdot \mathbf{G}) - \nabla^2 \mathbf{G}$, the Green's function therefore satisfies

$$\left(\nabla^2 + k_0^2\right) \mathbf{G}(\mathbf{r}) = 0, \qquad \text{if } \mathbf{r} \neq 0. \tag{4.41}$$

Combining everything yields

$$\bar{\mathbf{G}}(\mathbf{r}_i - \mathbf{r}_\mathbf{j}) \approx (1 - k_0^2\sigma^2)\mathbf{G}(\mathbf{r}_i - \mathbf{r}_\mathbf{j}) \approx e^{-k_0^2\sigma^2}\mathbf{G}(\mathbf{r}_i - \mathbf{r}_\mathbf{j}). \tag{4.42}$$

This justifies the rescaling factor of the last term in Eq. (4.18).

A very similar argument applies to the Rabi frequency. Within the saddle-point approximation, the averaged Rabi frequency is given by

$$\bar{\Omega}_i = \int \mathrm{d}^3\mathbf{r}\, p(\mathbf{r})\, \mathbf{d}_i^* \cdot \mathbf{E}(\mathbf{r}_i + \mathbf{r}) \tag{4.43}$$

$$\approx \Omega_i + \frac{1}{2}\sigma^2\, \mathbf{d}_i^* \cdot \nabla^2 \mathbf{E}(\mathbf{r})\big|_{\mathbf{r}=\mathbf{r}_i}. \tag{4.44}$$

We again use $(\nabla^2 + k_0^2)\mathbf{E}(\mathbf{r}) = 0$ to obtain

$$\bar{\Omega}_i \approx e^{-k_0^2\sigma^2/2}\, \Omega_i. \tag{4.45}$$

This is the second term in Eq. (4.18).

4.D Extended description of Fig. 4.7.1

The "ideal" points are computed for cavities with curved arrays. We consider lattice spacings $a = 0.47\lambda_0$, $a = 0.57\lambda_0$, and $a = 0.68\lambda_0$ and sizes $N \times N = 60 \times 60$, $N \times N = 50 \times 50$, and $N \times N = 40 \times 40$, respectively, for all combinations of $w_0/\lambda_0 \in \{2.5, 3.8, 5.0\}$, and $L/\lambda_0 \in \{5.5, 20.5, 50.5\}$. We also computed the results for $L = 1.5\lambda_0$. They are very similar to the ones for $L = 5.5\lambda_0$, except when $a = 0.68\lambda_0$, for which the target atom experiences a strong near-field interaction with the arrays, departing from the optical cavity regime (see Fig. 4.4.2, right panel).

Apart from a few exceptions, the "ideal" points are consistently above the theory

line by a factor of roughly $3/2$. We attribute this shift to differences between the mode profile and the Gaussian beam used to probe the mirror's reflectivity [see Fig. 4.6.3(b)], leading to a systematic underestimate of $\mathcal{R}$. The outliers below the theoretical prediction are likely due to the coupling between different cavity modes. The "ideal" points furthest below the dashed line for the three values of a correspond to cavities with $w_0 = 2.5\lambda_0$ and $L = 50.5\lambda_0$. These points have the largest value of the ratio L/R, where R is the radius of curvature of the mirror. A large value of L/R leads to a small separation between TEM_{mn} modes, as discussed in Section 4.4.2. The small splitting results in increased mixing of the transverse modes, which is not accounted for in the computation of the reflection coefficient of a single array mirror.

The "transmittive" points include the data of the cavities shown in Fig. 4.6.3(a) in the range $L/\lambda_0 \in [5.45, 5.50)$. In this case, the modes have Gaussian profiles, so the agreement with the theory is excellent. The increased κ_{out} of these cavities comes naturally at the expense of smaller C. The "motion" points include the data shown in Fig. 4.6.4 in the frozen motion regime, for which κ_{out} is very small. The points that are colored as half "motion" and half "transmittive" correspond to the points shown in Fig. 4.6.5. The "Stark shift" points correspond to the data shown in Fig. 4.6.7(a–c). The top half of the points are for $L = 1.5\lambda_0$, and the bottom half for $L = 5.5\lambda_0$. We show points in the range starting with $w_0 \approx 6\lambda_0$ down to $w_0 \approx 2\lambda_0$. We do not show the points with larger beam waists, as they have strong diffraction losses. The profile of the cavity mode with Stark-shifted mirrors differs the most from a Gaussian mode, which explains the larger displacement from the dashed line.

Acknowledgements

I would like to express my gratitude to many people that have been part of my PhD journey over the past years. Their help and support has always been very important to me.

First of all, I am very grateful to my supervisor Ignacio Cirac for his guidance during my PhD and for having given me the opportunity to work in such an inspiring environment. I highly appreciated his original thinking, his kindness and his guiding as a mentor.

I am thankful to Dominik Wild for his guidance and support as a co-supervisor during the second half of my PhD and for his invaluable feedback on this thesis. I am also thankful to Cosimo Rusconi and Daniel Malz, who fulfilled a similar role at the beginning of my PhD. They have all always been ready to help and I have learned a lot from them.

I would also like to thank Sirui Lu, Maximilian Lutz, María Cea, Irene Papaefstathiou and Arthur Christianen for being such lovely officemates.

I want to thank all the people at MPQ that have enriched my time here both scientifically and socially, including Albert Gasull, Bennet Windt, Guillermo González, Adrián Franco, Benjamin Schiffer, Esther Cruz, Patrick Emonts, Giacomo Giudice, Miguel Frías, Marta Florido, Reinis Irmejs, Denise Cocchiarella, Marianna Crupi, Miguel Bello, Eduardo Sánchez, Jiří Guth Jarkovský, Kristian Nielsen, Georgios Styliaris, Flavio Baccari and many others. I am also grateful to Andrea Kluth, Regina Jasny and Andrea Angione for their support in administration matters, and to Sonya Gzyl for her great job at coordinating the IMPRS program.

Finally, I want to thank my family and Neele for having been a constant source of support.

BIBLIOGRPAHY

[1] David Castells-Graells et al. „Atomic waveguide QED with atomic dimers“. In: *Physical Review A* 104.6 (2021), p. 063707. DOI: 10.1103/PhysRevA.104.063707.

[2] David Castells-Graells, J Ignacio Cirac, and Dominik S Wild. „Cavity Quantum Electrodynamics with Atom Arrays in Free Space“. In: *arXiv preprint arXiv:2409.15434* (2024).

[3] K. K. Nielsen et al. „Polaron-Polaritons in Subwavelength Arrays of Trapped Atoms“. in preparation.

[4] Antoine Browaeys and Thierry Lahaye. „Many-body physics with individually controlled Rydberg atoms“. In: *Nature Physics* 16.2 (2020), pp. 132–142.

[5] Loïc Henriet et al. „Quantum computing with neutral atoms“. In: *Quantum* 4 (2020), p. 327. DOI: https://doi.org/10.22331/q-2020-09-21-327.

[6] Andrew J Daley et al. „Practical quantum advantage in quantum simulation“. In: *Nature* 607.7920 (2022), pp. 667–676. DOI: https://doi.org/10.1038/s41586-022-04940-6.

[7] C. Monroe. „Quantum Information Processing with Atoms and Photons“. In: *Nature* 416.6877 (2002), pp. 238–246. DOI: 10.1038/416238a.

[8] Changsuk Noh and Dimitris G Angelakis. „Quantum Simulations and Many-Body Physics with Light“. In: *Reports on Progress in Physics* 80.1 (2017), p. 016401. DOI: 10.1088/0034-4885/80/1/016401.

[9] P. Kómár et al. „A quantum network of clocks“. In: *Nature Physics* 10.8 (June 2014), pp. 582–587. DOI: 10.1038/nphys3000.

[10] Darrick E. Chang, Vladan Vuletić, and Mikhail D. Lukin. „Quantum Nonlinear Optics — Photon by Photon“. In: *Nature Photonics* 8.9 (2014), pp. 685–694. DOI: 10.1038/nphoton.2014.192.

[11] Pedro De Vries, David V Van Coevorden, and Ad Lagendijk. „Point scatterers for classical waves“. In: *Reviews of Modern Physics* 70.2 (1998), p. 447. DOI: 10.1103/RevModPhys.70.447.

[12] S. J. van Enk and H. J. Kimble. „Single atom in free space as a quantum aperture“. In: *Phys. Rev. A* 61 (5 Mar. 2000), p. 051802. DOI: 10.1103/PhysRevA.61.051802.

[13] Meng Khoon Tey et al. „Strong interaction between light and a single trapped atom without the need for a cavity“. In: *Nature Physics* 4.12 (Oct. 2008), pp. 924–927. DOI: 10.1038/nphys1096.

[14] Andreas Reiserer and Gerhard Rempe. „Cavity-based quantum networks with single atoms and optical photons“. In: *Reviews of Modern Physics* 87.4 (2015), p. 1379. DOI: 10.1103/RevModPhys.87.1379.

[15] D. E. Chang et al. „Colloquium: Quantum Matter Built from Nanoscopic Lattices of Atoms and Photons“. In: *Reviews of Modern Physics* 90.3 (2018), p. 031002. DOI: 10.1103/RevModPhys.90.031002.

[16] Hendrik Antoon Lorentz. *The theory of electrons and its applications to the phenomena of light and radiant heat*. Vol. 29. GE Stechert & Company, 1916.

[17] Claude Cohen-Tannoudji, Jacques Dupont-Roc, and Gilbert Grynberg. *Photons and atoms-introduction to quantum electrodynamics*. 1997.

[18] C. W. Gardiner and M. J. Collett. „Input and output in damped quantum systems: Quantum stochastic differential equations and the master equation“. In: *Phys. Rev. A* 31 (6 June 1985), pp. 3761–3774. DOI: 10.1103/PhysRevA.31.3761.

[19] Kazuaki Sakoda and Kazuo Ohtaka. „Optical response of three-dimensional photonic lattices: Solutions of inhomogeneous Maxwell's equations and their applications“. In: *Physical Review B* 54.8 (1996), p. 5732.

[20] Cole P Van Vlack. *Dyadic green functions and their applications in classical and quantum nanophotonics*. Queen's University (Canada), 2012.

[21] Jonathan David Hood. „Atom-light interactions in a photonic crystal waveguide“. PhD thesis. California Institute of Technology, 2017.

[22] Claude Cohen-Tannoudji, Jacques Dupont-Roc, and Gilbert Grynberg. *Atom-photon interactions: basic processes and applications*. 1998.

[23] RH Lehmberg. „Radiation from an N-atom system. I. General formalism“. In: *Physical Review A* 2.3 (1970), p. 883. DOI: 10.1103/PhysRevA.2.883.

[24] R. H. Lehmberg. „Radiation from an N-Atom System. II. Spontaneous Emission from a Pair of Atoms“. In: *Phys. Rev. A* 2 (3 Sept. 1970), pp. 889–896. DOI: 10.1103/PhysRevA.2.889.

[25] Jean Dalibard, Yvan Castin, and Klaus Mølmer. „Wave-function approach to dissipative processes in quantum optics“. In: *Physical review letters* 68.5 (1992), p. 580. DOI: 10.1103/PhysRevLett.68.580.

[26] Howard Carmichael. *An open systems approach to quantum optics: lectures presented at the Université Libre de Bruxelles, October 28 to November 4, 1991*. Vol. 18. Springer Science & Business Media, 2009.

[27] Klaus Mølmer, Yvan Castin, and Jean Dalibard. „Monte Carlo wave-function method in quantum optics“. In: *JOSA B* 10.3 (1993), pp. 524–538. DOI: 10.1364/JOSAB.10.000524.

[28] A. Asenjo-Garcia et al. „Exponential Improvement in Photon Storage Fidelities Using Subradiance and “Selective Radiance” in Atomic Arrays“. In: *Phys. Rev. X* 7 (3 Aug. 2017), p. 031024. DOI: 10.1103/PhysRevX.7.031024.

[29] Robert J Bettles, Simon A Gardiner, and Charles S Adams. „Enhanced optical cross section via collective coupling of atomic dipoles in a 2D array“. In: *Physical review letters* 116.10 (2016), p. 103602. DOI: 10.1103/PhysRevLett.116.103602.

[30] Ephraim Shahmoon et al. „Cooperative resonances in light scattering from two-dimensional atomic arrays“. In: *Physical Review Letters* 118.11 (2017), p. 113601. DOI: 10.1103/PhysRevLett.118.113601.

[31] E M Purcell. „Spontaneous emission probabilities at radio frequencies“. In: *Physical Review* 69 (1946), p. 681. DOI: 10.1103/PhysRev.69.681.

[32] Lukas Novotny and Bert Hecht. *Principles of nano-optics*. Cambridge university press, 2012.

[33] John D Joannopoulos et al. „Molding the flow of light“. In: *Princeton Univ. Press, Princeton, NJ [ua]* (2008).

[34] Herbert Walther et al. „Cavity quantum electrodynamics“. In: *Rep. Prog. Phys.* 69.5 (2006), p. 1325. DOI: 10.1088/0034-4885/69/5/R02.

[35] Crispin Gardiner and Peter Zoller. *The quantum world of ultra-cold atoms and light Book I: Foundations of Quantum Optics*. Vol. 2. Imperial College Press, 2014.

[36] Crispin W Gardiner and Peter Zoller. *Quantum World Of Ultra-cold Atoms And Light, The-Book Iii: Ultra-cold Atoms*. Vol. 5. World Scientific, 2017.

[37] Jun Rui et al. „A subradiant optical mirror formed by a single structured atomic layer“. In: *Nature* 583.7816 (2020), pp. 369–374. DOI: 10.1038/s41586-020-2463-x.

[38] Kritsana Srakaew et al. „A subwavelength atomic array switched by a single Rydberg atom“. In: *Nature Physics* 19.5 (2023), pp. 714–719. DOI: 10.1038/s41567-023-01959-y.

[39] Anders S Sørensen and Klaus Mølmer. „Measurement Induced Entanglement and Quantum Computation with Atoms in Optical Cavities“. In: *Physical Review Letters* 91.9 (2003), p. 097905. DOI: 10.1103/PhysRevLett.91.097905.

[40] James S Douglas et al. „Quantum many-body models with cold atoms coupled to photonic crystals“. In: *Nature Photonics* 9.5 (2015), pp. 326–331. DOI: 10.1038/nphoton.2015.57.

[41] Alejandro González-Tudela et al. „Subwavelength vacuum lattices and atom–atom interactions in two-dimensional photonic crystals“. In: *Nature Photonics* 9.5 (2015), pp. 320–325. DOI: 10.1038/nphoton.2015.54.

[42] Dominik S Wild. „Algorithms and platforms for quantum science and technology“. PhD thesis. Harvard University, 2020.

[43] Arjan F. van Loo et al. „Photon-Mediated Interactions Between Distant Artificial Atoms“. In: *Science* 342.6165 (2013), pp. 1494–1496. DOI: 10.1126/science.1244324.

[44] Mohammad Mirhosseini et al. „Superconducting metamaterials for waveguide quantum electrodynamics“. In: *Nature Communications* 9.1 (2018), p. 3706. DOI: 10.1038/s41467-018-06142-z.

[45] Mohammad Mirhosseini et al. „Cavity Quantum Electrodynamics with Atom-like Mirrors“. In: *Nature* 569.7758 (2019), pp. 692–697. DOI: 10.1038/s41586-019-1196-1.

[46] Neereja M. Sundaresan et al. „Interacting Qubit-Photon Bound States with Superconducting Circuits“. In: *Phys. Rev. X* 9 (1 Feb. 2019), p. 011021. DOI: 10.1103/PhysRevX.9.011021.

[47] Fam Le Kien et al. „Nanofiber-mediated radiative transfer between two distant atoms“. In: *Phys. Rev. A* 72 (6 Dec. 2005), p. 063815. DOI: 10.1103/PhysRevA.72.063815.

[48] E. Vetsch et al. „Optical Interface Created by Laser-Cooled Atoms Trapped in the Evanescent Field Surrounding an Optical Nanofiber“. In: *Phys. Rev. Lett.* 104 (20 May 2010), p. 203603. DOI: 10.1103/PhysRevLett.104.203603.

[49] A. Goban et al. „Atom–light interactions in photonic crystals“. In: *Nature Communications* 5.1 (2014), p. 3808. DOI: 10.1038/ncomms4808.

[50] A. Goban et al. „Superradiance for Atoms Trapped along a Photonic Crystal Waveguide“. In: *Phys. Rev. Lett.* 115 (6 Aug. 2015), p. 063601. DOI: 10.1103/PhysRevLett.115.063601.

[51] Jonathan D. Hood et al. „Atom–atom interactions around the band edge of a photonic crystal waveguide“. In: *Proceedings of the National Academy of Sciences* 113.38 (2016), pp. 10507–10512. DOI: 10.1073/pnas.1603788113.

[52] A. Sipahigil et al. „An integrated diamond nanophotonics platform for quantum-optical networks“. In: *Science* 354.6314 (2016), pp. 847–850. DOI: 10.1126/science.aah6875.

[53] Carmen Palacios-Berraquero et al. „Large-scale quantum-emitter arrays in atomically thin semiconductors“. In: *Nature Communications* 8.1 (2017), p. 15093. DOI: 10.1038/ncomms15093.

[54] N. Samkharadze et al. „Strong spin-photon coupling in silicon“. In: *Science* 359.6380 (2018), pp. 1123–1127. DOI: 10.1126/science.aar4054.

[55] D E Chang et al. „Cavity QED with atomic mirrors“. In: *New Journal of Physics* 14.6 (June 2012), p. 063003. DOI: 10.1088/1367-2630/14/6/063003.

[56] Sajeev John and Jian Wang. „Quantum electrodynamics near a photonic band gap: Photon bound states and dressed atoms“. In: *Physical review letters* 64.20 (1990), p. 2418.

[57] Sajeev John and Jian Wang. „Quantum optics of localized light in a photonic band gap“. In: *Phys. Rev. B* 43 (16 June 1991), pp. 12772–12789. DOI: 10.1103/PhysRevB.43.12772.

[58] Alejandro González-Tudela and J Ignacio Cirac. „Markovian and non-Markovian dynamics of quantum emitters coupled to two-dimensional structured reservoirs“. In: *Physical Review A* 96.4 (2017), p. 043811.

[59] Alejandro González-Tudela and J Ignacio Cirac. „Quantum emitters in two-dimensional structured reservoirs in the nonperturbative regime“. In: *Physical Review Letters* 119.14 (2017), p. 143602.

[60] Kanupriya Sinha et al. „Non-Markovian collective emission from macroscopically separated emitters“. In: *Physical review letters* 124.4 (2020), p. 043603.

[61] H. Zoubi and H. Ritsch. „Metastability and directional emission characteristics of excitons in 1D optical lattices“. In: *EPL (Europhysics Letters)* 90.2 (Apr. 2010), p. 23001. DOI: 10.1209/0295-5075/90/23001.

[62] Jemma A Needham, Igor Lesanovsky, and Beatriz Olmos. „Subradiance-protected excitation transport“. In: *New Journal of Physics* 21.7 (July 2019), p. 073061. DOI: 10.1088/1367-2630/ab31e8.

[63] Stuart J. Masson and Ana Asenjo-Garcia. „Atomic-Waveguide Quantum Electrodynamics“. In: *Physical Review Research* 2.4 (2020), p. 043213. DOI: 10.1103/PhysRevResearch.2.043213.

[64] Taylor L Patti et al. „Controlling interactions between quantum emitters using atom arrays“. In: *Physical review letters* 126.22 (2021), p. 223602. DOI: https://doi.org/10.1103/PhysRevLett.126.223602.

[65] Giuseppe Calajó et al. „Exciting a bound state in the continuum through multiphoton scattering plus delayed quantum feedback“. In: *Physical review letters* 122.7 (2019), p. 073601.

[66] Lingzhen Guo et al. „Oscillating bound states for a giant atom“. In: *Physical Review Research* 2.4 (2020), p. 043014.

[67] Rahul Trivedi et al. „Optimal two-photon excitation of bound states in non-Markovian waveguide QED“. In: *Physical Review A* 104.1 (2021), p. 013705. DOI: https://doi.org/10.1103/PhysRevA.104.013705.

[68] Diego Porras and J Ignacio Cirac. „Collective generation of quantum states of light by entangled atoms“. In: *Physical Review A—Atomic, Molecular, and Optical Physics* 78.5 (2008), p. 053816. DOI: 10.1103/PhysRevA.78.053816.

[69] C J Mewton and Z Ficek. „Radiative properties of a linear chain of coupled qubits“. In: *Journal of Physics B: Atomic, Molecular and Optical Physics* 40.9 (Apr. 2007), S181–S197. DOI: 10.1088/0953-4075/40/9/s11.

[70] Yu-Xiang Zhang and Klaus Mølmer. „Theory of Subradiant States of a One-Dimensional Two-Level Atom Chain“. In: *Phys. Rev. Lett.* 122 (20 May 2019), p. 203605. DOI: 10.1103/PhysRevLett.122.203605.

[71] P Forn-Díaz et al. „Ultrastrong coupling of a single artificial atom to an electromagnetic continuum in the nonperturbative regime“. In: *Nature Physics* 13.1 (2017), pp. 39–43.

[72] Javier Puertas Martínez et al. „A tunable Josephson platform to explore many-body quantum optics in circuit-QED“. In: *npj Quantum Information* 5.1 (2019), pp. 1–8.

[73] GC Stey and RW Gibberd. „Decay of quantum states in some exactly soluble models“. In: *Physica* 60.1 (1972), pp. 1–26.

[74] Peter W Milonni and Peter L Knight. „Retardation in the resonant interaction of two identical atoms“. In: *Physical Review A* 10.4 (1974), p. 1096.

[75] U Dorner and P Zoller. „Laser-driven atoms in half-cavities“. In: *Physical Review A* 66.2 (2002), p. 023816.

[76] Beatriz Olmos et al. „Long-range interacting many-body systems with alkaline-earth-metal atoms“. In: *Physical review letters* 110.14 (2013), p. 143602.

[77] TC Tsui et al. „Realization of a stroboscopic optical lattice for cold atoms with subwavelength spacing“. In: *Physical Review A* 101.4 (2020), p. 041603.

[78] J. Sebby-Strabley et al. „Lattice of double wells for manipulating pairs of cold atoms“. In: *Phys. Rev. A* 73 (3 Mar. 2006), p. 033605. DOI: 10.1103/PhysRevA.73.033605.

[79] Marco Anderlini et al. „Controlled exchange interaction between pairs of neutral atoms in an optical lattice“. In: *Nature* 448.7152 (2007), pp. 452–456. DOI: 10.1038/nature06011.

[80] S. Fölling et al. „Direct observation of second-order atom tunnelling“. In: *Nature* 448.7157 (2007), pp. 1029–1032. DOI: 10.1038/nature06112.

[81] Stefan Trotzky et al. „Controlling and Detecting Spin Correlations of Ultracold Atoms in Optical Lattices“. In: *Phys. Rev. Lett.* 105 (26 Dec. 2010), p. 265303. DOI: 10.1103/PhysRevLett.105.265303.

[82] Michael Lubasch et al. „Adiabatic Preparation of a Heisenberg Antiferromagnet Using an Optical Superlattice“. In: *Phys. Rev. Lett.* 107 (16 Oct. 2011), p. 165301. DOI: 10.1103/PhysRevLett.107.165301.

[83] David Plankensteiner et al. „Selective protected state preparation of coupled dissipative quantum emitters“. In: *Scientific reports* 5.1 (2015), pp. 1–12.

[84] Yizun He et al. „Geometric control of collective spontaneous emission“. In: *Physical Review Letters* 125.21 (2020), p. 213602.

[85] Cosimo C Rusconi, Tao Shi, and J Ignacio Cirac. „Exploiting the photonic nonlinearity of free-space subwavelength arrays of atoms“. In: *Physical Review A* 104.3 (2021), p. 033718. DOI: 10.1103/PhysRevA.104.033718.

[86] P-O Guimond et al. „Subradiant bell states in distant atomic arrays“. In: *Physical review letters* 122.9 (2019), p. 093601. DOI: 10.1103/PhysRevLett.122.093601.

[87] Maria Moreno-Cardoner et al. „Subradiance-enhanced excitation transfer between dipole-coupled nanorings of quantum emitters“. In: *Phys. Rev. A* 100 (2 Aug. 2019), p. 023806. DOI: 10.1103/PhysRevA.100.023806.

[88] Morton M Sternheim and James F Walker. „Non-Hermitian Hamiltonians, decaying states, and perturbation theory“. In: *Physical Review C* 6.1 (1972), p. 114. DOI: 10.1103/PhysRevC.6.114.

[89] C-L Hung et al. „Quantum spin dynamics with pairwise-tunable, long-range interactions“. In: *Proceedings of the National Academy of Sciences* 113.34 (2016), E4946–E4955. DOI: 10.1073/pnas.1603777113.

[90] Dirk Bouwmeester, Artur Ekert, and Anton Zeilinger, eds. *The Physics of Quantum Information*. Berlin, Heidelberg: Springer Berlin Heidelberg, 2000. DOI: 10.1007/978-3-662-04209-0.

[91] H. J. Kimble. „The Quantum Internet“. In: *Nature* 453.7198 (2008), pp. 1023–1030. DOI: 10.1038/nature07127.

[92] S. Pirandola et al. „Advances in Quantum Cryptography“. In: *Advances in Optics and Photonics* 12.4 (2020), p. 1012. DOI: 10.1364/AOP.361502.

[93] D. Copsey et al. „Toward a Scalable, Silicon-Based Quantum Computing Architecture“. In: *IEEE Journal of Selected Topics in Quantum Electronics* 9.6 (2003), pp. 1552–1569. DOI: 10.1109/JSTQE.2003.820922.

[94] L.-M. Duan and C. Monroe. „*Colloquium* : Quantum Networks with Trapped Ions“. In: *Reviews of Modern Physics* 82.2 (2010), pp. 1209–1224. DOI: 10.1103/RevModPhys.82.1209.

[95] E. T. Khabiboulline et al. „Optical Interferometry with Quantum Networks“. In: *Phys. Rev. Lett.* 123 (7 Aug. 2019), p. 070504. DOI: 10.1103/PhysRevLett.123.070504.

[96] Fabrizio Illuminati. „Light Does Matter“. In: *Nature Physics* 2.12 (2006), pp. 803–804. DOI: 10.1038/nphys479.

[97] Stephan Ritter et al. „An Elementary Quantum Network of Single Atoms in Optical Cavities“. In: *Nature* 484.7393 (2012), pp. 195–200. DOI: 10.1038/nature11023.

[98] J. D. Thompson et al. „Coupling a Single Trapped Atom to a Nanoscale Optical Cavity“. In: *Science* 340.6137 (2013), pp. 1202–1205. DOI: 10.1126/science.1237125.

[99] T. G. Tiecke et al. „Nanophotonic Quantum Phase Switch with a Single Atom“. In: *Nature* 508.7495 (2014), pp. 241–244. DOI: 10.1038/nature13188.

[100] Stephan Welte et al. „Photon-Mediated Quantum Gate between Two Neutral Atoms in an Optical Cavity“. In: *Physical Review X* 8.1 (2018), p. 011018. DOI: 10.1103/PhysRevX.8.011018.

[101] Brandon Grinkemeyer et al. „Error-Detected Quantum Operations with Neutral Atoms Mediated by an Optical Cavity“. In: *arXiv preprint arXiv:2410.10787* (2024). DOI: https://doi.org/10.48550/arXiv.2410.10787.

[102] Shankar G. Menon et al. „An Integrated Atom Array – Nanophotonic Chip Platform with Background-Free Imaging“. In: *Nature Communications* 15.1 (2024), p. 6156. DOI: 10.1038/s41467-024-50355-4.

[103] Michael Reitz, Christian Sommer, and Claudiu Genes. „Cooperative Quantum Phenomena in Light-Matter Platforms“. In: *PRX Quantum* 3.1 (2022), p. 010201. DOI: 10.1103/PRXQuantum.3.010201.

[104] Janne Ruostekoski. „Cooperative Quantum-Optical Planar Arrays of Atoms“. In: *Physical Review A* 108.3 (2023), p. 030101. DOI: 10.1103/PhysRevA.108.030101.

[105] G. Facchinetti, S. D. Jenkins, and J. Ruostekoski. „Storing Light with Subradiant Correlations in Arrays of Atoms“. In: *Physical Review Letters* 117.24 (2016), p. 243601. DOI: 10.1103/PhysRevLett.117.243601.

[106] M T Manzoni et al. „Optimization of photon storage fidelity in ordered atomic arrays“. In: *New Journal of Physics* 20.8 (2018), p. 083048. DOI: 10.1088/1367-2630/aadb74.

[107] Oriol Rubies-Bigorda et al. „Photon Control and Coherent Interactions via Lattice Dark States in Atomic Arrays“. In: *Physical Review Research* 4.1 (2022), p. 013110. DOI: 10.1103/PhysRevResearch.4.013110.

[108] Kyle E. Ballantine and Janne Ruostekoski. „Cooperative Optical Wavefront Engineering with Atomic Arrays“. In: *Nanophotonics* 10.7 (2021), pp. 1901–1909. DOI: 10.1515/nanoph-2021-0059.

[109] D. Fernández-Fernández and A. González-Tudela. „Tunable Directional Emission and Collective Dissipation with Quantum Metasurfaces“. In: *Physical Review Letters* 128.11 (2022), p. 113601. DOI: 10.1103/PhysRevLett.128.113601.

[110] Nico S Baßler et al. „Metasurface-based hybrid optical cavities for chiral sensing“. In: *Physical Review Letters* 132.4 (2024), p. 043602. DOI: 10.1103/PhysRevLett.132.043602.

[111] K. D. B. Higgins et al. „Superabsorption of Light via Quantum Engineering“. In: *Nature Communications* 5.1 (2014), p. 4705. DOI: 10.1038/ncomms5705.

[112] Raphael Holzinger et al. „Nanoscale Coherent Light Source“. In: *Physical Review Letters* 124.25 (2020), p. 253603. DOI: 10.1103/PhysRevLett.124.253603.

[113] K. E. Ballantine and J. Ruostekoski. „Unidirectional Absorption, Storage, and Emission of Single Photons in a Collectively Responding Bilayer Atomic Array“. In: *Physical Review Research* 4.3 (2022), p. 033200. DOI: 10.1103/PhysRevResearch.4.033200.

[114] Taylor L. Patti et al. „Controlling Interactions between Quantum Emitters Using Atom Arrays“. In: *Physical Review Letters* 126.22 (2021), p. 223602. DOI: 10.1103/PhysRevLett.126.223602.

[115] Christof Weitenberg et al. „Single-Spin Addressing in an Atomic Mott Insulator“. In: *Nature* 471.7338 (2011), pp. 319–324. DOI: 10.1038/nature09827.

[116] Immanuel Bloch, Jean Dalibard, and Sylvain Nascimbène. „Quantum Simulations with Ultracold Quantum Gases“. In: *Nature Physics* 8.4 (2012), pp. 267–276. DOI: 10.1038/nphys2259.

[117] Yang Wang et al. „Coherent Addressing of Individual Neutral Atoms in a 3D Optical Lattice“. In: *Physical Review Letters* 115.4 (2015), p. 043003. DOI: 10.1103/PhysRevLett.115.043003.

[118] Ephraim Shahmoon, Mikhail D. Lukin, and Susanne F. Yelin. „Quantum Optomechanics of a Two-Dimensional Atomic Array“. In: *Physical Review A* 101.6 (2020), p. 063833. DOI: 10.1103/PhysRevA.101.063833.

[119] Ephraim Shahmoon et al. „Cavity Quantum Optomechanics with an Atom-Array Membrane“. In: arXiv:2006.01973 (2020).

[120] D. O'Shea et al. „All-Optical Switching and Strong Coupling Using Tunable Whispering-Gallery-Mode Microresonators“. In: *Applied Physics B* 105.1 (2011), pp. 129–148. DOI: 10.1007/s00340-011-4714-x.

[121] Iacopo Carusotto and Cristiano Ciuti. „Quantum Fluids of Light“. In: *Reviews of Modern Physics* 85.1 (2013), pp. 299–366. DOI: 10.1103/RevModPhys.85.299.

[122] Robert J. Bettles et al. „Quantum and Nonlinear Effects in Light Transmitted through Planar Atomic Arrays“. In: *Communications Physics* 3.1 (2020), pp. 1–9. DOI: 10.1038/s42005-020-00404-3.

[123] Simon Panyella Pedersen, Lida Zhang, and Thomas Pohl. „Quantum nonlinear metasurfaces from dual arrays of ultracold atoms“. In: *Physical Review Research* 5.1 (2023), p. L012047. DOI: 10.1103/PhysRevResearch.5.L012047.

[124] F. Robicheaux and Deepak A. Suresh. „Intensity Effects of Light Coupling to One- or Two-Atom Arrays of Infinite Extent“. In: *Physical Review A* 108.1 (2023), p. 013711. DOI: 10.1103/PhysRevA.108.013711.

[125] R. Bekenstein et al. „Quantum Metasurfaces with Atom Arrays“. In: *Nature Physics* 16.6 (2020), pp. 676–681. DOI: 10.1038/s41567-020-0845-5.

[126] M. Moreno-Cardoner, D. Goncalves, and D. E. Chang. „Quantum Nonlinear Optics Based on Two-Dimensional Rydberg Atom Arrays“. In: *Physical Review Letters* 127.26 (2021), p. 263602. DOI: 10.1103/PhysRevLett.127.263602.

[127] Lida Zhang et al. „Photon-Photon Interactions in Rydberg-atom Arrays“. In: *Quantum* 6 (2022), p. 674. DOI: 10.22331/q-2022-03-30-674.

[128] J. D. Carter, O. Cherry, and J. D. D. Martin. „Electric-Field Sensing near the Surface Microstructure of an Atom Chip Using Cold Rydberg Atoms“. In: *Physical Review A* 86.5 (2012), p. 053401. DOI: 10.1103/PhysRevA.86.053401.

[129] Crispin Gardiner and Peter Zoller. *Quantum noise: a handbook of Markovian and non-Markovian quantum stochastic methods with applications to quantum optics*. Springer Science & Business Media, 2004.

[130] Bindiya Arora, MS Safronova, and Charles W Clark. „Magic wavelengths for the n p- n s transitions in alkali-metal atoms“. In: *Physical Review A* 76.5 (2007), p. 052509. DOI: 10.1103/PhysRevA.76.052509.

[131] Eugene P Wigner. „Lower limit for the energy derivative of the scattering phase shift“. In: *Physical Review* 98.1 (1955), p. 145. DOI: 10.1103/PhysRev.98.145.

[132] R. Bourgain et al. „Direct measurement of the Wigner time delay for the scattering of light by a single atom“. In: *Optics Letters* 38.11 (May 2013), p. 1963. DOI: 10.1364/ol.38.001963.

[133] Simon Panyella Pedersen. *Nonlinear Quantum Optics in an Atomic Cavity*. 2023. arXiv preprint arXiv: 2311.03918 (quant-ph).

[134] Anthony E Siegman. *Lasers*. University Science Books, 1986.

[135] Haruka Tanji-Suzuki et al. „Interaction between Atomic Ensembles and Optical Resonators: Classical Description“. In: *Advances in Atomic, Molecular, and Optical Physics*. Ed. by E. Arimondo, P.R. Berman, and C.C. Lin. Vol. 60. Academic Press, 2011, pp. 201–237. DOI: 10.1016/B978-0-12-385508-4.00004-8.

[136] Tingye Li. „Diffraction loss and selection of modes in maser resonators with circular mirrors“. In: *The Bell System Technical Journal* 44.5 (1965), pp. 917–932. DOI: 10.1002/j.1538-7305.1965.tb01673.x.

[137] Yakov Solomons, Roni Ben-Maimon, and Ephraim Shahmoon. „Universal approach for quantum interfaces with atomic arrays“. In: *PRX Quantum* 5.2 (2024), p. 020329. DOI: 10.1103/PRXQuantum.5.020329.

[138] Michael James Kastoryano, Florentin Reiter, and Anders Søndberg Sørensen. „Dissipative preparation of entanglement in optical cavities“. In: *Physical review letters* 106.9 (2011), p. 090502. DOI: 10.1103/PhysRevLett.106.090502.

[139] Karim Murr. „On the suppression of the diffusion and the quantum nature of a cavity mode. Optical bistability: forces and friction in driven cavities“. In: *Journal of Physics B: Atomic, Molecular and Optical Physics* 36.12 (2003), p. 2515. DOI: 10.1088/0953-4075/36/12/311.

[140] Mark D Lee, Stewart D Jenkins, and Janne Ruostekoski. „Stochastic methods for light propagation and recurrent scattering in saturated and nonsaturated atomic ensembles“. In: *Physical Review A* 93.6 (2016), p. 063803. DOI: 10.1103/PhysRevA.93.063803.

[141] Teresa D Karanikolaou, Robert J Bettles, and Darrick E Chang. „Near-resonant light scattering by an atom in a state-dependent trap“. In: *New Journal of Physics* 26.4 (2024), p. 043005. DOI: 10.1088/1367-2630/ad3775.

[142] Adam M. Kaufman and Kang-Kuen Ni. „Quantum science with optical tweezer arrays of ultracold atoms and molecules“. In: *Nature Physics* 17.12 (Nov. 2021), pp. 1324–1333. DOI: 10.1038/s41567-021-01357-2.

[143] Tim Schröder et al. „Scalable focused ion beam creation of nearly lifetime-limited single quantum emitters in diamond nanostructures“. In: *Nature Communications* 8.1 (May 2017). DOI: 10.1038/ncomms15376.

[144] Patrick Back et al. „Realization of an Electrically Tunable Narrow-Bandwidth Atomically Thin Mirror Using Monolayer $MoSe_2$“. In: *Phys. Rev. Lett.* 120 (3 Jan. 2018), p. 037401. DOI: 10.1103/PhysRevLett.120.037401.

[145] Giovanni Scuri et al. „Large Excitonic Reflectivity of Monolayer $MoSe_2$ Encapsulated in Hexagonal Boron Nitride“. In: *Phys. Rev. Lett.* 120 (3 Jan. 2018), p. 037402. DOI: 10.1103/PhysRevLett.120.037402.

[146] Dominik S. Wild et al. „Quantum Nonlinear Optics in Atomically Thin Materials“. In: *Phys. Rev. Lett.* 121 (12 Sept. 2018), p. 123606. DOI: 10.1103/PhysRevLett.121.123606.

[147] Sergey Bravyi, David P. DiVincenzo, and Daniel Loss. „Schrieffer–Wolff Transformation for Quantum Many-Body Systems“. In: *Annals of Physics* 326.10 (2011), pp. 2793–2826. DOI: 10.1016/j.aop.2011.06.004.